MUC16 AND L1CAM TARGETED MOLECULAR IMAGING OF OVARIAN EPITHELIAL CARCINOMA

by

BRANDON ELISHA NEMIEBOKA

September 2017

A dissertation submitted to the Faculty of the Louis V. Gerstner, Jr. Graduate School of Biomedical Sciences at Memorial Sloan Kettering Cancer Center in partial fulfillment of the requirements for the degree of Doctor of Philosophy.

Abstract

L1-cell adhesion molecule (L1CAM) is a cell surface glycoprotein of the immunoglobulin superfamily critical for normal development of the central nervous system. It is overexpressed in human malignancies including neuroblastoma and epithelial ovarian carcinoma (EOC). L1CAM has been implicated in a variety of cancer processes including tumor progression and metastasis. Diagnostic imaging modalities for EOC are generally inadequate and curative therapy for subsets of these high-risk cancers is an unmet need. Here, we evaluate ^{89}Zr-radiolabeled anti-L1CAM antibodies *in vitro* and *in vivo* as a PET imaging agent for EOC. Two humanized IgG antibodies (HuE71, produced in GnT1-deficient CHO cells and HuE71-4 (IgG4 class switch produced in wild type CHO cells) were prepared. HuE71 and HuE71-4 were conjugated with desferrioxamine-isothiocyanate and radiolabeled with ^{89}Zr to high specific with high crude radiochemical purities. The stabilities of these complexes were assessed through a serum challenge study, which revealed intact construct after 7 days in human serum at 37°C. The immunoreactivity of radiolabeled antibodies was assessed in the L1CAM-positive ovarian cancer cell line, SKOV-3.

To evaluate the tracers *in vivo*, female athymic nude mice bearing subcutaneous SKOV-3 tumors were utilized. Serial PET imaging studies revealed distinct *in vivo* biodistribution profiles for each of the antibodies. ^{89}Zr-HuE71 revealed rapid accumulation of the tracer in the tumor tissue at 24 hours post-injection continuing to accumulate through 120 hours. On the other hand, ^{89}Zr-HuE71-4 showed a slightly lower uptake at 24 hours but accumulation of the tracer continued to throughout 120 hours. With the exception of liver, background organ uptake differed dramatically between the tracers with ^{89}Zr-HuE71 showing axillary and submandibular lymph node uptake at 24 hours while ^{89}Zr-HuE71-4 revealed minimal lymph node uptake. Histological analysis of the lymph nodes confirmed the absence of metastatic cells, but revealed histiocytosis and hyperplasia

consistent with drainage reaction. Kidney uptake of these tracers differed as well with ^{89}Zr-HuE71-4 showing high kidney uptake by 72 hours post-injection. Conversely, kidney uptake of ^{89}Zr-HuE71 showed only minimal kidney uptake. The differential biodistribution profile seen with these antibodies suggests that the high lymph node uptake of ^{89}Zr-HuE71 was probably secondary to Fc receptor binding, absent for IgG4 antibodies, hence the low lymphoid uptake of huE71-4. The high renal uptake of ^{89}Zr-huE71-4 may be secondary to Fab exchange characteristic of the IgG4 subclass *in vivo*.

Acknowledgements

To my thesis advisor, Dr. Jason Lewis, a million thanks for providing me with the opportunity to conduct research in your laboratory. Your mentorship and support have been invaluable during this training experience. Much gratitude to my thesis advisory committee, Dr. David Scheinberg, Dr. Nai-Kong Cheung, and Dr. Douglass Ballon for your support and guidance throughout the years. Thanks to the members (past and present) of the Lewis Lab, Spriggs Lab and the Cheung Lab, especially Dr. Maya Suzuki for help making the L1CAM antibodies.

Table of Contents

Table of Figures

Chapter 1

Chapter 2

Chapter 3

Chapter 4

Appendix

CHAPTER 1: Introduction to Molecular Imaging of Ovarian Cancer

This chapter is an adaptation of research originally published in the Journal of Nuclear Medicine: Sharma SK, Nemieboka B, Sala E, Lewis JS, Zeglis BM. Molecular Imaging of Ovarian Cancer. Journal of Nuclear Medicine. 2016; 57(6):827-33

Introduction

Ovarian cancer continues to be the most lethal gynecologic malignancy and the fifth leading cause of cancer-related deaths in women. As of 2015, the 5-year survival rate for advanced stage ovarian cancer is a dismal 27% [(1)]. This high mortality rate can largely be attributed to three issues: (a) the lack of effective screening tests and diagnostic methods; (b) the vague symptomatic presentation of the disease, which leads to late detection; and (c) the frequent recurrence of therapy-resistant disease after initial treatment. The statistics with regard to the first two concerns are particularly striking. If detected at an early stage (I), there is a 90% cure rate for ovarian cancers. However, this rate drops precipitously to 20-25% for patients diagnosed at later stages (III-IV)[(2)]. Clearly, advances across a variety of fields are needed to improve the clinical management of this disease. In the pages that follow, our goal is to focus on a growing part of this puzzle by providing a bird's-eye view of the roles that *molecular imaging* can play in the clinical care of ovarian cancer.

Different imaging modalities provide different types of information. *Anatomical imaging* methods such as ultrasound and CT create exquisitely detailed maps of organ morphology, while *molecular imaging* modalities such as PET and optical imaging yield functional information on the biochemistry of tissues. Not surprisingly, both types of imaging play important roles in the clinical management of ovarian cancer. To wit, the use of ultrasound as the first imaging modality in the characterization of adnexal lesions and CT for the evaluation of disease extent in patients with suspected ovarian cancer

are two examples of the integration of *anatomical* imaging into current clinical protocols for the disease.

Over the past two decades, a variety of *molecular imaging* modalities have emerged to complement traditional anatomical imaging. Indeed, molecular imaging techniques can serve a variety of roles in the clinical care of ovarian cancer patients, including (i) the localization of primary tumors; (ii) the determination of the extent of metastatic spread; (iii) the stratification of patients for surgery and therapy; (iv) the evaluation of the metabolic status of the tumor; (v) the characterization of the expression levels of biomarkers by the malignant tissue; and (vi) the design, implementation, and monitoring of targeted therapies.

In this introduction, our goal is to provide a broad overview of the roles that imaging — and *molecular* imaging, in particular — plays in the management of ovarian cancer. The introduction is composed of four sections, each focused on a different type of imaging: magnetic resonance imaging, nuclear imaging, optical imaging, and ultrasound imaging. While primary emphasis is given to clinical studies, particularly innovative and promising preclinical investigations will be discussed as well.

Magnetic Resonance Imaging

Traditional magnetic resonance imaging has demonstrated significant utility in ovarian cancer imaging, particularly in distinguishing between benign and malignant ovarian lesions that are indeterminate on ultrasound. For example, a recent study performed by Haggerty *et al.* in patients with indeterminate adnexal masses showed that pelvic MRI had a sensitivity of 95.0% and specificity of 94.1% for detecting malignant tissue [(3)]. Similarly, Adusumilli and colleagues demonstrated that MR imaging boasts a sensitivity of 100% for identifying malignant tissue and a specificity of 94% for the delineation of benign ovarian masses [(4)]. To improve the visibility of anatomical structures,

contrast agents are frequently used in conjunction with MR imaging. Along these lines, recent years have witnessed a surge in preclinical studies using targeted contrast agents based on super-paramagnetic iron oxide nanoparticles (SPIONs) [5]. In one study, Shahbazi-Gahrouei and colleagues conjugated SPIONs with a MUC1-specific antibody and conducted *in vivo* animal imaging and biodistribution studies in OVCAR3 tumor-bearing mice which showed significant and specific uptake of the contrast agent within the tumor tissue [5]. Quan, *et al* obtained similar results in an investigation using ultra-small SPIONs bearing antibodies that target ovarian carcinoma-associated antigen [6].

Beyond providing anatomic information, MRI can *also* be used for functional imaging via diffusion-weighted imaging (DWI), dynamic contrast enhanced (DCE), and magnetic resonance spectroscopy (MRS). DWI measures the Brownian motion of water molecules, which is impacted by the hypercellularity of tumor tissue and the extracellular architecture. Apparent diffusion coefficients (ADC) derived from DWI provide a quantitative parameter of the diffusivity of the imaged tissue. In a 41 patient study, Schwenzer, *et al.* evaluated DWI in the context of peritoneal carcinomatosis and compared the results to ^{18}F-FDG-PET/CT [7]. They found that there was a moderate yet significant correlation between ADC and standard uptake value (SUV) for peritoneal masses. DCE-MRI, on the other hand, acquires images at different time points following the injection of an MR contrast agent. The transport kinetics of the contrast agent into the tumor are calculated and depend on both vascularity and permeability of the malignant tissue. In a clinical study performed by Li, *et al.*, DCE-MRI was able to detect a significant difference between the contrast enhancement profiles of benign and malignant ovarian tumors [8]. Finally, MRS measures the chemical composition of regions of interest yielding semi-quantitative data on biochemical compounds such as choline, creatine, and lactate. Esseridou, *et al.* evaluated MRS in 16 patients with ovarian masses who underwent MRI/MRS followed by histopathological examination of the masses [9]. Of the 19 malignant tumors

identified by histopathology, 17 demonstrated a choline peak on MRS, indicative of metabolic deregulation and malignancy. Finally, in a prospective study of 21 patients undergoing neo-adjuvant chemotherapy for advanced ovarian cancer, Sala, *et al.* found significant differences in baseline ADC values between primary ovarian cancer, omental cake, and peritoneal deposits, indicating that diffusivity profiles may be tumor site-dependent and suggesting biological heterogeneity of disease (Figure 1.1) [(10)]. In this work, ADC and the fractional volume of the extravascular extracellular space (v_e) correlated with the cytotoxic effects of platinum-based therapy and are thus potentially useful response biomarkers, while choline concentration predicted but did not reflect response. Furthermore, ovarian tumors and metastatic peritoneal implants display spatial heterogeneity as perfusion, diffusion, and metabolism can vary markedly within the spatially distant tumor sub-regions which may in turn represent distinct phenotypic habitats within the tumor, distinct clonality, or a combination thereof.

Nuclear Imaging

Not surprisingly, the most ubiquitous radiotracer in oncologic PET imaging — ^{18}F-FDG — has been used in a variety of ways in the management of ovarian cancer. For example, several reports point to the superior performance of FDG-PET/CT in the detection of *recurrent* ovarian cancer. For example, FDG-PET/CT is reported to have found positive lesions in many instances where CT by itself was negative [(11)]. Furthermore, FDG-PET was able to document the evidence of disease recurrence 6 months prior to findings on CT [(12)]. Pre-operative whole body imaging via FDG-PET/CT has often contributed to the accurate upstaging of ovarian cancer patients as well, especially with regard to lymph node involvement (Figure 1.2) [(13,14)]. In addition to the qualitative visualization of lesions on an FDG-PET scan, semi-quantitative parameters such as SUV have been shown to have prognostic and predictive utility during clinical follow-up [(15)].

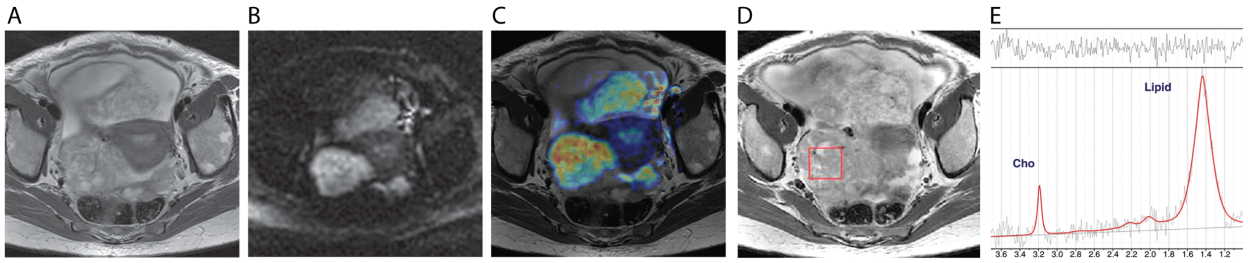

Figure 1.1. Multiparametric MR images (3.0 T) of a 58-year-old woman with advanced ovarian cancer.
(A) T2-weighted imaged; (B) DW image (b = 500 sec/mm2); (C) fused T2 and DW image; (D) T2-weighted image showing ROI for MR spectroscopy (red); (E) spectral fit (red) overlaid on the raw MRS data (grey), illustrating a strong choline (Cho) signal. Adapted and reprinted with permission from Sala, et al [10].

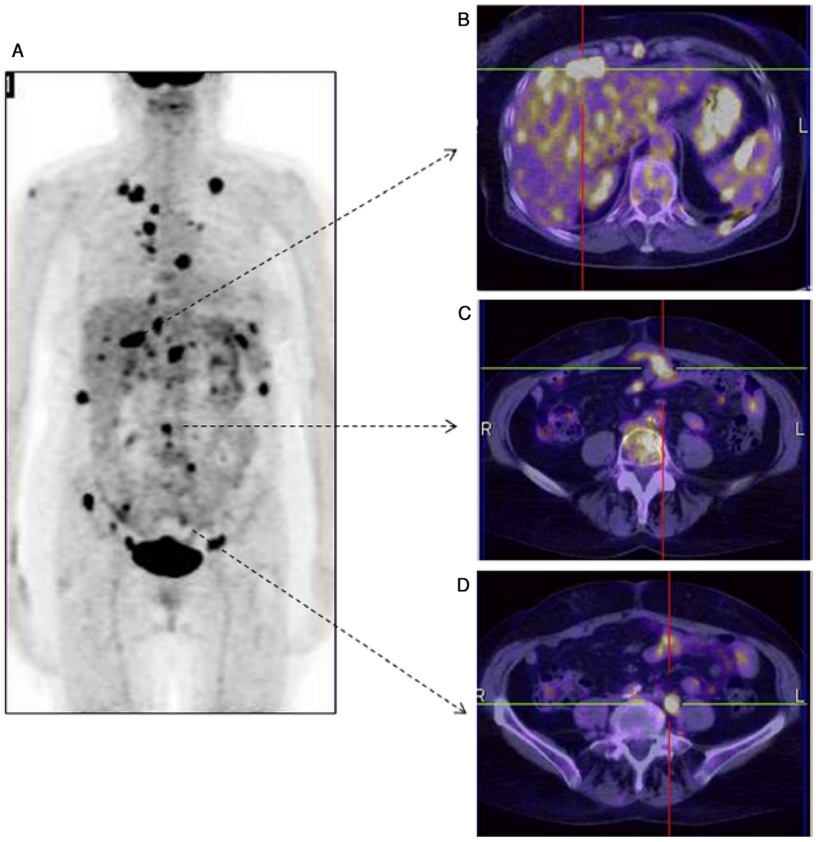

Figure 1.2. FDG-PET/CT of recurrent ovarian cancer.
(A) Maximum intensity projection FDG-PET; (B-D) transaxial fused PET/CT images delineating uptake of the radiotracer in the liver (B), the peritoneum (C), and the locoregional lymph nodes (D). Adapted and reprinted with permission from Caobelli *et al.* [14].

Along these lines, Vallius *et al.* used FDG-PET/CT to predict histopathologic responders from non-responders to neoadjuvant chemotherapy (NACT) prior to interval debulking surgery [16]. In another example, a recent clinical study in 12 platinum-resistant patients demonstrated an exposure–response relationship between a pan-AKT inhibitor and the tumoral uptake of FDG [17].

Despite its utility in ovarian cancer, FDG-PET has some important limitations, most notably the prevalence of *false negatives* associated with the cystic nature of ovarian cancer and *false positives* stemming from the uptake of FDG in inflammatory cells and benign growths. In response to these limitations, an impressive array of second-generation radiotracers have been developed and translated to the clinic. For example, two SPECT radiotracers that target the folate receptor (FR) — ^{111}In-DTPA-folate and ^{99m}Tc-etarfolatide — have shown promise for the delineation of newly-diagnosed ovarian cancer and the stratification of patients based on their levels of FR expression in ovarian tumor lesions, respectively [18,19]. Shifting gears to PET, a recent clinical report probing the possibility of imaging estrogen receptor alpha (ER) levels with ^{18}F-labeled estradiol found that this radiotracer could delineate ER+ tumors from ER- tumors with high specificity [20]. Finally, a first-in-human PET imaging study using a ^{89}Zr-labeled anti-mesothelin antibody in 4 ovarian cancer and 7 pancreatic cancer patients found that the mean SUV_{max} was higher in ovarian cancer lesions than in pancreatic cancer lesions [21].

Moving from the clinic to the laboratory, a number of promising imaging agents have been the subjects of preclinical studies in recent years. Sharma, *et al.*, for example, have reported the development of a ^{89}Zr-labeled radioimmunoconjugate based on the CA125-targeting murine antibody B43.13 [22]. Notably, this agent is capable of delineating the metastatic spread of OVCAR3 tumors along the ipsilateral chain of lymph nodes. Ocak, *et al.* recently employed a ^{68}Ga-DOTA-albumin-folate conjugate and FR680 for the multimodal PET/FMT imaging of the intraperitoneal spread of FR-positive MKP-L cells [23]. Similarly, Liu and coworkers reported on the multimodal

PET/OI imaging of metastatic ovarian tumors within the peritoneum of mice using a ^{64}Cu-labeled pyropheophorbide-folate conjugate [24]. Finally, Li, *et al.* have recently created a SPECT imaging agent to target the interleukin-6 receptor (IL-6R) [25]. In their work, a radiolabeled IL-6R-targeting peptide — ^{99m}Tc-HYNIC-Aca-LSLITRL — displayed high uptake in C13K tumors that express high levels of IL-6R and much reduced retention in SKOV3.ip tumors known to express low levels of IL-6R.

A particularly interesting subset of preclinical investigations has focused on the use of nuclear imaging for the monitoring of therapeutic progress. For example, the HER2-targeted affibody ^{99m}Tc-peptide-$Z_{HER2:342}$ was recently successfully employed for monitoring the efficacy of trastuzumab therapy in a SKOV3 xenograft model via SPECT [26]. Likewise, Niu *et al.* have shown that the uptake of ^{64}Cu-DOTA-trastuzumab can be used to monitor response to therapy with 17-DMAG [27]. Finally, Nagengast *et al.* have demonstrated the utility of ^{89}Zr-labeled bevacizumab as an imaging marker for early response to anti-angiogenic therapy with an Hsp90 inhibitor, NVP-AUY922 [28].

Optical Imaging

Optical imaging is emerging as a powerful tool in biomedical research and clinical practice. In oncology, the use of fluorescent probes as tools for image-guided surgery has proven particularly promising. In this setting, the imaging agents assist surgeons in distinguishing malignant from benign tissue with the help of a navigation system that activates the molecular probe and captures and processes the emitted light to generate an image in real time [29]. The first-in-human studies using this approach were published in 2011 by van Damm, *et al.,* who exploited the over-expression of folate receptor alpha (FR-□) in ovarian cancer by developing a fluorescein-conjugated folate probe (FITC-folate) (Figure 1.3) [30]. Ten patients with suspected ovarian cancer received an

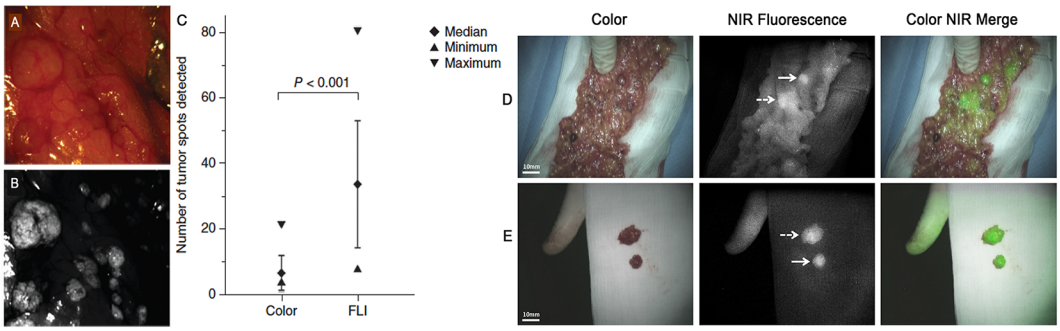

Figure 1.3. Identification of metastatic ovarian cancer deposits via intraoperative and *ex vivo* fluorescence Imaging.

Comparative images of tumors within the abdominal cavity visualized under white light (A) versus fluorescence emissions from a folate receptor-targeted probe (B); (C) statistical analysis revealing the benefit of intraoperative fluorescence imaging; (D) identification of two metastatic lesions in the greater omentum using the indocyanine green dye; (E) *ex vivo* visualization of the resected lesions. Adapted and reprinted with permission from van Dam *et al.* [30] and Tummers *et al.* [31].

injection of the probe and underwent image-guided surgery, followed by post-operative histopathological analyses. Critically, all tissue samples that fluoresced *in vivo* and *ex vivo* were confirmed to be malignant, while none of the resected benign tissues exhibited fluorescence. Similarly, a clinical trial is currently underway with data recently presented by Tummers *et al* [32]. Briefly, FITC-conjugated folate was injected into patients undergoing cytoreductive surgery. Out of the 12 ovarian cancer patients, 44 confirmed malignant lesions were resected, including 6 that were not identified by initial surgical inspection.

Recently, the attention of the field has shifted from fluorophores that emit visible light to probes that emit near infrared fluorescence (NIRF). To provide a few examples, Terwisscha van Scheltinga *et al.* targeted epidermal growth factor receptor 2 (HER2) and vascular endothelial growth factor using IRDye 800CW-labeled monoclonal antibodies [33], while Lee *et al.* targeted FR- with an activatable NIRF probe that only emits fluorescence following cleavage of a linker by the lysosomal enzyme cathepsin B [34]. In the clinic, Tummers *et al.* conducted a trial in which 10 patients with suspected ovarian cancer were administered indocyanine green (ICG) prior to image-guided cytoreductive surgery. Although all of the metastatic deposits in these patients exhibited NIR fluorescence, 13 non-malignant lesions also exhibited fluorescence, leading to a high false-positive rate of 62% [31].

Ultrasound

Both photoacoustic imaging and traditional ultrasound have also shown promise for ovarian cancer imaging. As its name suggests, photoacoustic imaging is predicated on the photoacoustic effect: the generation of ultrasonic waves following the absorption of photons by biomolecules such as hemoglobin or melanin. Because ultrasonic waves exhibit less scattering in biological tissue compared to photons, photoacoustic imaging has the potential to visualize tumors deep within the

body [35]. Along these lines, Aguirre *et al.* have developed a co-registered ultrasound/photoacoustic imaging system and used it to image 33 ovary samples collected from patients undergoing oophorectomy, ultimately determining a sensitivity and specificity of 83% for diagnosing ovarian cancer in postmenopausal ovaries [36]. More recently, several papers have been published improving upon the hybrid technology, including the creation of a system for the real-time co-registration of images [37] and a miniaturized illumination probe for transvaginal photoacoustic imaging [38]. Exogenous contrast agents can also be used for photoacoustic imaging, as Jokerst *et al.* have illustrated in their work using non-targeted gold nanorods as a contrast agent for photoacoustic *and* Raman imaging [39].

Traditional ultrasound continues to be further improved as well, especially with the development of microbubble-based contrast agents for the imaging of tumor angiogenesis. For example, Willmann *et al.* observed increased ultrasound signal in ovarian tumor tissue after the administration of perfluorocarbon-filled microbubbles conjugated to knottin peptides targeting integrin $alpha_v beta_3$ [40]. More recently, Lutz *et al.* observed a significantly higher ultrasound signal using microbubbles engineered to target the vascular marker CD276 (Figure 1.4) [41]. Ultimately, the real-time acquisition and processing of both traditional ultrasound and photoacoustic imaging — combined with the fact that ultrasound systems are inexpensive and widespread in the clinic — make these modalities primed for increased use as diagnostic tools for ovarian cancer.

Conclusion

With the advent of personalized medicine, this field has reached a fascinating crossroads. Much of the silence of the '*silent killer*' has been dispelled, and recent years have witnessed a surge in the

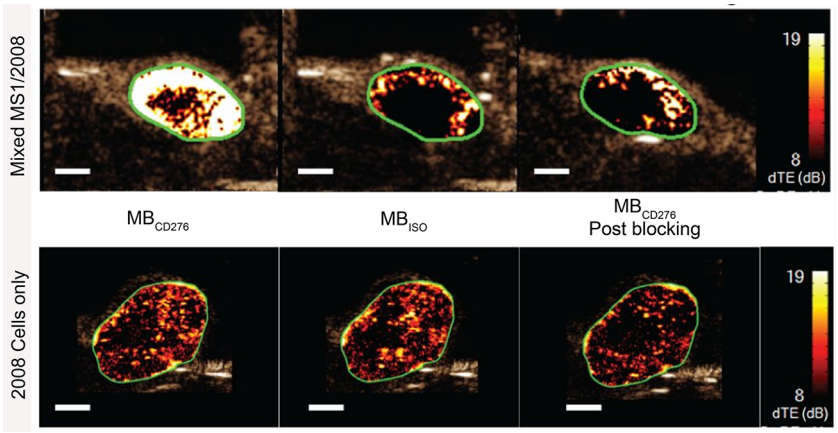

Figure 1.4. Preclinical contrast-enhanced ultrasound imaging of angiogenesis.
Microbubbles functionalized with a CD276-targeting antibody (MB_{CD276}) effectively targeted xenografts composed of 2008 human ovarian cancer cells mixed with the CD276-expressing MS1 mouse endothelial cells. The specificity of targeting was demonstrated via comparison with isotype antibody-functionalized microbubbles (MB_{ISO}) as well as a blocking experiment in which an excess of CD276 antibody was administered. Adapted and reprinted with permission from Lutz *et al.* [41].

understanding of the etiology and molecular characteristics of the disease. In light of these advances, we believe that imaging will play a central role in both the preclinical study and clinical management of ovarian cancer in the years to come. As we have discussed in these pages, an array of extremely promising imaging strategies have *already* impacted clinical care. The future is even brighter. Indeed, there are a variety of different avenues that are primed for innovation. In our opinion, two stand out. First, the use of hybrid imaging systems — such as PET/MR — that provides simultaneous anatomical and functional data has shown potential in the ovarian cancer setting and certainly merits further investigation (Figure 1.5). Second, the current push to unravel the molecular fingerprints of the sub-types of ovarian cancer has yielded a list of new biomarkers that is growing by the day. Molecular imaging agents targeting these biomarkers have the potential to serve two exciting roles: as *diagnostic tools* for the identification of a patient's tumor type and as *theranostic tools* for the selection of personalized targeted therapies. In the end, we are optimistic and hopeful that the combination of technological innovations, novel imaging probes, and the further integration of imaging into clinical protocols will lead to significant and lasting improvements in the prognosis and care of ovarian cancer patients.

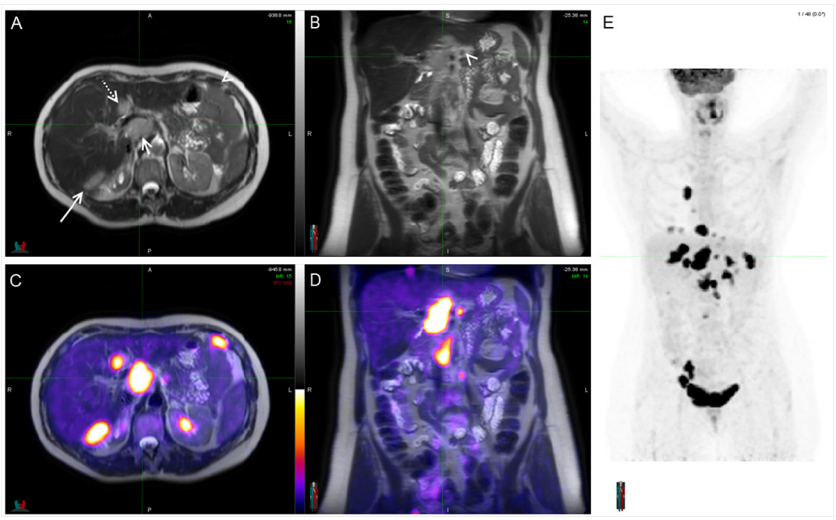

Figure 1.5. PET/MRI: An emerging hybrid imaging technique.
Axial (A) and coronal (B) T2-weighted MRI scans of an ovarian cancer patient, in which tumor lesions were seen adjacent to the liver (long arrow), segment IV of the liver (dotted arrow), *porta hepatis* (short arrow), and peritoneum (arrowheads); fused axial (C) and coronal (D) PET/MRI scans wherein FDG-PET not only demonstrated excellent correlation with lesions identified previously by MRI alone but also highlighted new lesions; (E) whole body MIP from FDG-PET showing multiple lesions in the chest and abdomen. Adapted and reprinted with permission from Partovi *et al.* [42].

CHAPTER 2: Preclinical Evaluation of MUC16 Antibodies for PET Imaging of Ovarian Cancer

Introduction:

Ovarian Epithelial Carcinoma

With approximately 22,440 cases estimated to be diagnosed in 2017, ovarian cancer is the second most common gynecologic malignancy and the most common cause of gynecologic cancer death in the United States [43]. There are a several distinct types of ovarian cancer such as germ cell tumors and sex-cord stromal tumors, but epithelial ovarian carcinoma constitutes the majority of the cases with 95% being attributed to this class [44]. Although the incidence is low compared to other cancer types, the average 5-year survival is low, 29% [45]. This is due to the non-specific symptoms such as bloating, abdominal pain, and fatigue which cause many patients to present with advanced-stage disease [46]. CA-125, a serum biomarker cleaved from the transmembrane protein MUC16, is used as a diagnostic tool for ovarian epithelial carcinoma. Although CA-125 is the most widely used laboratory test for the evaluation of adnexal masses, its utility as a tumor marker has been debated in the literature due to its low specificity (78%) and low sensitivity (78%), especially in early- stage and premenopausal patients [46]. In addition, this serum biomarker is known to be elevated in several conditions other than ovarian epithelial carcinoma such as uterine inflammation, liver disease and pancreatitis [47].

In terms of imaging modalities used for the initial evaluation of adnexal masses, transvaginal ultrasound is the most widely used [48]. Despite its high sensitivity for identifying masses (99.7%), the specificity for malignant masses is low (33.7%) [49]. Due to the high risk of spillage and seeding of malignant cells upon puncturing the mass, image-guided biopsies are not routinely performed in patients with suspicious lesions [50]. Thus, a definitive diagnosis of epithelial ovarian carcinoma

requires surgical resection of the mass and histologic analysis. In fact, a large proportion of patients with adnexal masses who undergo surgery do not have epithelial ovarian carcinoma. For example, in a large ovarian cancer screening randomized trial, of the 570 patients that underwent a surgical procedure for suspicious ovarian mass, only 20 cases of malignancy were identified (3.5%) [(51)]. **Therefore, there is an unmet need for a non-invasive imaging tool that is capable of delineating ovarian epithelial carcinoma—the overall goal of this project.**

Because the degree of clinical suspicion of ovarian cancer is much greater for postmenopausal women than for premenopausal women, this diagnostic tool would be most useful for premenopausal women. More specifically, this tool would be most useful for patients who have a personal history or family history of BRCA 1/2 mutant breast or ovarian cancer as carriers of these mutations have been shown to have elevated risk of ovarian cancer [(52)]. Owing to the fact that the oophorectomy procedure causes immediate menopause, which increases the risk of conditions such as osteoporosis and heart disease among others, premenopausal women considering surgical resection should have a more sensitive and specific diagnostic tool to confirm malignant disease. Although the incidence of adnexal mass being malignant in premenopausal women is low (1-3:1000), the consequences of a false negative diagnosis are too great to ignore. In addition to diagnosis, the proposed radiotracer could be used as a tool to monitor response to treatment following surgical resection and adjuvant chemotherapy. Some of the limitations that are seen with the current methods for diagnosis of ovarian epithelial carcinoma can be addressed by using molecularly targeted imaging tracers providing a noninvasive approach. The specific targeting capability of antibodies to biomarkers expressed on the tumor cell surface makes immunoPET imaging an attractive platform for diagnosis of malignancies[(53)].

Zirconium-89 and ImmunoPET

Full, intact antibodies have an average biologic half-life of about 3 weeks and because of their size, can take two to four days to accumulate within tumor tissue while clearing from background tissue [54,55]. As such, this property necessitates the use of a radionuclide that has a corresponding physical half-life, in this case, zirconium-89 ($t_{1/2}$= 3.3 days)[56]. ^{89}Zr decays first by positron emission and electron capture to ^{89m}Y that then decays by gamma emission to stable ^{89}Y [55]. Previous studies have demonstrated that free ^{89}Zr is taken up primarily by the bone, joints and cartilage and DFO-^{89}Zr is taken up primarily by the liver [57].

An important consideration regarding the use of immunoPET is the risk of release of $^{89}Zr^{4+}$ from the antibody which could be detrimental to non-targeted tissues. Holland *et al.* examined the *in vivo* biodistribution of free ^{89}Zr-chloride and ^{89}Zr-oxalate by injecting mice with 300 μCi of each via the tail vein. They found that ^{89}Zr-chloride was mainly sequestered in the liver while ^{89}Zr-oxalate showed high accumulation in the bones, joints and cartilage [58]. To avoid the release of ^{89}Zr, a chelator that forms a stable complex with the ^{89}Zr is necessary. Over the years, several chelator have been used such as diethylenetriaminepentaacetic acid (DTPA), ethylenediaminetetraacetic acid (EDTA), 1,4,7,10-tetraacetic acid (DOTA), and desferoxiamine (DFO) [59]. Compared to ^{89}Zr-DTPA, ^{89}Zr-EDTA, and ^{89}Zr-DOTA, ^{89}Zr-DFO has been shown to be the most stable, and as such, DFO is currently the most common chelator for ^{89}Zr. Meijs *et al.* and Holland *et al* demonstrated that only 0.2% of ^{89}Zr was released from the ^{89}Zr-DFO complex after 24 hours in serum and after 7 days less than 2% had been released [57,59]. These favorable stability measurements encouraged investigators to develop several techniques for the conjugation of DFO to biomolecules [60-62]. A simplified method of DFO conjugation was developed by Perk *et al.* with the derivative *p*-isothiocyanatobenzyl-DFO which can be directly coupled to lysine residues of antibodies via a thiourea linkage [62]. An important consideration of this method of bioconjugation is the potential

for decreased immunoreactivity of the antibody due to the chelator interfering with the antigen-binding domain of the antibody. Work is currently being done to develop more controlled conjugation methods [63-66].

^{89}Zr-labeled antibodies directed against various malignancies have been investigated in many preclinical and clinical trials. Notably, human epidermal growth factor receptor 2 (HER2) has been the focus of many studies as this receptor is involved in angiogenesis, differentiation, metastasis, proliferation and cell survival and has been shown to be overexpressed in breast and ovarian cancer [67]. The anti-HER2 antibody trastuzumab was approved by the FDA for the treatment of HER2-positive breast cancer, but it has also been used as a molecular imaging targeting vector [68]. Chang *et al.* demonstrated that ^{89}Zr-labeled trastuzumab was able to specifically accumulate in HER2-positive murine tumor models. Further, the first human study using ^{89}Zr-trastuzumab was published in 2010 [69,70]. Fourteen breast cancer patients with HER2- positive metastatic disease received the radiolabeled antibody and PET scans that showed high uptake in the tumor lesions. All of the known tumors were detected in addition to lesions that had no previously been identified. This and other clinical studies have shown that ^{89}Zr-based immunoPET is capable of producing high-resolution images with high tumor uptake and good signal-to-noise ratio [71,72].

Molecular Target: MUC16

For the purposes of this study, we will be exploiting the overexpression of MUC16, a heavily glycosylated transmembrane mucin protein with a core peptide of 22,152 amino acids and molecular weight of 2.5 MDa [73]. This protein is found to be expressed at a basal level on the apical membranes of epithelial cells in the cornea, conjunctiva, the respiratory tract, and female reproductive tract. The outer portion of the MUC16 protein, once cleaved, is known as CA-125, a widely-used biomarker for ovarian epithelial carcinoma. The ectodomain contains the N- terminus, a

tandem repeat region with over 60 tandem repeats of 156 amino acids and a region with several SEA domain region that mediates the auto-cleavage (Figure 2.1) [74]. Several studies have shown that MUC16/CA-125 is overexpressed in various cancer types, including ovarian epithelial carcinoma. In addition, they demonstrate that this glycoprotein promotes cancer cell proliferation and inhibits anti-cancer immune responses [75-77]. In order to explore the biology of MUC16 more extensively, Rao *et al.* derived several murine monoclonal antibodies against the extracellular portion of MUC16 proximal to the CA-125 cleavage site [78]. The fact that these antibodies target the portion of the antigen that remains attached to the cell membrane following cleavage is advantageous because it minimizes binding of the tracer to shed serum antigen, thus lowering background organ uptake and increasing the signal to noise ratio. In this chapter, our goal is to validate this hypothesis and determine the optimal MUC16 antibody for imaging using an *in vitro* screen followed by *in vivo* characterization.

Results and Discussion

Bioconjugation and Radiolabeling

To begin with the bioconjugation of the antibodies to functionalized isothiocyanate desferrioxamine chelator (p-SCN-Bn-DFO), a concentrated solution of each antibody dissolved in PBS was pH adjusted to 8.5-9 and incubated with the chelator dissolved in DMSO at a 10:1 molar excess for 1 hour at 37 degrees Celsius. The modified antibodies were purified from the unreacted chelator using centrifugal filters (Amicon Ultra 50 kDa) and aliquoted and stored at -20 degrees Celsius. Each of the antibodies was then radiolabeled with ^{89}Zr in PBS for 60 minutes at 37 degrees Celsius. Radiochemical yields and specific activities were calculated using instant thin layer chromatography (ITLC) with a mobile phase of EDTA (pH 5.0, 50 mM) where the free ^{89}Zr

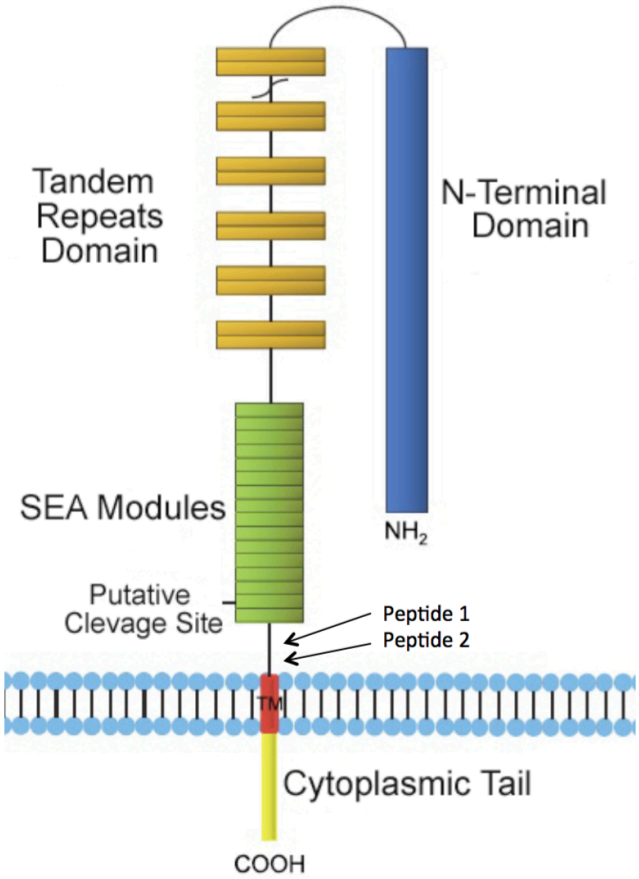

Peptide 1

Antibody	Subclass
9B11	IgG1
10A2	IgG1
2F4	IgG1
23D3	IgG2b
7B12	IgG1
28F8	IgG1

Peptide 2

Antibody	Subclass
4C7	IgG1
9C9	IgG2b
4H11	IgG2b
4A2	IgG1
4A5	IgG1
29G9	IgG1

Figure 2.1 Schematic of MUC16/CA-125 glycoprotein and panel of murine antibodies.
Murine MUC16 antibodies were raised against peptide sequences (1 and 2) highlighted by arrows pointing to region of glycoprotein proximal to the putative cleavage site. No *in vitro* or *in vivo* patterns were observed based on peptide origin of murine antibodies.

migrates with the solvent front and the chelated ^{89}Zr remains at the baseline. Specific activities for the antibodies varied from 0.21 μCi/μg to 5.74 μCi/μg (Figure A.2.1). In addition, one of the antibodies from the panel, 4A2, did not label at all with a radiochemical yield of 0.00% and specific activity of 0.0 μCi/μg. Nevertheless, the remaining 11 antibodies did in fact label with the majority of them (8 of the 11 remaining) having a specific activity of 3.19 μCi/μg or greater. The three leading candidates ^{89}Zr-7B12, ^{89}Zr-9C9, and ^{89}Zr-4H11 had radiochemical yields of 98%, 99% and 95% respectively, along with specific activities of 5.32, 4.35, and 5.74 μCi/μg, respectively (Figure 2.2).

Of course, in terms of imaging, the higher the specific activity, the more advantageous because this minimizes the risk of saturating binding sites within the target tissue, leading to higher relative uptake. The differences that we have observed in the specific activities of the antibodies are most likely due differences in the efficiency of the bioconjugation reactions. Although the exact same conditions were used, there were slight variations in the concentrations of the starting antibody solutions (12-14 mg/mL), but not enough variation to explain wide discrepancy in specific activities. Other possible reasons why four of the twelve antibodies had specific activities below 3 μCi/μg may lie in the actual primary or tertiary structure of the antibodies. As lysine residues are required for the DFO coupling, subtle differences in the number of lysines, or tertiary structure that obscures lysines could potential impact the bioconjugation reaction. In addition, subtle differences in the pH of the reaction mixture could have an impact as well.

Immunoreactivity

Due to the fact that we used a non-specific bioconjugation approach to couple DFO to the

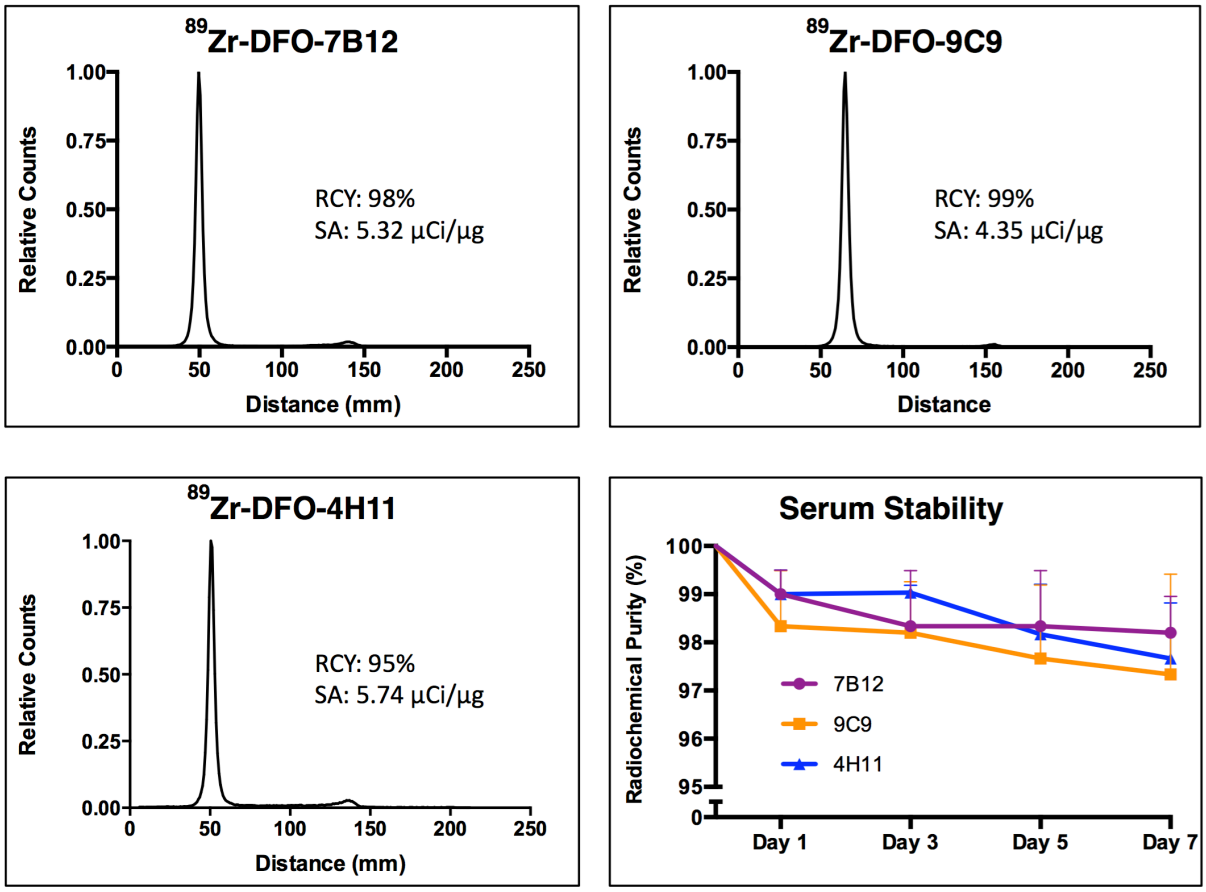

Figure 2.2. Radio-ITLC of lead antibody candidates and serum stability challenge.
The radio-ITLC chromatograms of radiolabeling reactions were acquired by spotting 1 µL of each reaction mixture on silica-gel impregnated glass-microfiber paper strips using 50 mM EDTA at pH 5 as the mobile phase. The antibody bound activity remained at baseline and crude radiochemical yield report as percentage of total radioactivity at baseline. Serum stability of the radioimmunoconjugates was assessed by incubating 100 µL of purified reaction mixture in 900 µL of human male AB+ serum at 37 degrees Celsius. Aliquots of radioimmunoconjugates (in triplicate) were assessed via radio-ITLC at the time points listed above.

antibodies, it is entirely possible that this step could be a negative effect on the ability of the antibodies to bind the target. For instance, if the chelator binds within the antigen binding site, it could disrupt sensitive antigen-antibody interactions, and as such, the next step in this screen is the immunoreactivity assay where a constant amount of radiolabeled antibody was incubated with increasing amounts of the antigen-positive ovarian cancer cell line, SKOV-3 [79]. Following a 1-hour incubation period and a series of PBS washes, the cell-associated activity was counted on a gamma counter. The panel of antibodies displayed a range of immunoreactivities from 61.5 ± 1.2 % to 88.3 ± 5.9 % with the lead candidates, ^{89}Zr-7B12, ^{89}Zr-9C9, and ^{89}Zr-4H11 displaying immunoreactivities of 86.7 ± 4.7 %, 84.6 ± 4.4 %, and 88.3 ± 5.9 %, respectively (Figures 2.3, A.2.1, A.2.2). The eight radiolabeled antibodies with the highest immunoreactive fractions (above our cutoff of 70%) were carried forward to the next screening assay.

Cell Saturation Binding

As opposed to the immunoreactivity assay which determines the fraction of antibody that is able to bind the target post-radiolabeling, the cell saturation binding assay (Scatchard assay) provides insight into how well, or how strongly the antibodies are able to bind yielding affinity (K_d) values. By incubating a constant amount of antigen-positive cells with increasing concentrations of radiolabeled antibody, we can determined the K_d values of the radiolabeled antibodies ranged from 6.37 ± 1.20 nM to 19.80 ± 1.09 nM with the three lead candidates, ^{89}Zr-7B12, ^{89}Zr-9C9, and ^{89}Zr-4H11 yielding values of 9.95 ± 1.24 nM, 9.02 ± 1.49 nM, and 6.37 ± 1.20 nM (Figures 2.4, A.2.1, A.2.3). Interestingly, these values are within close proximity to the K_d values obtained by Dharma Rao *et al.* who reported values ranging from 6.8 ± 0.6 to 8.6 ± 1.9 nM [36]. Our data suggest that the bioconjugation coupling and radiolabeling did not significantly affect the binding affinity of these MUC16 antibodies. From this point, we eliminated the antibodies that exhibited K_d values greater

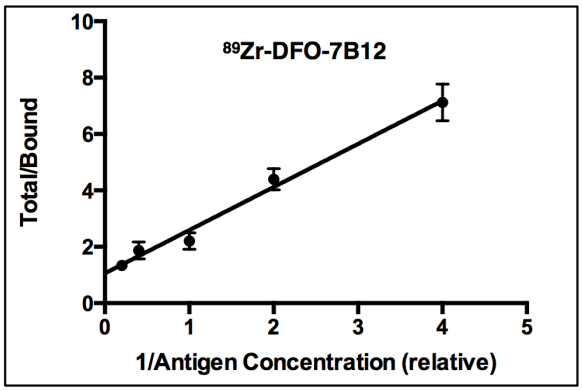

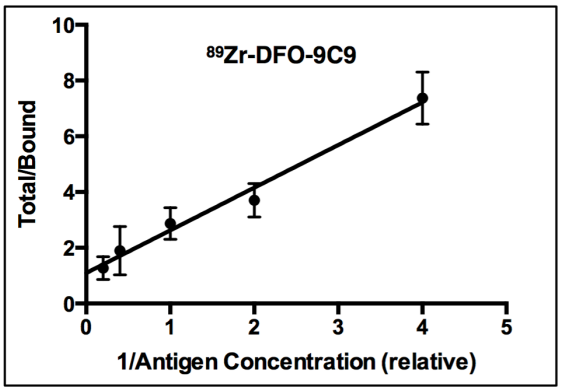

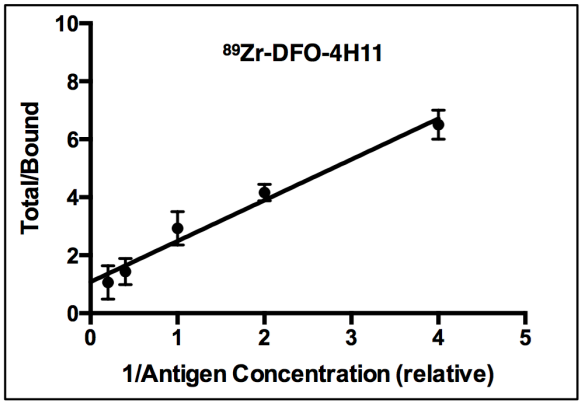

Antibody	Immunoreactivity
^{89}Zr-7B12	86.7 ± 4.7 %
^{89}Zr-9C9	84.6 ± 4.4 %
^{89}Zr-4H11	88.3 ± 5.9 %

Figure 2.3. Immunoreactivity assay of three leading candidates.
The radioimmunoconjugates were functionally characterized for binding to antigen-expressing cells (SKOV-3) and the determination of the immunoreactive fraction via Lindmo assays [79]. Aliquots of each radioimmunoconjugate, 50 µL of 1 µCi/mL stock were added to tubes containing 5.0 x 10^5 – 5.0 x 10^6 cells/mL (in triplicate) in 500 µL PBS, 1% BSA (pH 7.4 to a final volume of 550 µL). Cell bound activity was counted and data graphed on double-reciprocal plot. Immunoreactive fractions are presented as mean percentages of triplicate samples ± SEM.

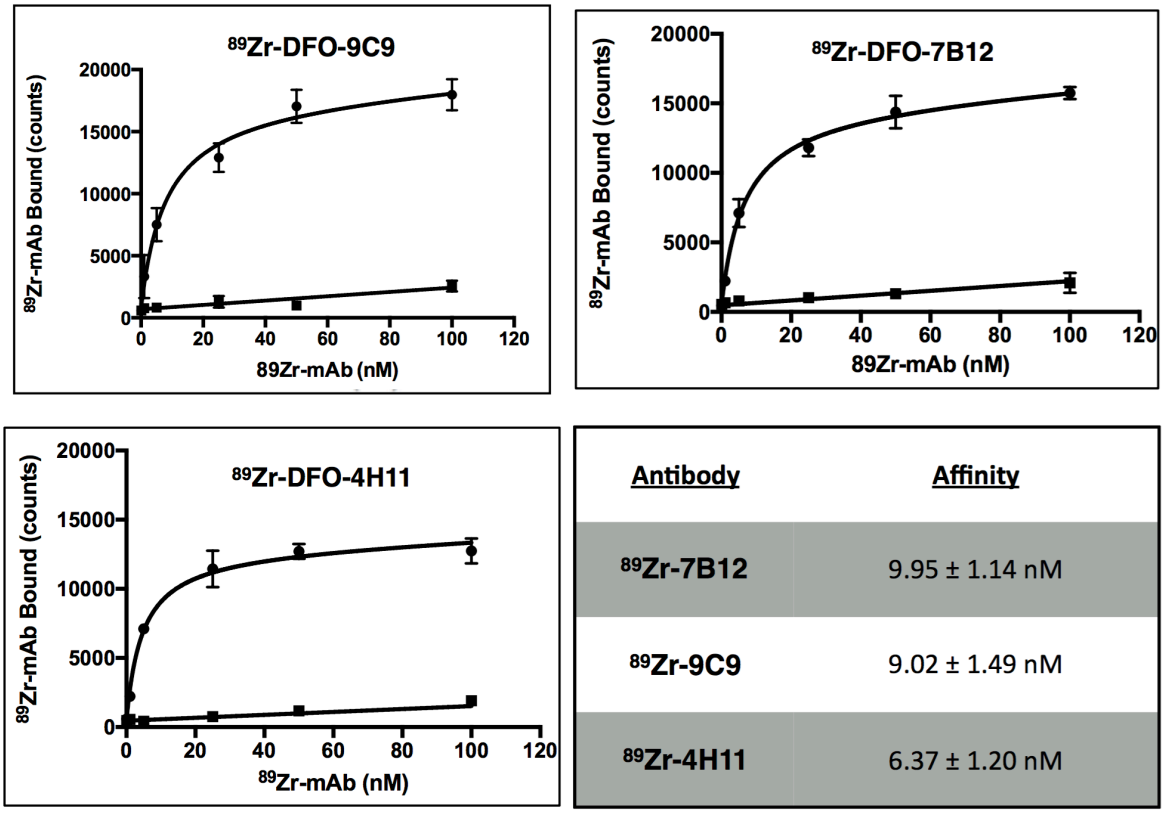

Antibody	Affinity
^{89}Zr-7B12	9.95 ± 1.14 nM
^{89}Zr-9C9	9.02 ± 1.49 nM
^{89}Zr-4H11	6.37 ± 1.20 nM

Figure 2.4. Cell saturation binding assay of three leading candidates.
The radioimmunoconjugates were characterized for binding to antigen-expressing cells (SKOV-3) and the K_D values were calculated. 5.0 x 10^6 cells were incubated with increasing nanomolar concentrations of each radioimmunoconjugate. Following washes, cell bound activity was counted and data graphed using Prism 7 Software. Affinity values were calculated and presented as mean value of triplicate samples ± SEM.

than 10 nM from the screen (28F8: 19.80 ± 1.09 nM, 4C7: 13.29 ± 2.89 nM, 9B11: 13.80 ± 2.92 nM).

In Vitro Cell Uptake

We next investigated the extent to which each of the remaining five antibodies were internalized by the antigen positive cell line, SKOV-3. In terms of molecular imaging, antibodies that are actively uptaken by tumor tissue are advantageous in the sense that the cells, in essence, capture the radioactive isotope and sequester it from other tissues. Further, as a radiometal, ^{89}Zr is residualized within the cells following internalization as it is incorporated into cellular proteins. This is in contrast to other commonly used isotopes such as ^{131}I which is effluxed from cells after internalization. Briefly, we incubated each of the radiolabeled antibodies with SKOV-3 cells for various time points and washed with PBS, followed by acid, followed by base to collect the unbound antibody, cell surface bound antibody, and internalized antibody, respectively. This protocol was followed at both 37 degrees and 4 degrees Celsius as a negative control for active internalization.

All five of the antibodies were shown to be actively internalized, albeit at different rates over a 24 hour period (Figures 2.5, A.2.1, A.2.4). ^{89}Zr-7B12 exhibited a rapid uptake to 4.24 ± 0.62 % normalized dose by 1 hour and then a very gradual internalization to 8.41 ± 0.59 % by 24 hours. Similarly, ^{89}Zr-9C9 exhibited a rapid internalization to 5.22 ± 1.34 % by 1 hour followed by gradual accumulation to 11.89 ± 2.21 % normalized dose by 24 hours. Most notably, ^{89}Zr-4H11 exhibited the fastest uptake with 12.47 ± 3.02 % of the normalized dose being internalized by 4 hours followed by a slow accumulation to 14.09 ± 1.34 % by 24 hours (Figure 2.5). The two inferior antibody candidates (^{89}Zr-2F4 and ^{89}Zr-23D3) did internalize, but less than 5% of the normalized dose after 24 hours (Figure A.2.4). It is curious that all five of these antibodies show varying rates and different maximal cell internalization values given that they were all raised against the same

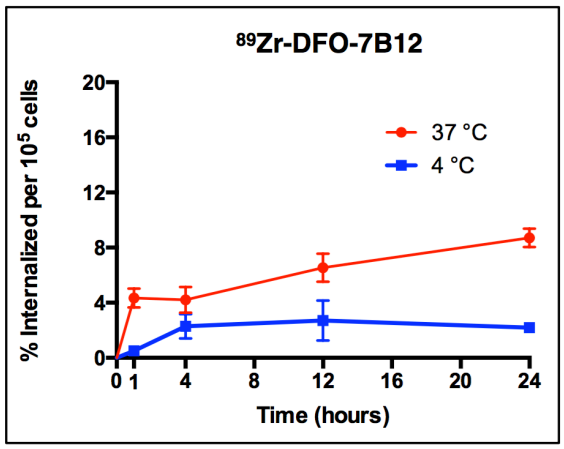

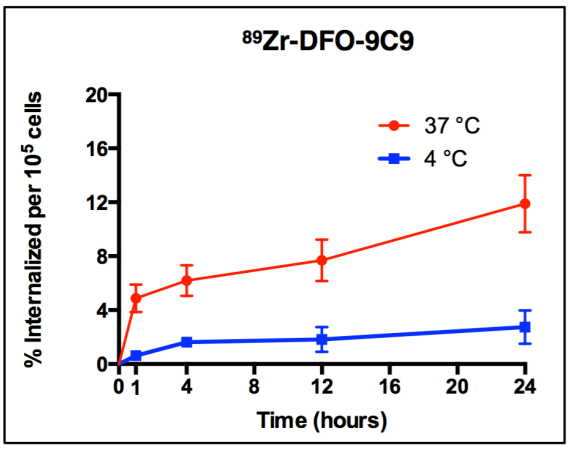

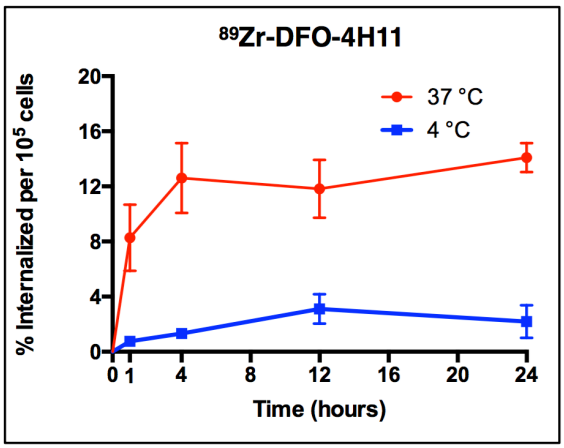

Antibody	Cell Uptake
^{89}Zr-7B12	8.41 ± 0.59 %ID
^{89}Zr-9C9	11.89 ± 2.21 %ID
^{89}Zr-4H11	14.09 ± 1.34 %ID

Figure 2.5. Internalization assay of three leading MUC16 radioimmunoconjugate candidates.

Internalization of each radioimmunoconjugate was investigated on SKOV-3 cells. 1×10^5 cells were incubated for 1-24h with 2 mL of radioimmunoconjugate (1μCi/mL) at 37 and 4 degree Celsius. The percent internalized activity was calculated as the ratio of the activity of the washed lysate and the total activity. Uptake values reported as mean of triplicate samples ± SEM.

segment of antigen, MUC16. A possible reason for this could be the geometry of binding of each of these antibodies. It could be the case that each of the antibodies binds at a slightly different angle or conformation such that they have different proximities to the cell membrane. It would follow that antibodies that bind closer to the membrane would be uptaken more rapidly.

Serial PET Imaging

At this point, we have been able to narrow down our panel of twelve MUC16 antibodies to the three leading candidates (^{89}Zr-7B12, ^{89}Zr-9C9, ^{89}Zr-4H11). To assess these tracers *in vivo*, we performed serial PET imaging with female, athymic nude mice bearing subcutaneous SKOV-3 xenografts. The radiolabeled immunoconjugates were injected via the tail vein and PET images were acquired at 4 time points post-injection (24, 48, 72 and 96h). Presented in all of the imaging figures are coronal slices of the mice through the tumor tissue (all scaled from 0 to 20 % injected dose per gram) and maximal intensity projections (MIP) representing the total body image.

For ^{89}Zr-7B12 (Figure 2.6), despite its favorable *in vitro* cell uptake values, we observe at limited uptake of the tracer in the tumor tissue throughout the entire time course. The liver at 24h ours and throughout the 96 hours appears to be the organ with the most activity followed by the spleen. These are both organs with prominent reticuloendothelial cells so the high uptake in these organs may be due to aggregation of the tracer. There is also prominent bone uptake with this tracer that continues to gradually accumulate throughout 96 hours.

The ^{89}Zr-9C9 (Figure 2.7) images show somewhat of an improvement from ^{89}Zr-7B12. The is slow accumulation of the tracer within the tumor that intensifies beginning at 48 hours post-injection and continues to accumulate throughout 96 hours. Similar to ^{89}Zr-7B12, there is liver

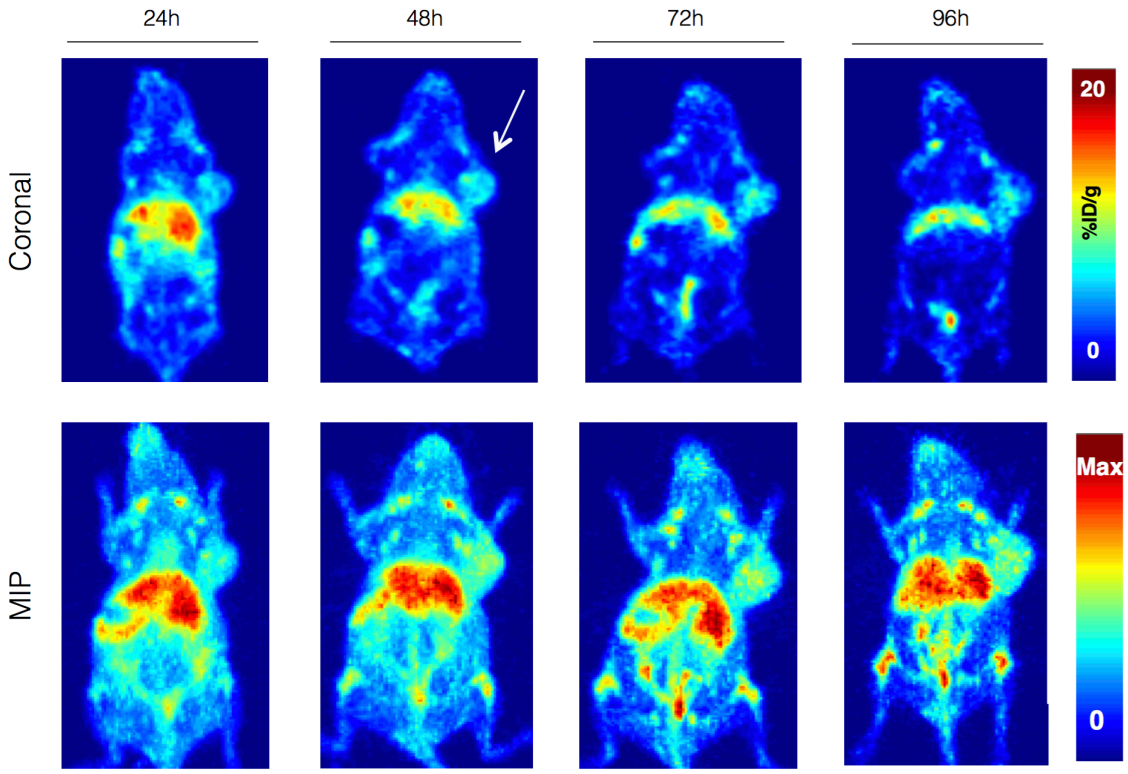

Figure 2.6. Serial PET imaging of ^{89}Zr-DFO-7B12
Small-animal PET imaging in a subcutaneous ovarian cancer tumor model revealing limited tumor uptake and high background tissue activity. Representative coronal and maximal intensity projection (MIP) PET images of ^{89}Zr-DFO-7B12 (168-176 μCi in 150 μL of PBS injected via tail vein) in athymic nude mice bearing subcutaneous MUC16-positive SKOV-3 tumors xenografted on the right shoulder (white arrow). Coronal planar images intersect the middle of the tumor.

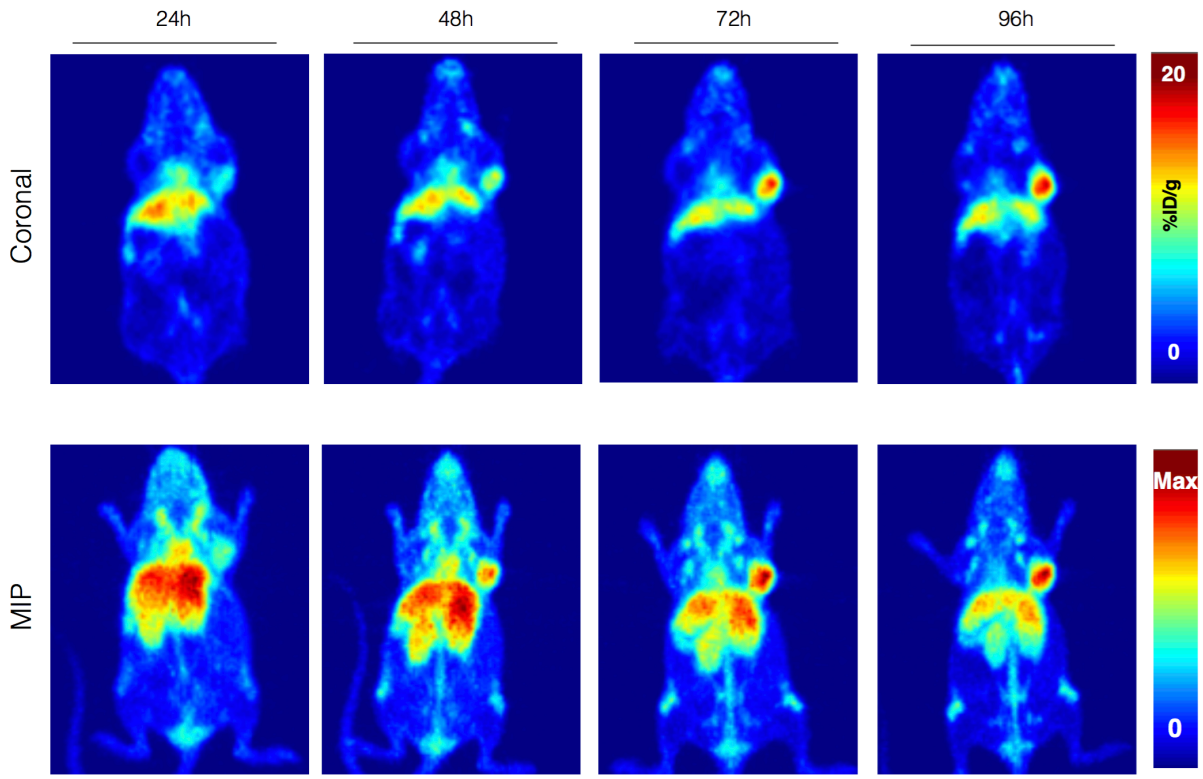

Figure 2.7. Serial PET imaging of ^{89}Zr-DFO-9C9
Small-animal PET imaging in a subcutaneous ovarian cancer tumor model revealing high tumor uptake as well as liver and kidney activity. Representative coronal and maximal intensity projection (MIP) PET images of ^{89}Zr-DFO-9C9 (181-194 μCi in 150 μL of PBS injected via tail vein) in athymic nude mice bearing subcutaneous MUC16-positive SKOV-3 tumors xenografted on the right shoulder (white arrow). Coronal planar images intersect the middle of the tumor.

uptake at 24 hours, but it slowly clears from the liver throughout 96 hours. Further, this tracer shows kidney uptake that is visualized at 24 hours and slows clears through 96 hours, but not completely. This kidney uptake could potential be a sign of fragmentation of the antibody *in vivo*.

For the final tracer, ^{89}Zr-4H11, the images are much clearer of background organ activity (Figure 2.8). The tracer accumulates very rapidly beginning at 24 hours and continuing to accumulate through 96 hours, similar to what was seen in the *in vitro* cell uptake study (Figure 2.5). There is liver uptake that dissipates from 24 hours to 96 hours. Interestingly, there are 4 bilateral structures that are illuminated at all time points in the maximal intensity projections. We have identified these structures as the submandibular and axillary lymph nodes. Histopathological analysis of these lymph nodes by the Laboratory of Comparative Pathology revealed no signs of neoplastic cells within these nodes and instead noted histiocytosis and hyperplasia consistent with drainage reaction. Because ovarian cancer has a propensity to invade lymph nodes, this phenomenon of false positives may have be a hurdle in terms of clinical translation.

Ex Vivo Biodistribution

To confirm the PET imaging results and to verify specificity of the tracers, *ex vivo* biodistribution studies were performed (Figure 2.9). The radiolabeled immunoconjugates were injected via tail vein into female athymic nude mice bearing SKOV3 tumors and various organs were collected at 96 hours post-injection, analyzed on a gamma counted, and weight normalized. The results of these studies confirm the trends that were revealed in the imaging data. The tumor uptake values at 96 hours post-injection for ^{89}Zr-7B12, ^{89}Zr-9C9, and ^{89}Zr-4H11 were 5.34 ± 1.14 % ID/g, 18.76 ± 2.63 % ID/g, and 17.44 ± 2.89 % ID/g, respectively. These values correspond with the PET images, most notably for ^{89}Zr-7B12 which had very little uptake within the tumor according to the images. By co-injecting with 50-fold excess cold antibody, we were able to significantly lower the

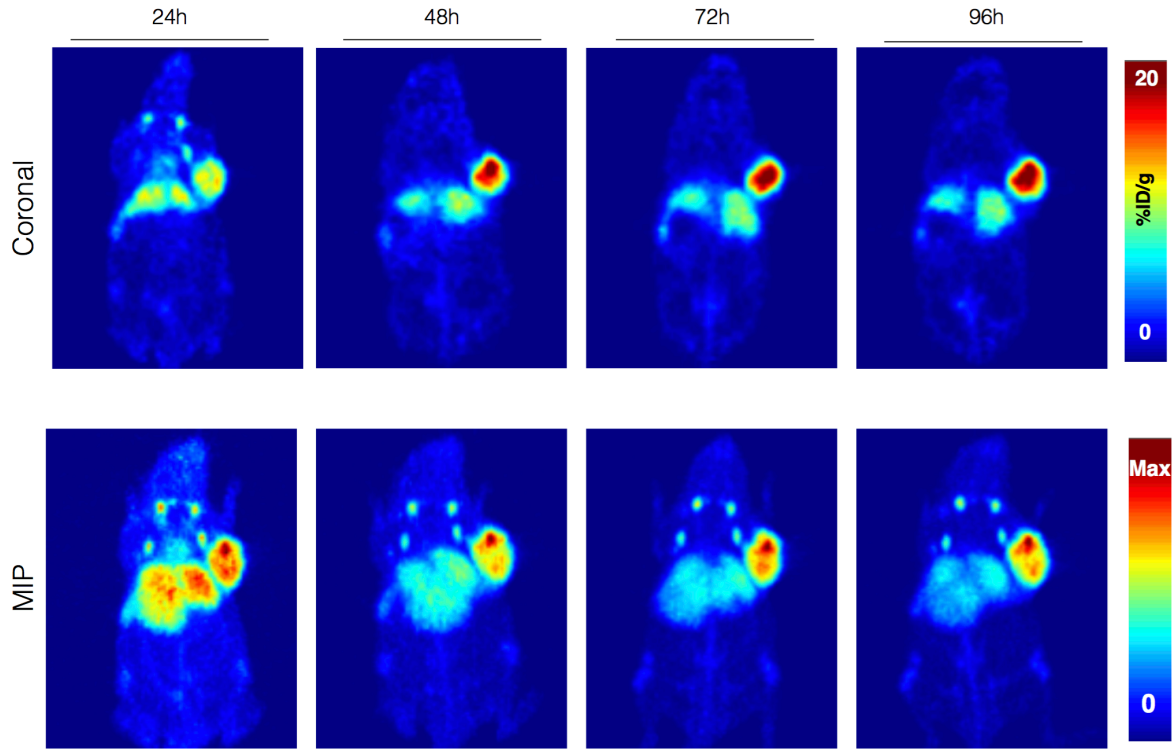

Figure 2.8. Serial PET images of ^{89}Zr-DFO-4H11
Small-animal PET imaging in a subcutaneous ovarian cancer tumor model revealing high tumor radioactivity concentration and lymph node activity. Representative coronal and maximal intensity projection (MIP) PET images of ^{89}Zr-DFO-4H11 (173-187 μCi in 150 μL of PBS injected via tail vein) in athymic nude mice bearing subcutaneous MUC16-positive SKOV-3 tumors xenografted on the right shoulder (white arrow). Coronal planar images intersect the middle of the tumor.

tumor uptake values for ^{89}Zr-9C9 and ^{89}Zr-4H11 to 6.86 ± 1.92 % ID/g and 7.26 ± 2.13 % ID/g, signifying specific uptake of the hot tracers. Because the uptake of ^{89}Zr-7B12 was already quite low to begin with, co-injection with 50-fold excess of the antibody did not significantly decrease the uptake of the hot tracer, signifying non-specific uptake. The high liver uptake that was seen in the PET images of ^{89}Zr-7B12 was also confirmed by *ex vivo* biodistribution as the uptake value was 16.98 ± 2.23 % ID/g as compared to 8.91 ± 2.14 % ID/g and 6.23 ± 1.21% ID/g for ^{89}Zr-9C9 and ^{89}Zr-4H11. Further, the high kidney uptake visualized with ^{89}Zr-9C9 was confirmed to be 11.08 ± 2.38% ID/g while it was 5.88 ± 1.19 % ID/g and 4.27 ± 0.94% ID/g for ^{89}Zr-7B12 and ^{89}Zr-4H11. Interestingly, the lymph node uptake for ^{89}Zr-4H11 registered at 11.53 ± 2.82 % ID/g while ^{89}Zr-7B12 and ^{89}Zr-9C9 had values of 6.76 ± 1.98 % ID/g and 4.24 ± 0.49 % ID/g.

The goal of this screen was to find the optimal radiolabeled antibody against MUC16 from the panel of 12. Ultimately, the best antibody would have the highest tumor uptake with the lowest background organ uptake. Although the tumor uptake of ^{89}Zr-9C9 is slightly higher, within error, at 96h post-injection, ^{89}Zr-4H11 had significant tumor uptake beginning at 24 hours whereas ^{89}Zr-9C9 had significant uptake later on at 72 hours. This 48 hour time difference for tumor uptake of the tracers is important because it implies that delivery of the radiolabeled ^{89}Zr-4H11 to the tumor tissue is the quickest of 3 tracers so we would potentially be able to image human patients sooner post-injection with ^{89}Zr-4H11. Also, in terms of a potential radioimmunotherapy application, this is also a desirable characteristic because ^{89}Zr-4H11 appears to have a higher tumor activity residence time and less off-target tissue uptake.

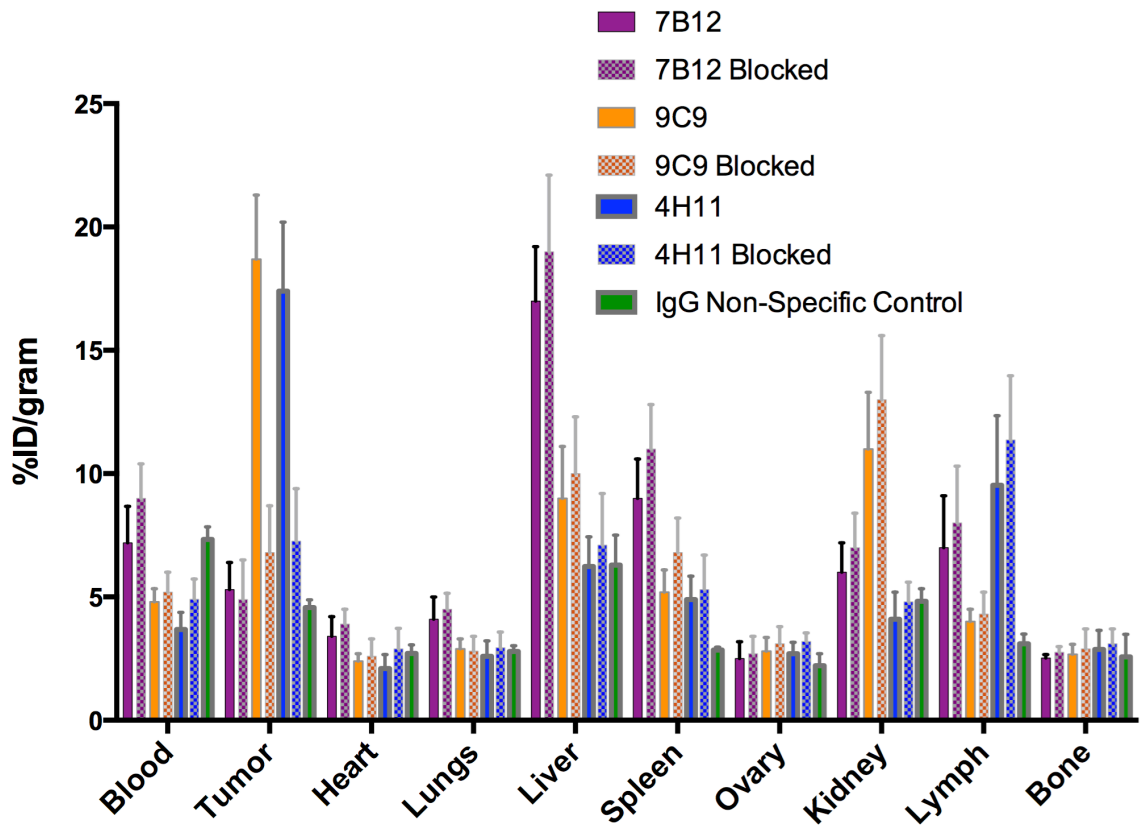

Antibody	Tumor : Blood	Tumor : Liver	Tumor : Kidney
^{89}Zr-7B12	0.74	0.26	0.71
^{89}Zr-9C9	3.62	1.78	1.65
^{89}Zr-4H11	4.37	2.91	4.61

Figure 2.9. *Ex vivo* biodistribution of three leading candidates 96h post-injection and tumor-to-tissue ratios

Acute biodistribution of radioimmunoconjugates in SKOV-3 tumor-bearing mice. Biodistribution data from athymic nude mice (n = 4 per group) following the administration of ^{89}Zr-DFO-7B12, ^{89}Zr-DFO-9C9, and ^{89}Zr-DFO-4H11 via tail vein injection (21-29 μCi, 3.6–6.6 μg). A 50-fold excess was co-injected for the blocking groups. Tumor-to-tissue ratios calculated from %ID/g values.

Conclusions

In this study, we set out to determine the optimal ^{89}Zr radiolabeled antibody for PET imaging of ovarian cancer beginning with a panel of murine antibodies targeting the highly overexpressed glycoprotein, MUC16. We conducted a series of *in vitro* assays to narrow down the panel to those with the highest specific activity, highest immunoreactivity, highest affinity, and highest and fastest internalization. We hypothesized that these *in vitro* properties would predict for a tracer that, at an *in vivo* level, produce quality images with high tumor-to-background activity. ^{89}Zr-4H11 met all of the criteria that we set with the highest immunoreactivity, the highest affinity, the highest specific activity, and the highest and most rapid internalization *in vitro.* Further, *in vivo* ^{89}Zr-4H11 performed the best as well with the highest tumor-to-background organ ratios all around (Figure 2.9). ImmunoPET with ^{89}Zr-4H11 is a potential strategy for the noninvasive imaging of ovarian cancer and further work is currently underway to characterize the humanized version of this antibody to push it one step closer to being evaluated as a diagnostic tool in man.

Materials and Methods

General Laboratory Procedures

Unless otherwise noted, all chemicals were acquired from Sigma-Aldrich (St. Louis, MO) and used as received and all instruments were calibrated and maintained in accordance with standard procedures. ^{89}Zr was produced at Memorial Sloan Kettering Cancer Center on a TR19/9 cyclotron (Ebco Industries Inc.) via the ^{89}Y(*p,n*)^{89}Zr reaction and purified to yield ^{89}Zr with a specific activity of 196–496 MBq/mg. Activity measurements were made using a CRC-15R Dose Calibrator (Capintec). For the quantification of activities, samples were counted on an Automatic Wizard

gamma counter (Perkin Elmer). The radiolabeling of ligands was monitored using instant thin-layer chromatography paper (Agilent Technologies) and analyzed on a Bioscan AR-2000 radio-ITLC plate reader using Winscan Radio-TLC software (Bioscan Inc., Washington, DC). All *in vivo* experiments were performed according to protocols approved by the Memorial Sloan Kettering Institutional Animal Care and Use Committee (Protocol 08−07−013).

Cell Culture

T-75 flasks (Corning, Corning NY) containing cells were stored in cell incubators maintained at 37 °C and a 5% CO_2 concentration. SKOV3-phrGFP-MUC16^{c114} (SKOV-3), a human epithelial ovarian carcinoma cell line (ATCC, Manassas, VA) transfected with MUC16 was cultured in RPMI McCoy's 5A Medium, modified to contain 1.5 mM L-glutamine, were all grown with 100 units/mL penicillin G and 100 μg/mL streptomycin and 10% fetal bovine serum and 800 μg/mL of G418. The SKOV-3 cell line was subcultivated once per week using 0.25% trypsin/0.53 mM EDTA in Hank's Buffered Salt Solution without calcium and magnesium and passaged 1:5 for standard cell line passaging.

Xenograft Mouse Models

Eight to ten week old athymic nu/nu female mice were purchased from Charles River Laboratories (Kingston, NY). Animals were housed in ventilated cages, were given food and water ad libitum, and were allowed to acclimatize for approximately 1 week prior to inoculation. SKOV3-phrGFP-MUC16^{c114} (SKOV-3) tumors were induced on the right shoulder by a subcutaneous injection of 5.0×10^6 cells in a 150 μL cell suspension of a 1:1 mixture of fresh media/BD Matrigel (BD Biosciences, Bedford, Ma). Experiments were performed approximately 2-3 weeks following the injection of the cancer cells.

Antibody Bioconjugation

Antibodies were obtained in PBS at an average concentration of 2-3 mg/mL. The antibodies were concentrated using centrifugal filter units with a 50,000 molecular weight cutoff (Amicon Ultra 4 Centrifugal Filtration Units, Millipore Corp., Billerica, MA) to a final concentration of 12-15 mg/mL. After concentrating, the antibodies were pH adjusted to 8.5-9.0 with 0.1 M Na_2CO_3 before the addition of 10 equivalents of *p*-SCN-Bn-DFO (Macrocyclics, Inc. Dallas, TX) dissolved in DMSO. The reaction was incubated at 37 degrees Celsius for 1 h constantly shaking at 500 rpm. The antibodies were purified using centrifugal filter units with a 50,000 molecular weight cutoff (Amicon Ultra 4 Centrifugal Filtration Units, Millipore Corp., Billerica, MA) to purify the ligand-antibody conjugate. The final bioconjugates were aliquoted and stored in PBS pH 7.4 at -80 degrees Celsius.

^{89}Zr Radiolabeling

^{89}Zr was received after target processing as ^{89}Zr-oxalate in 1.0 M oxalic acid. The solution was neutralized with 1.0 M sodium carbonate to reach pH ~7. DFO-antibodies were incubated together with neutralized ^{89}Zr labeled in PBS pH 7.4 at 37 degrees Celsius for 60 minutes. The progress of the reactions was monitored via radio-ITLC with silica-gel impregnated glass-microfiber paper strips (iTLC-SG, Varian, Lake Forest, CA) (analyzed by AR-2000, Bioscan Inc., Washington, DC). using 50 mM EDTA at pH 5 as the mobile phase. ^{89}Zr-DFO-antibody complexes remained at the origin, while free ^{89}Zr was taken up by EDTA in the mobile phase and migrated along solvent front. Crude radiochemical yields were calculated using the radio-ITLC data. ^{89}Zr labeled antibodies were then purified using size-exclusion chromatography (PD10), followed by centrifugal filtration to concentrate the final volume for formulation. The radiochemical purity of the final purified radiolabeled antibodies was confirmed to be >99% by radio-ITLC before use.

Serum Stability

Aliquots of each ^{89}Zr-antibody complex (100 μL) were incubated with 900 μL of human serum and agitated constantly on a thermomixer at 37 degrees Celsius. Samples were taken from each microcentrifuge tube and analyzed using radio-ITLC at day 0, 1, 3, 5, and 7 in triplicate. The stability of the complexes was measured as the percentage of ^{89}Zr that was retained at the origin of the radio-ITLC strip and reported as % intact.

Immunoreactivity

The immunoreactive fraction of the ^{89}Zr-DFO-antibodies was determined using a cell binding assay following procedures derived from Lindmo *et al* [79]. To this end, SKOV-3 cells were suspended in microcentrifuge tubes at concentrations ranging from 5.0 x 10^5 – 5.0 x 10^6 cells/mL in 500 μL PBS, 1% BSA (pH 7.4). Aliquots of ^{89}Zr-DFO-antibody (50 μL of 1 μCi/mL stock were added to each tube to a final volume of 550 μL. The samples were incubated on a thermomixer for 60 min at 37 degrees Celsius. The treated cells were then pelleted via centrifugation (1400 RPM for 4 min), aspirated supernatant, and washed three times with cold PBS before removing the supernatant and counting the cell-associated radioactivity. The activity data were background-corrected and compared with the total number of counts in appropriate control samples. Immunoreactive fractions were determined by linear regression analysis of a plot of (total/bound) activity against (1/[normalized cell concentration]).

Internalization Assay

Internalization of each ^{89}Zr-mAb was investigated on SKOV-3 cells. Approximately 1 × 10^5 cells were seeded in a 12-well plate and incubated overnight. A volume of 2 mL of radiolabeled

protein (1μCi/mL) was added to each well. The plates were incubated at 37 and 4 °C for 1−24 h. Following each incubation period, the medium was collected and the cells were rinsed with 1 mL of phosphate buffered saline (PBS) twice. Surface-bound activity was collected by washing the cells in 1 mL of 100 mM acetic acid + 100 mM glycine (1:1, pH 3.5). The adherent cells were then lysed with 1 mL of 1 M NaOH. Each wash was collected and counted for activity. The percent internalized activity was calculated as the ratio of the activity of the lysate and the total activity from the medium, PBS, acid, and base washes.

PET Imaging

PET imaging experiments were conducted on an Inveon PET/CT scanner (Siemens Healthcare Global). Female, athymic nude mice with SKOV-3 xenografts on their right shoulders were administered ^{89}Zr-antibody (168-194 μCi in 150 μL of PBS) via intravenous tail vein injection. Animals were anesthetized by inhalation of 2% isoflurane (Baxter Healthcare, Deerfield, IL) and medical air gas mixture and placed within the scanner with anesthesia maintained using 2% isoflurane and medical air gas mixture. PET data for each mouse were recorded via static scans at 24, 48, 72, and 96 hours post-injection. An energy window of 350-700 keV and a coincidence timing window of 6 ns were used. Data were sorted into 2D histograms by Fourier rebinning, and transverse images were reconstructed by filtered back-projection (FBP) into a 128 × 128 × 63 (0.72 × 0.72 × 1.3 mm^3) matrix. The counting rates in the reconstructed images were converted to activity concentrations (percentage injected dose per gram of tissue, %ID/g) by use of a system calibration factor derived from the imaging of a mouse-sized water-equivalent phantom containing ^{89}Zr. Images were analyzed using ASIPro VM software (Concorde Microsystems).

Biodistribution

Biodistribution studies were performed using the ^{89}Zr-antibodies SKOV3 tumor-bearing female, athymic nude mice. Animals were administered (21-29 μCi) of each of the ^{89}Zr-antibodies in 150 μL PBS) via intravenous tail vein injection. For blocking groups, animals were co-injected with 50-fold excess of cold antibody. Animals (n = 4 per group) were euthanized by CO_2 asphyxiation at 96 hours post-injection. Following euthanasia, 17 organs (blood, tumor, heart, lungs, liver, spleen, stomach, large bowel, small bowel, pancreas, ovary, kidney, bone, muscle, lymph, skin, tail) were collected, weighed, and assayed for radioactivity on a gamma counter calibrated for ^{89}Zr. Counts were converted into activity using a calibration curve generated from known standards. Count data were background and decay corrected to the time of injection, and the percent injected dose per gram (%ID/g) for each tissue sample was calculated by normalization to the total activity injected. The data depicted in this study are expressed as averages ± standard deviation. Statistical differences were analyzed by unpaired, two-tailed, student's t-test using GraphPad Prism 7 software. P-values <0.05 were considered statistically significant and indicated by an asterisk.

CHAPTER 3: Differential Biodistribution of L1CAM Targeted Antibodies Based on Fc Region Modifications and Radioimmunotherapy Application

Introduction

As our group has seen with many radiolabeled antibodies in the past, there can be, depending on the targeted antigen and tumor model, retention and accumulation of the tracer within lymph nodes. This is especially true for antigens that are secreted from the cell of origin into the serum and immune complexes are drained through the lymphatic system. A recent study published by Sharma *et al.* explored this phenomenon within the context of epithelial ovarian cancer with a ^{89}Zr-radiolabeled antibody targeting MUC16 using an OVCAR3 xenograft model. They concluded that the lymph node uptake observed was, in fact, a true signal as the presence of neoplastic cells, metastasis from the implanted subcutaneous xenograft, was confirmed on *ex vivo* histology[80]. In our experience, however, the lymph node uptake that we previously observed post-tracer injection using a SKOV-3 subcutaneous xenograft model was a false positive signal as *ex vivo* histology confirmed the absence of neoplastic cells from the lymph nodes that were collected (Figure 2.6). **To that end, we hypothesize that the lymph node tracer uptake that we observed is due to: (1) local expression of the antigen within the lymph nodes and/or (2) binding of the Fc region of the antibodies to Fc receptors within the lymph nodes.**

Molecular Target: L1CAM

In order to examine this hypothesis and to determine if this phenomenon is tracer-specific, we developed a panel of humanized antibodies targeting a different antigen, L1 cell adhesion molecule (L1CAM). L1-cell adhesion molecule (L1CAM) is a 200-220 kDa cell surface glycoprotein

of the immunoglobulin superfamily critical for normal development of the central nervous system. It is overexpressed in human malignancies including neuroblastoma, epithelial ovarian carcinoma, melanoma, renal carcinoma, and gastrointestinal cancer. L1CAM has also been implicated in a variety of cancer processes including tumor progression and metastasis[81-84]. In addition, overexpression of L1CAM has been shown to be associated with a poorer outcome in ovarian cancer patients[85]. Similar to MUC16, it has also been shown that L1CAM is cleaved and released into the serum and ascites of patients with ovarian epithelial carcinoma[86].

The overall goal of these studies is to shed light on the previously observed lymph node uptake by evaluating the effect of modifications within in the Fc region of humanized antibodies on their *in vivo* biodistribution. Molecular imaging techniques most certainly provide us with a non-invasive approach to visualize these antibodies *in vivo* and enable us to gain insight into the underlying biology of the Fc region of antibodies.

IgG and Fc Region Biology

In humans, there are four subclasses of IgG antibodies (IgG1, IgG2, IgG3, and IgG4), which can be broken down into further subtypes. In addition, there are several types of Fc receptors, with those that bind IgG antibodies classified as Fc gamma receptors. The Fc gamma receptors can be further subdivided into classes that are differentially expressed on immune cells with Fc gamma receptor I having the highest affinity for IgG antibodies[87]. IgG1 antibodies are the most abundant in humans and have the highest affinity for activating Fc gamma receptors[88]. In addition, the sugar moieties, or glycosylation state, of IgGs play a large role in the binding to Fc gamma receptors. Specifically, for IgG1 antibodies, the sugar moieties attached to the N297 residue on the constant region interact with and alter Fc binding characteristics of the antibody[89]. The complex sugar moieties attached to this residue include mannose and N-acetylglucosamine (GlcNac) along with

other branching sugars including fucose, galactose, and sialic acid and alteration of this glycosylation site can dramatically affect binding[90,91]. IgG antibodies with an entire deletion of these sugars demonstrate significantly reduced Fc gamma receptor binding. On the other hand, removal of fucose residues from the glycosylation site greatly increases the affinity of the IgG for the Fc gamma receptor[90]. While IgG1 antibodies have the highest affinity for Fc gamma receptor, IgG4 antibodies, which represent the least abundant IgG in humans, have a significantly lower affinity for the Fc gamma receptor and is generally viewed as an anti-inflammatory IgG that dampens immune responses as a regulatory mechanism. This is thought to be due, in part, to the intrinsic property of IgG4 antibodies known as dynamic fab arm exchange[92].

IgG Structure

All the subclasses of IgG antibodies are composed of two heavy-light chain pairs that are bound together by disulfide bonds made by cysteine residues on the heavy chain located in the hinge region of the antibody. This hinge region is variable in length, along with the number of disulfide bonds, depending on the subclass of the IgG. These characteristics influence the flexibility of the hinge region and play a role in the binding affinities to the Fc gamma receptor[93]. With IgG4 antibodies, the two half-molecules (heavy-light chain pair) are able to disassociate with one another at the hinge region and recombine spontaneously with other half-molecules to form bispecific, monovalent antibodies *in vitro* an *in vivo* [54,94]. This dynamic Fab arm exchange property can be disabled in IgG4 antibodies by the introduction of a serine to proline mutation (S228P) within the hinge region of the antibody[95]. It is important to note that the experiments performed in this study utilize humanized antibodies in mice expressing mouse Fc gamma receptors. Although the Fc gamma receptors in man and mouse are only 60-70% homologous, recent studies have shown that human IgGs bind to the orthologous mouse Fc gamma receptors with very similar affinities suggesting similar biological activities[96,97].

L1CAM Antibody Modifications

In order to investigate the effects of the Fc region on the *in vivo* biodistribution of radioimmunoconjugates, we have developed a panel of humanized IgG1 and IgG4 antibodies, all of which have the exact same antigen binding site, but have modifications in the Fc region, and thus, alterations in their affinity for the Fc gamma receptors (Figure 3.1). HuE71-1 MAGE is an IgG1 antibody against L1CAM with glycans lacking α-1,6-fucose that was produced in CHO cells that were deficient in in the enzyme, UDP-N-acetylglucosamine: α-3-d-mannoside-β-1,2-N-acetylglucosaminyltransferase I (GnT1), effectively enhancing the Fc region[98]. HuE71-1 WT is the wildtype variant of this antibody produced in wildtype CHO cells while HuE71-1 Aglyco is the aglycosylated variant that contains a N297A mutation diminishing its Fc gamma receptor binding. HuE71-4 WT is the IgG4 variant of this antibody while HuE71-4 Mutant contains a S228P mutation preventing dynamic fab arm exchange from occurring. Finally, HuCtrl-4 is an IgG4 wildtype antibody targeting GD2, a non-specific antigen in the animal model used for this study.

Results and Discussion

Conjugation and Radiolabeling

For the conjugation of the antibodies to functionalized isothiocyanate desferrioxamine chelator (p-SCN-Bn-DFO), a concentrated solution of each antibody dissolved in PBS was pH adjusted to 8.5-9 and incubated with the chelator dissolved in DMSO at a 10:1 molar excess for 1 hour at 37 degrees Celsius.

Following spin filter purification of the antibodies (Amicon Ultra 50 kDa), aliquots were frozen and samples of the starting material (unconjugated antibody) and the conjugated antibodies were evaluated using matrix-assisted laser desorption/ionization time of flight mass spectrometry (MALDI-ToF MS) to determine the chelate number for each antibody. Because we decided to use a

Antibody	HuE71-1 MAGE	HuE71-1	HuE71-1 Aglyco	HuE71-4	HuE71-4M	Ctrl-4
Target	L1CAM	L1CAM	L1CAM	L1CAM	L1CAM	GD2 (non-specific)
Subclass	IgG1	IgG1	IgG1	IgG4	IgG4	IgG4
Modification	Defucosylated Fc region	Wildtype	Aglycosylated Fc region	Wildtype	Hinge region mutation	Wildtype
FcγR Binding	++	+	-	-	-	-
Fab Arm Exchange	-	-	-	+	-	+

Figure 3.1. Table of L1CAM targeted humanized antibodies outlining characteristics.

non-specific conjugation method, it is entirely possible for DFO moieties to form multiple thiourea linkages on lysine residues distributed randomly on the antibodies. MALDI-ToF MS analysis of the pre-conjugated and post-conjugated antibodies revealed values of 2.38 chelates per ^{89}Zr-HuE71-1 MAGE, 1.41 chelates per ^{89}Zr-HuE71-1 WT, 1.07 chelates per ^{89}Zr-HuE71-1 Aglyco, 1.30 chelates per ^{89}Zr-HuE71-4 WT, 0.63 chelates per ^{89}Zr-HuE71-4 Mutant, and 1.12 chelates per ^{89}Zr-HuCtrl-4 WT (Figures A.3.1-A.3.7). Needless to say, these values represent average number of chelates per antibody molecule and not absolute values. Of course, it is impossible to have 1.41 DFO molecules attached to ^{89}Zr-HuE71-1 WT so this number indicates that each antibody molecule has 1 or 2 chelators bound. Each of the antibodies was then radiolabeled with ^{89}Zr in PBS for 60 minutes at 37 degrees Celsius.

Radiochemical yields and specific activities were calculated using instant thin layer chromatography (ITLC) with a mobile phase of EDTA (ph 5.0, 50 mM) where the free ^{89}Zr migrates with the solvent front and the chelated ^{89}Zr remains at the baseline. Radiochemical yields for all of the antibodies were greater than 95% and the radiochemical purities for all of the antibodies were greater than 99% following size exclusion chromatography purification (PD-10 column). Specific activities for all of the antibodies (excluding ^{89}Zr-HuE71-4 Mutant) were between 6.18-6.89 μCi/μg post-radiolabeling. Despite many attempts at optimizing the radiolabeling of ^{89}Zr-HuE71-4 Mutant, we were unable to achieve a specific activity above 2.14 μCi/μg. This finding makes sense when considered with the MALDI-ToF MS data which indicates ^{89}Zr-HuE71-4 Mutant has the lowest average chelate number of 0.63. Further investigation could be pursued to evaluate the effect of the S228P mutation on the DFO bioconjugation reaction. Considering the serine has a polar side chain and proline has a non-polar, cyclic side chain, one possible hypothesis is the S228P in the hinge region alters the conformation of the antibody to the extent that fewer lysine residues

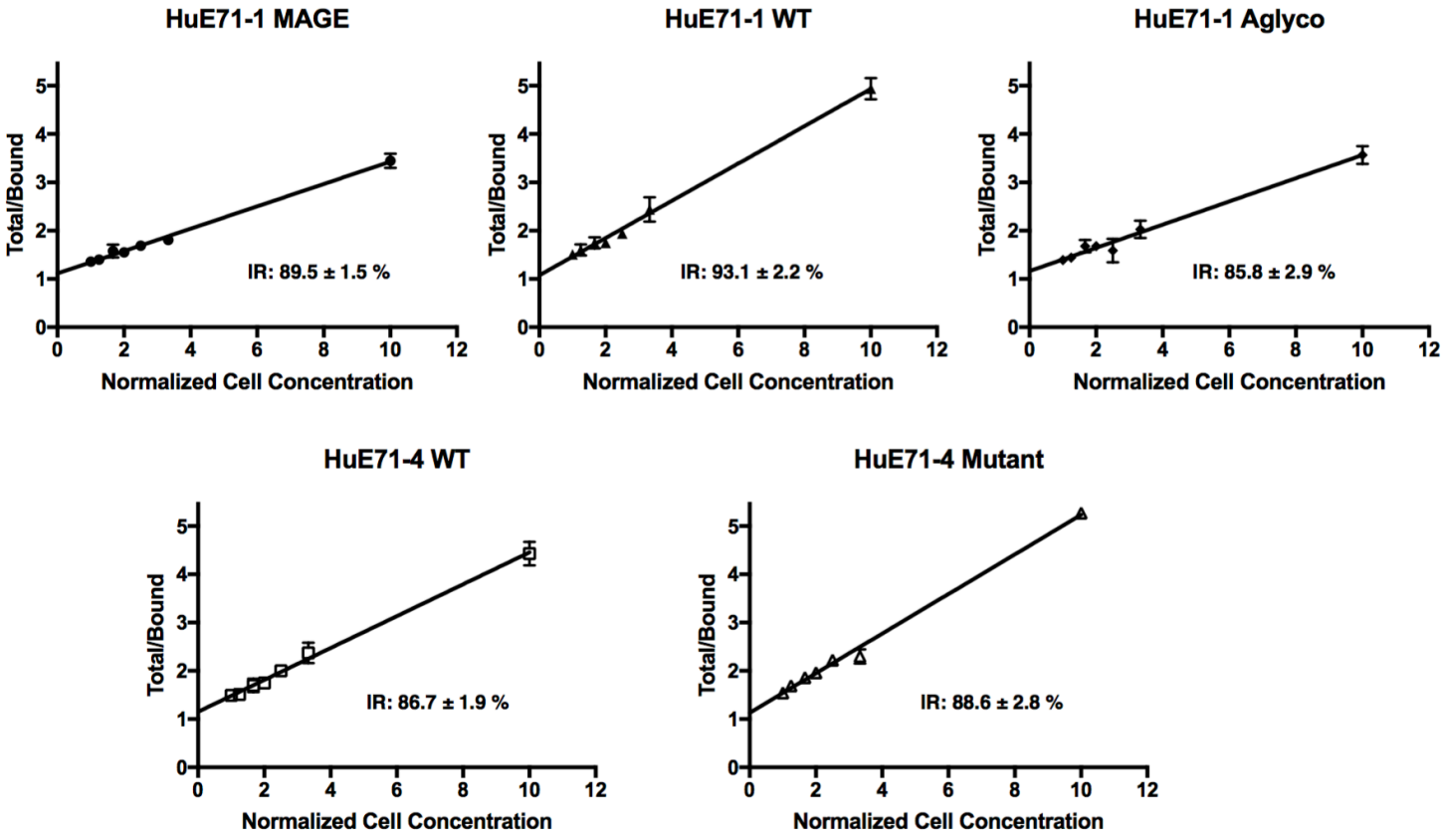

Figure 3.2. Immunoreactivity of ^{89}Zr-radiolabeled L1CAM antibodies
The radioimmunoconjugates were functionally characterized for binding to antigen-expressing cells (SKOV-3) and the determination of the immunoreactive fraction via Lindmo assays [79]. Aliquots of each radioimmunoconjugate, 50 μL of 1 μCi/mL stock were added to tubes containing 5.0 x 10^5 – 5.0 x 10^6 cells/mL (in triplicate) in 500 μL PBS, 1% BSA (pH 7.4 to a final volume of 550 μL). Cell bound activity was counted and data graphed on double-reciprocal plot. Immunoreactive fractions are presented as mean percentages of triplicate samples ± SEM.

are available to react with the functionalized DFO [99].

In Vitro Characterization

In order to assess the radiochemical stability of the tracers, a serum stability challenge was performed. A small aliquot (100 μL) of each radioimmunoconjugate was incubated in human serum (900 μL) at 37 degrees through seven days. Samples were taken on days 0, 1, 3, 5 and 7 and evaluated via radio instant thin layer chromatography to determine the percentage of activity remaining bound to the antibody. The study revealed that all of the tracers were stable throughout seven days with values of 97.3 ± 0.8% for ^{89}Zr-HuE71-1 MAGE, 97.7 ± 0.7% for ^{89}Zr-HuE71-1 WT, 96.6 ± 0.8% for ^{89}Zr-HuE71-1 Aglyco, 96.9 ± 0.3% for ^{89}Zr-HuE71-4 WT, 97.5 ± 0.3% for ^{89}Zr-HuE71-4 Mutant, and 96.7 ± 1.1% for ^{89}Zr-HuCtrl-4 WT (Figure A.3.8). These values, all above 95% intact through seven days are in line with what was expected for a ^{89}Zr-DFO radiolabeled antibody.

To determine the extent to which these antibodies were able to bind the target post-radiolabeling, immunoreactivity assays were performed. Briefly, the ^{89}Zr-labeled antibodies were incubated with increasing concentrations of target positive ovarian cancer cells (SKOV3) and, following washes, the cell bound activity was counted and used to calculate the immunoreactive fraction. These experiments yielded immunoreactivities greater than 85% for all the antibodies, specifically, 89.5 ± 1.5 % for ^{89}Zr-HuE71-1 MAGE, 93.1 ± 2.2 % for ^{89}Zr-HuE71-1 WT, 85.8 ± 2.9 % for ^{89}Zr-HuE71-1 Aglyco, 86.7 ± 1.9 % for ^{89}Zr-HuE71-4 WT and 88.6 ± 2.8 % for ^{89}Zr-HuE71-4 Mutant (Figure 3.2). We were pleased to observe that all of the radioimmunoconjugates had high immunoreactive fractions as it would complicate our analysis of imaging and biodistribution data if there were significant differences between the tracers in terms of antigen binding. With the

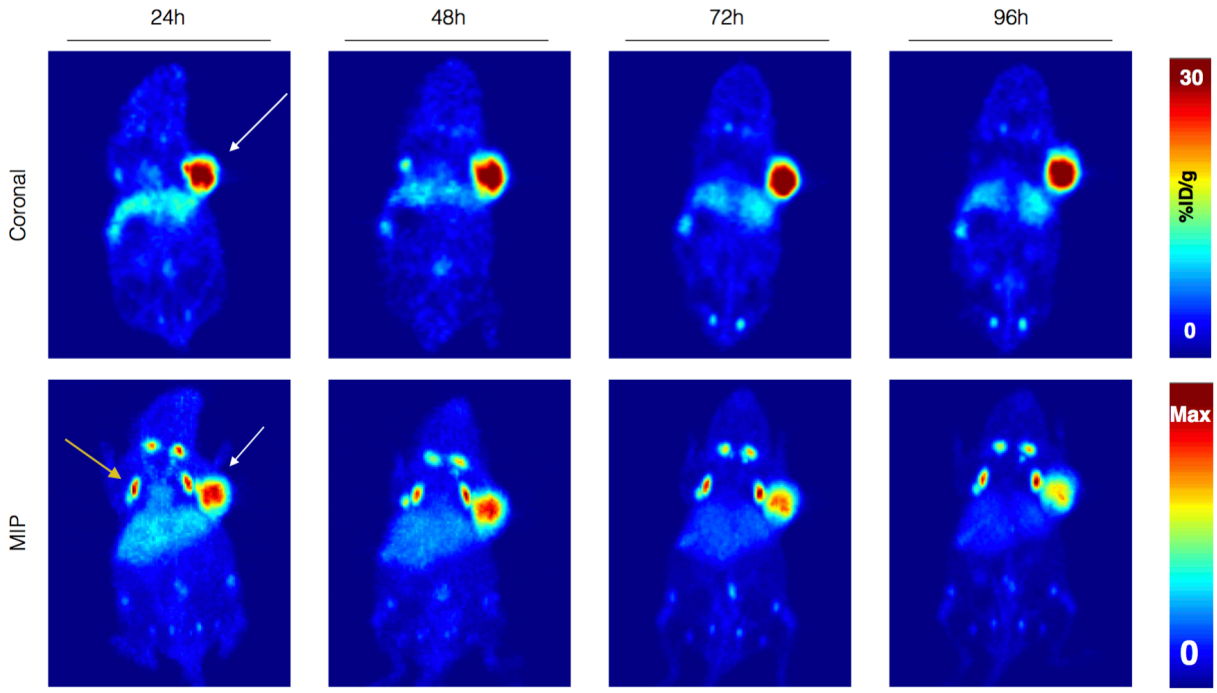

Figure 3.3. Serial PET imaging of ^{89}Zr-HuE71-1 MAGE
Small-animal PET imaging in a subcutaneous ovarian cancer tumor model revealing high tumor and lymph node (yellow arrow) activity concentration. Representative coronal and maximal intensity projection (MIP) PET images of ^{89}Zr-HuE71-1 MAGE (192-197 μCi in 150 μL of PBS injected via tail vein) in athymic nude mice bearing subcutaneous SKOV-3 tumors xenografted on the right shoulder (white arrow). Coronal planar images intersect the middle of the tumor.

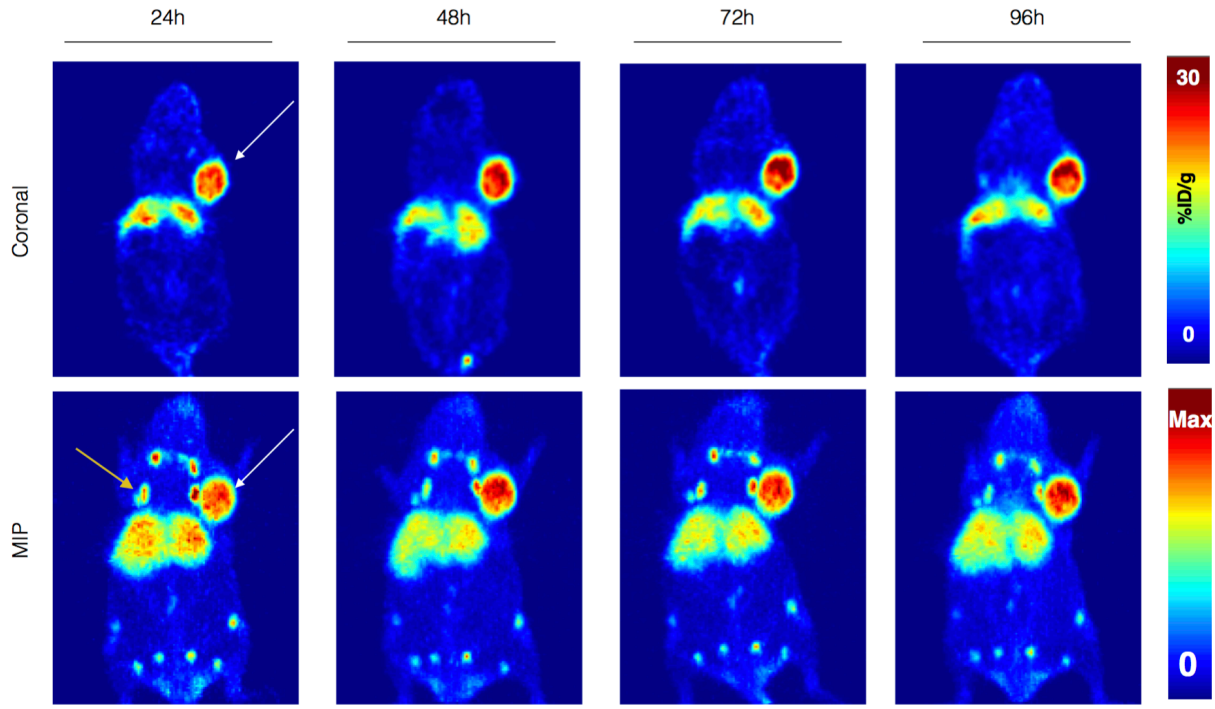

Figure 3.4. Serial PET imaging of ^{89}Zr-HuE71-1 WT
Small-animal PET imaging in a subcutaneous ovarian cancer tumor model revealing high tumor, liver and lymph node (yellow arrow) activity concentration. Representative coronal and maximal intensity projection (MIP) PET images of ^{89}Zr-HuE71-1 WT (194-201 μCi in 150 μL of PBS injected via tail vein) in athymic nude mice bearing subcutaneous SKOV-3 tumors xenografted on the right shoulder (white arrow). Coronal planar images intersect the middle of the tumor.

immunoreactivities of all of the tracers within range of each other, we can make the assumption that any differences that we observe in the pattern of imaging and biodistribution of the radioimmunoconjugates are not due to differences in the binding ability of the to the target antigen (L1CAM).

Serial PET Imaging

To investigate how the modifications to the Fc region of the antibodies would alter the biodistribution pattern of these radioimmunoconjugates, we performed serial PET imaging studies on female nude athymic mice bearing subcutaneous SKOV3 tumors on the right shoulder. The radiolabeled immunoconjugates were injected via the tail vein and PET images were acquired at 4 time points post-injection (24, 48, 72 and 96h). Presented in all of the imaging figures are coronal slices of the mice through the tumor tissue (all scaled from 0 to 30 % injected dose per gram) and maximal intensity projections (MIP) representing the total body image.

For ^{89}Zr-HuE71-1 MAGE (Figure 3.3), we observed at 24 hours post-injection high radioactivity concentration of the tracer in the tumor tissue (white arrow) with minimal radioactivity in the non-targeted organs. The tracer cleared rapidly from the blood pool as no heart or large blood vessels can be seen. Interestingly, four bilateral structures within the upper portion of the animal (yellow arrow) appeared to have high radioactive concentration as well. These PET-positive tissues were harvested and identified them as the submandibular and axillary lymph nodes. Further, the lymph node uptake with ^{89}Zr-HuE71-1 MAGE persisted up to 96 hours post-injection of the radiotracer. PET images of SKOV-3 xenografts injected with ^{89}Zr-HuE71-1 WT revealed high tracer uptake within the tumor tissue at 24 hours which continued to accumulate up to 96 hours (Figure 3.4). There was high liver radioactivity concentration that was quite intense at 24 hours then gradually washes out slightly through 96 hours. Once again, the four lymph nodes in the upper

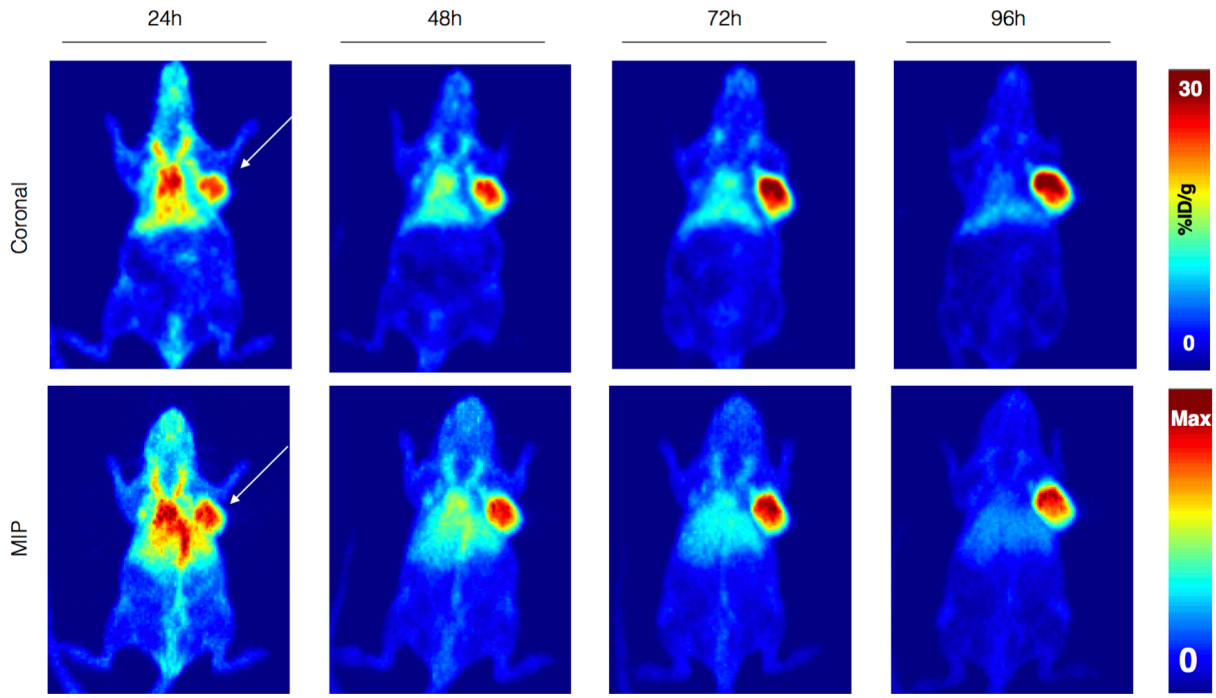

Figure 3.5. Serial PET imaging of ^{89}Zr-HuE71-1 Aglyco
Small-animal PET imaging in a subcutaneous ovarian cancer tumor model revealing high tumor and very low background activity concentration. Representative coronal and maximal intensity projection (MIP) PET images of ^{89}Zr-HuE71-1 Aglyco (207-214 μCi in 150 uL of PBS injected via tail vein) in athymic nude mice bearing subcutaneous SKOV-3 tumors xenografted on the right shoulder (white arrow). Coronal planar images intersect the middle of the tumor.

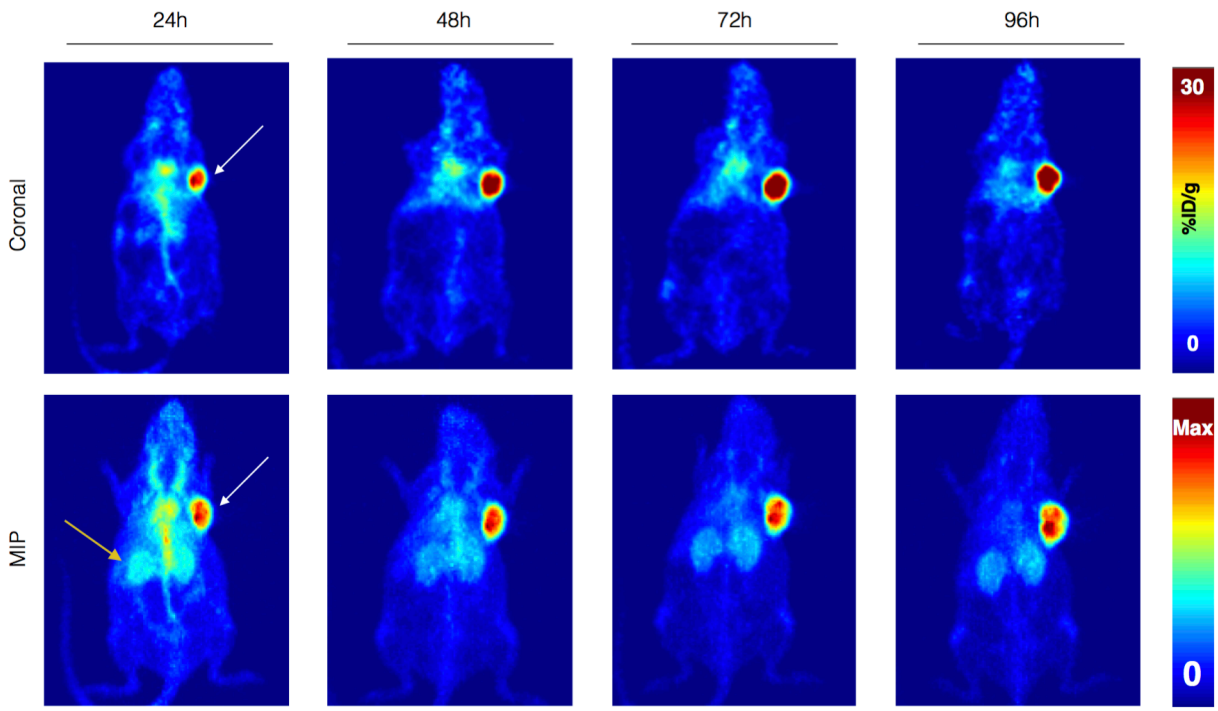

Figure 3.6. Serial PET imaging of ^{89}Zr-HuE71-4 WT
Small-animal PET imaging in a subcutaneous ovarian cancer tumor model revealing high tumor and kidney (yellow arrow) activity concentration. Representative coronal and maximal intensity projection (MIP) PET images of ^{89}Zr-HuE71-4 WT (198-204 μCi in 150 uL of PBS injected via tail vein) in athymic nude mice bearing subcutaneous SKOV-3 tumors xenografted on the right shoulder (white arrow). Coronal planar images intersect the middle of the tumor.

portion of the mouse were illuminated on PET at 24 hours, as well as the lower lymph nodes, but they appeared to fade slightly through 96 hours.

In the ^{89}Zr-HuE71-1 Aglyco (Figure 3.5) images, we observed high radioactivity concentration of the tracer within the tumor tissue at 24 hours which continued to accumulate up to 96 hours. Blood pool activity with this tracer was quite high and clearly visible at 24 hours in the heart, descending aorta, and right and left common carotid arteries but this activity cleared out rapidly by 72 hours post-injection. Based on the PET imaging data, of the IgG1 radiolabeled antibodies, ^{89}Zr-HuE71-1 Aglyco has the cleanest biodistribution profile, in that, by from 24 hours post-injection to 96 hours, the tumor tissue had the highest radioactivity concentration with the least amount of non-targeted tissue activity.

For ^{89}Zr-HuE71-4 WT (Figure 3.6), the majority of the activity was within the tumor tissue at 24 hours and in the maximal intensity projections, blood pool activity acould be visualized quite clearly. Two bilateral structures in the middle of the animal (yellow arrow) could also be seen and these have been confirmed to be kidneys. The high activity within the tumor tissue persisted up to 96 hours post-injection, as well as the kidney activity.

In images of ^{89}Zr-HuE71-4 Mutant (Figure 3.7), we observed slight tumor uptake at 24 hours that continued to gradually accumulate over a period of time up to 96 hours. Once again, there was blood pool activity that, in this case, appeared to decrease throughout 96 hours, but not completely. Most notable, however, is the absence of kidney uptake with ^{89}Zr-HuE71-4 Mutant that was clearly observed with ^{89}Zr-HuE71-4 WT.

The final tracer imaged in this study was a non-specific control antibody, ^{89}Zr-HuCtrl-4 WT (Figure 3.8). At all time points the activity within the tumor tissue was very minimal, consistent with

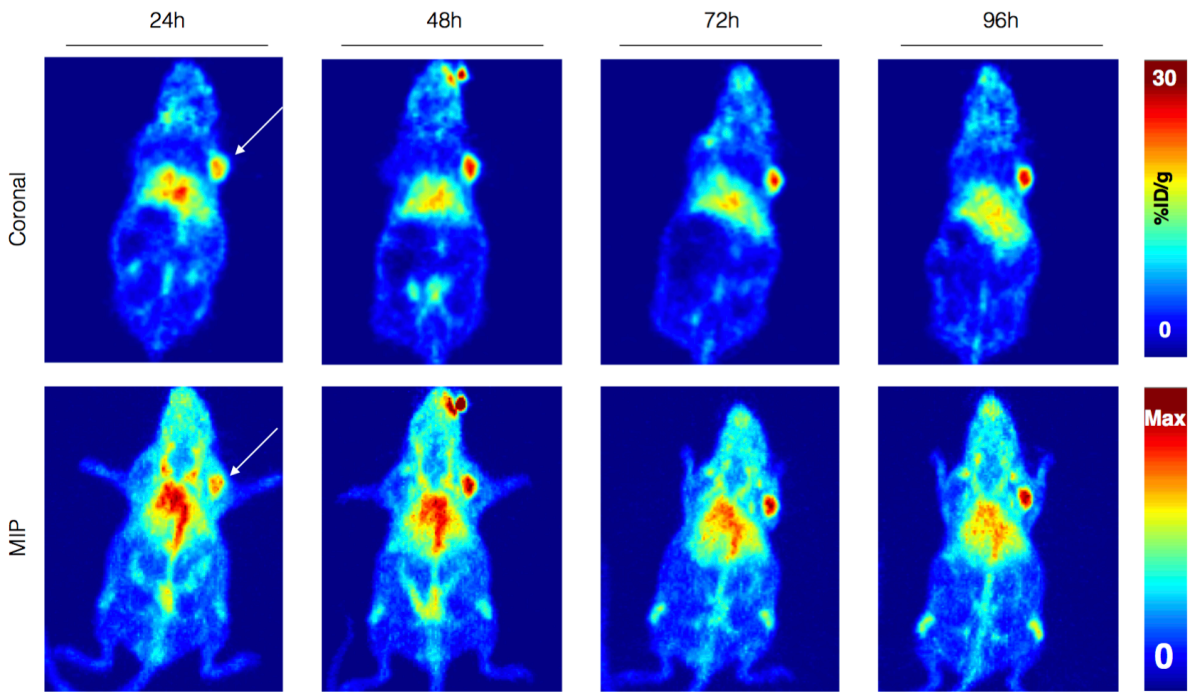

Figure 3.7. Serial PET imaging of ^{89}Zr-HuE71-4 Mutant
Small-animal PET imaging in a subcutaneous ovarian cancer tumor model revealing high tumor and background tissue activity while kidney activity appeared minimal. Representative coronal and maximal intensity projection (MIP) PET images of ^{89}Zr-HuE71-4 Mutant (206-212 μCi in 150 μL of PBS injected via tail vein) in athymic nude mice bearing subcutaneous SKOV-3 tumors xenografted on the right shoulder (white arrow). Coronal planar images intersect the middle of the tumor.

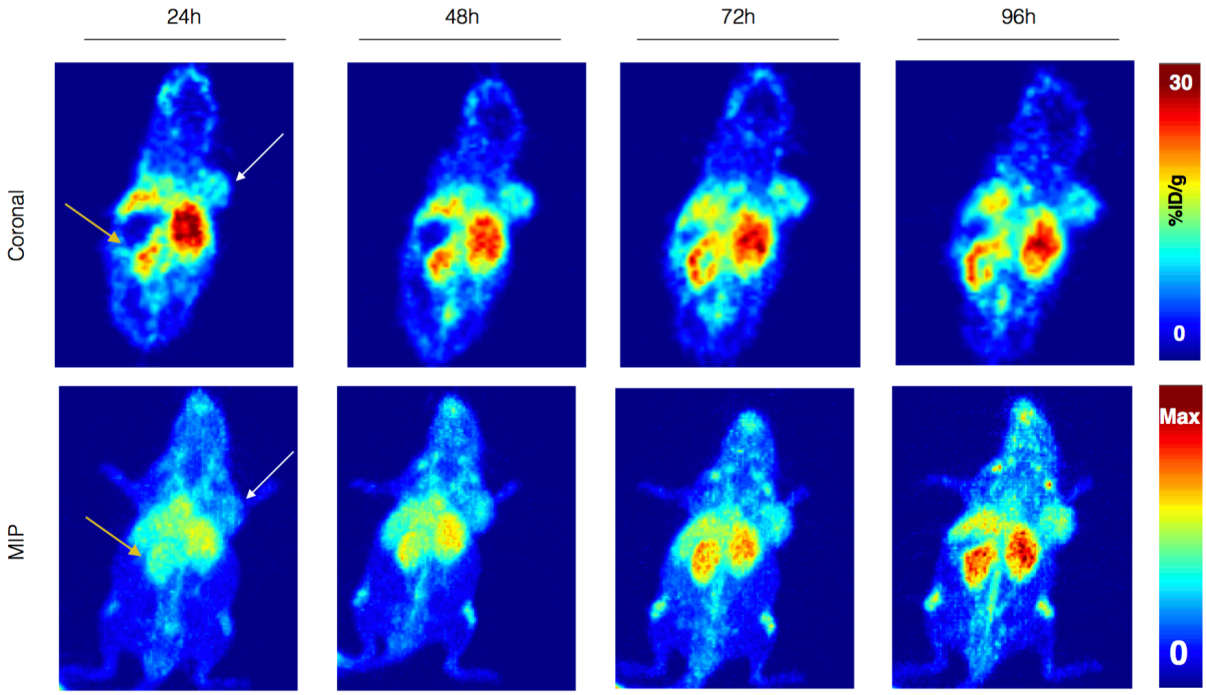

Figure 3.8. Serial PET imaging of ^{89}Zr-HuCtrl-4 WT
Small-animal PET imaging in a subcutaneous ovarian cancer tumor model revealing low tumor but high kidney (yellow arrow) activity. Representative coronal and maximal intensity projection (MIP) PET images of ^{89}Zr-HuCtrl-4 WT (200-211 μCi in 150 μL of PBS injected via tail vein) in athymic nude mice bearing subcutaneous SKOV-3 tumors xenografted on the right shoulder (white arrow). Coronal planar images intersect the middle of the tumor.

the fact that the target of the antibody, GD2, was not highly expressed by the SKOV-3 cell line. Liver activity could be seen through all of the time points as well as intense kidney activity.

The results of this study are both intriguing and informative. To reiterate, besides the control antibody (^{89}Zr-HuCtrl-4 WT), all of the other tracers had the exact same antigen binding site targeting L1CAM. The only differences between the five L1CAM tracers lies within the Fc region and those differences clearly have a large impact on the biodistribution *in vivo*. The antibody variants that are known to have less Fc receptor binding (^{89}Zr-HuE71-1 Aglyco, ^{89}Zr-HuE71-4 WT, ^{89}Zr-HuE71-4 Mutant) all are absent of lymph node uptake according to the PET images. Conversely, the antibodies that are known to have normal or enhanced Fc gamma receptor binding (^{89}Zr-HuE71-1 WT, ^{89}Zr-HuE71-1 MAGE) have intense lymph node uptake on PET imaging. Considering the fact that the antigen binding regions of all of the L1Cam tracers were the same, but the lymph node uptake was differential, we are able to rule out the hypothesis that local expression of the antigen plays a role in lymph node uptake. Further, we measured the binding of the L1CAM radioimmunoconjugates in immunoreactivity assays, which yielded greater than 85% immunoreactive fractions so we are able to rule out differences in antigen binding as a cause for the differential uptake.

Focusing in on the IgG4 tracers, we came across an interesting finding—high kidney uptake in the wildtype variant. Even more interesting is the fact that a simple S228P mutation in this tracer was able to reduce the kidney uptake to the point where it could not be visualized on PET at any time point. IgG4 antibodies, as described earlier, undergo dynamic fab arm exchange and are capable of spontaneously breaking apart at the hinge region (to form a ~75 kDa construct) and then recombine with other half molecules. We hypothesize that the kidney uptake seen in the wild type IgG4 may be secondary to the dynamic fab arm exchange property because the S228P mutation

prevents this renal accumulation from occurring, as seen on PET. We believe that the 75 kDa half antibody undergoes further reduction into 25 and 50 kDa fragments allowing them to pass through the glomeruli within the kidneys. In support of this finding, the non-specific ^{89}Zr-HuCtrl-4 WT antibody, an IgG4, exhibits high accumulation within the renal tissue as well, strengthening this IgG4-renal uptake hypothesis. These observations most certainly warrant further investigation.

Ex Vivo Biodistribution

To confirm the PET imaging results and to verify specificity of the tracers, *ex vivo* biodistribution studies were performed (Figure 3.9, 3.10, A.3.9, A.3.10). The radiolabeled immunoconjugates were injected via tail vein into female athymic nude mice bearing SKOV3 tumors and various tissues were collected at 96 hours post-injection, analyzed on a gamma counted, and weight normalized. The results of these studies matched the trends that were revealed by the PET imaging experiments with the antibodies that are known to have normal or enhanced Fc gamma receptor binding (^{89}Zr-HuE71-1 WT, ^{89}Zr-HuE71-1 MAGE) having high lymph node uptake (16.85 ± 1.39 %ID/gram, 17.16 ± 0.41 %ID/gram). Conversely, the aglycosylated variant of the antibody, ^{89}Zr-HuE71-1 Aglyco, demonstrated a basal level of lymph node uptake of 5.59 ± 0.49 %ID/gram.

These values obtained via *ex* vivo biodistribution correlate well with the imaging data and further corroborate the hypothesis that increased lymph node uptake is due to binding of the Fc region of the antibody as opposed to the variable region. For the IgG4 antibodies, ^{89}Zr-HuE71-4 WT displayed lymph node uptake of 3.98 ± 0.969 %ID/gram while ^{89}Zr-HuE71-4 Mutant was 3.70 ± 0.975 %ID/gram. No significant difference was seen with these two antibodies within the lymph nodes, but for the kidneys, that is not the case. ^{89}Zr-HuE71-4 WT accumulated in the kidneys with a value of 12.06 ± 1.23 %ID/gram while ^{89}Zr-HuE71-4 Mutant was significantly lower at 5.83 ± 0.537 %ID/gram. These data recapitulate what was observed in the PET imaging data and further imply

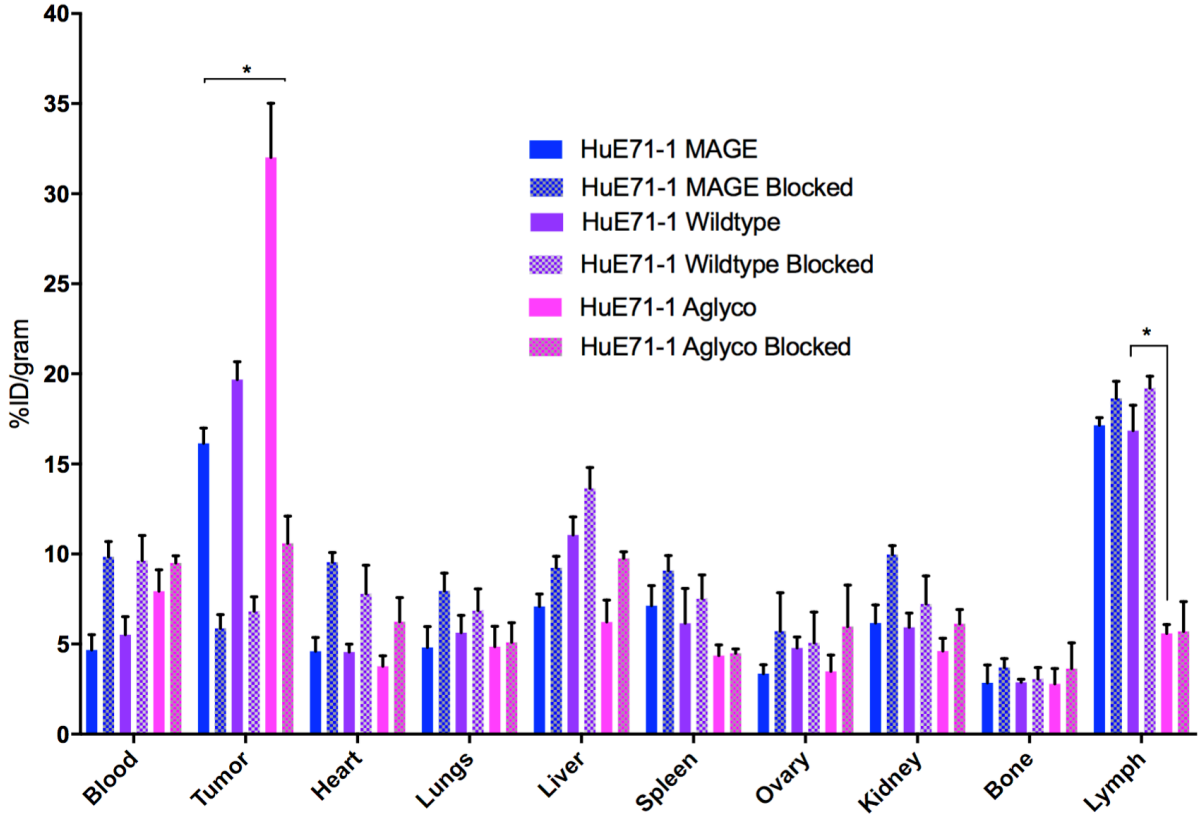

Figure 3.9 *Ex vivo* biodistribution of IgG1 antibodies 96h post-injection of tracer.
Acute biodistribution of radioimmunoconjugates in SKOV-3 tumor-bearing mice. Biodistribution data from athymic nude mice (n = 4 per group) following the administration of IgG1 radioimmunoconjugates via tail vein injection (17-24 μCi, 3–6 μg). A 50-fold excess was co-injected for the blocking groups. %ID/g values listed in Figure A.3.9. Asterisk indicates $P < 0.05$.

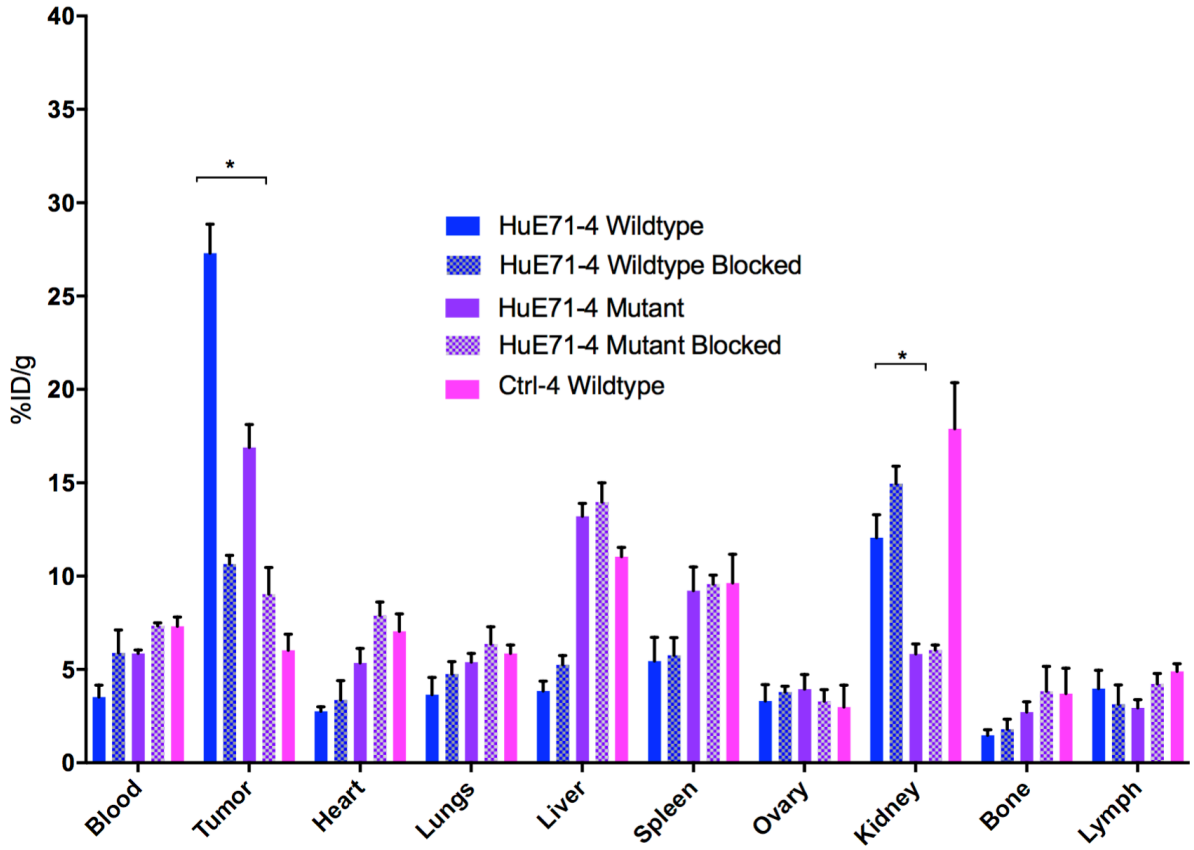

Figure 3.10 *Ex vivo* biodistribution of IgG4 antibodies 96h post-injection of tracer.
Acute biodistribution of radioimmunoconjugates in SKOV-3 tumor-bearing mice. Biodistribution data from athymic nude mice (n = 4 per group) following the administration of IgG4 radioimmunoconjugates via tail vein injection (21-26 μCi, 3–6 μg). A 50-fold excess was co-injected for the blocking groups. %ID/g values listed in Figure A.3.10. Asterisk indicates $P < 0.05$.

that the IgG4 property of dynamic fab arm exchange plays a role in the renal uptake of the tracers.

To evaluate the specificity of these tracers for the target, blocking groups were included in the *ex vivo* biodistribution studies. Fifty-fold excess of the cold tracer was co-injected with the radiolabeled tracer via the tail vein. In principle, the addition of the cold tracer would dramatically reduce the specific activity of the hot tracer and if specific, a significant decrease in uptake of the hot tracer would be appreciated. This is, in fact, what was observed for all five of the L1CAM targeted antibodies. Tumor tissue uptake values were reduced from 16.15 ± 0.85 %ID/gram to 5.87 ± 0.76 %ID/gram for ^{89}Zr-HuE71-1 MAGE, 19.67 ± 1.23 %ID/gram to 6.82 ± 0.809 %ID/gram for ^{89}Zr-HuE71-1 WT, 32.02 ± 2.99 %ID/gram to 10.58 ± 1.52 %ID/gram for ^{89}Zr-HuE71-1 Aglyco, 27.29 ± 1.55 %ID/gram to 10.65 ± 0.472 %ID/gram for ^{89}Zr-HuE71-4 WT, and 16.90 ± 1.21 %ID/gram to 9.04 ± 1.42 %ID/gram for ^{89}Zr-HuE71-4 Mutant. For ^{89}Zr-HuCtrl-4 WT, a non-specific antibody in this model, the tumor uptake was quite low at 6.02 ± 0.90 % ID/gram. This uptake in the tumor tissue can be attributed to the enhanced permeability and retention (EPR) effect [(100)].

Ex Vivo Histology

In order to determine whether the lymph node uptake that was seen in the PET imaging studies with the IgG1 tracers actually indicated metastatic disease, the lymph nodes and tumors were collected and analyzed histologically by the Laboratory of Comparative Pathology (Figure 3.11). Hematoxylin and eosin staining of the tumor tissue confirmed the mass to be anaplastic carcinoma. The tumor tissue is described as well demarcated, unencapsulated, densely cellular nodular neoplastic mass which consists of tightly packed lobules and nests of neoplastic epithelial cells supported by fine fibrovascular septa. Neoplastic cells are polygonal to spindloid, have variably distinct cell borders, abundant amounts of eosinophilic cytoplasm occasionally vacuolated, and

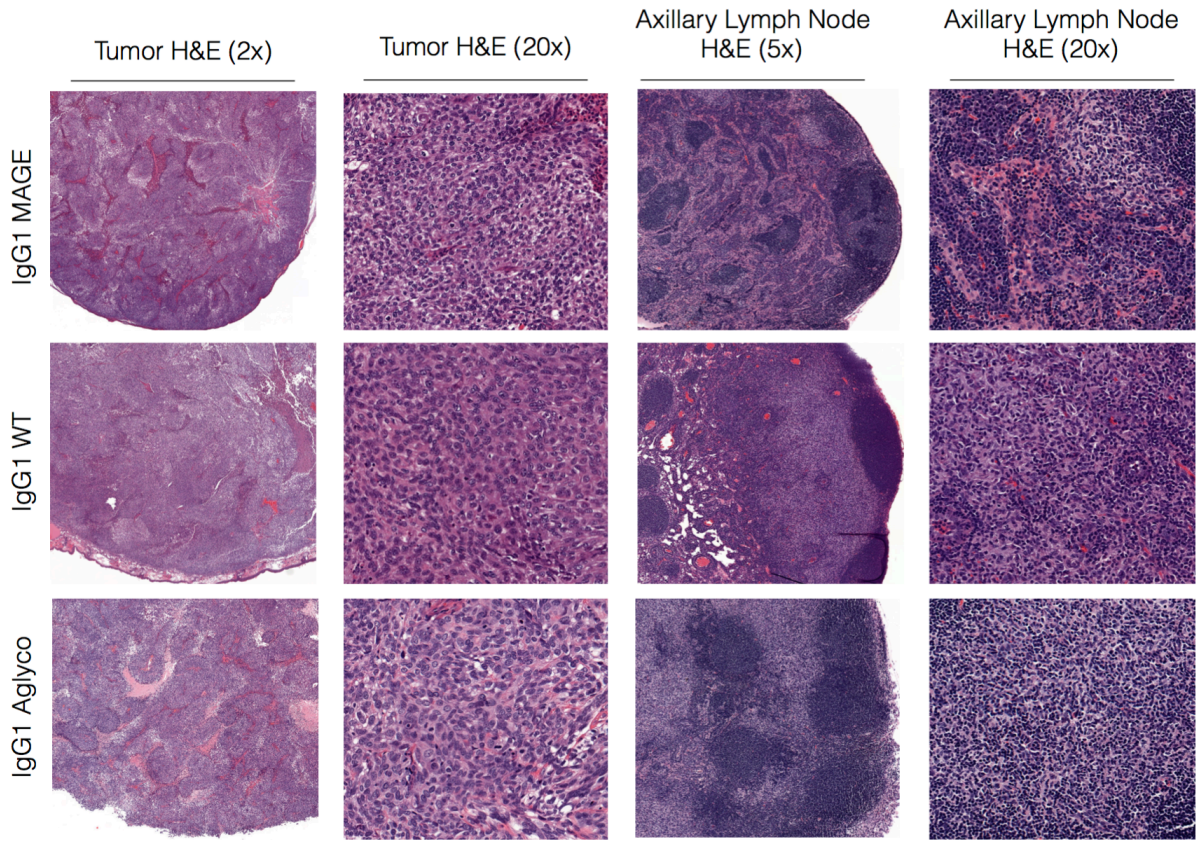

Figure 3.11. *Ex* vivo histological analysis of tumor and lymph node tissue.
Tumor and lymph node tissue of mice injected with specified radioimmunoconjugate were collected, embedded in parafin and subjected to routine H&E staining and analysis.

round nuclei with finely granular to vesicular chromatin and 1-2 evident magenta nucleoli. There is severe anisocytosis and anisokaryosis. Mitoses average 4-6 per single high power field (40x). There are multifocal areas of coagulative necrosis. Hematoxylin and eosin staining of the right and left axillary lymph nodes and mesenteric lymph nodes revealed histiocytosis and plasmacytosis, a common manifestation of drainage reaction, within the medullary sinuses and most importantly, no evidence of neoplastic cells.

^{177}Lu Radioimmunotherapy Study

From the previous imaging and *ex vivo* biodistribution studies, it is clear that ^{89}Zr-HuE71-1 Aglyco is the best candidate for a radioimmunotherapy application because of its high tumor activity concentration of 32.02 ± 2.99 %ID/gram at 96 hours post-injection along with its low background tissue uptake (especially kidneys and blood). We chose to label the antibody with the metallic radionuclide ^{177}Lu because of its radiochemical properties (half-life, 6.7 days; mean range, 0.2 mm; %ß = 100) and widespread use to label antibodies and peptides for imaging and radioimmunotherapy studies in animals and humans [101-103]. The HuE71-1 Aglyco antibody was conjugated to DOTA, labeled with ^{177}Lu to a specific activity of 3.94 mCi/mg (radiochemical purity > 99%) and subjected to imaging studies and an *ex vivo* biodistribution study in athymic nude female mice bearing SKOV-3 subcutaneous tumors (Figure A.3.11). The studies confirmed a similar biodistribution profile as observed with the ^{89}Zr-HuE71-1 Aglyco with the majority of the activity localizing to the tumor tissue as seen in the SPECT/CT image and Cerenkov image, and confirmed by *ex vivo* biodistribution 168 hours post-injection.

With these promising data in hand, we evaluated the efficacy of the novel ^{177}Lu-HuE71-1 Aglyco as a radioimmunotherapeutic agent at 3 doses (800 μCi, 800 μCi fractionated [2 doses, staggered 14 days], and 400 μCi) and compared with the cold antibody, 800 μCi non-specific

antibody control, and saline in the same animal model (n=8-9 per group) (Figure 3.12). Following the average tumor volume through 80 days (60 days post initial treatment), significant differential responses were observed between the control groups and the radiolabeled treatment groups. Notably, none of the groups displayed signs of tumor regression beyond the starting volume. The three ^{177}Lu-HuE71-1 Aglyco groups showed significant growth-delay effects through 80 days post-inoculation. Interestingly however, there was no significant difference within the ^{177}Lu-HuE71-1 Aglyco groups in terms of tumor volume during the later time points of the study with the average tumor volumes for these groups being equivalent within error on Day 80. In addition, signs of toxicity (weight loss > 80% and petechiae) were observed in 4/8 of the mice in the highest treatment group (800 μCi, ^{177}Lu-HuE71-1 Aglyco) within the first 2 weeks following treatment. More interestingly, this was not observed in any of the mice injected with 800 μCi of the non-specific control antibody. This observation is most likely due to the difference in clearance/elimination of the tracers. Further investigation into this possibility is necessary to confirm. These data together suggest that a single dose of 400 μCi ^{177}Lu-HuE71-1 Aglyco is sufficient to delay tumor growth in this model while avoiding toxicity issues.

Conclusions

In this study, we have been able to show that molecular imaging techniques can be useful tools for the study and design of antibodies for use in imaging applications and beyond. More specifically, we have been able to visualize at the whole organism level, how deliberate Fc engineering strategies can impact the biodistribution of antibodies *in vivo*.

By developing a panel of antibodies that were identical in terms of the antigen binding region, and only modifying the Fc region, we have been able to answer our question regarding high

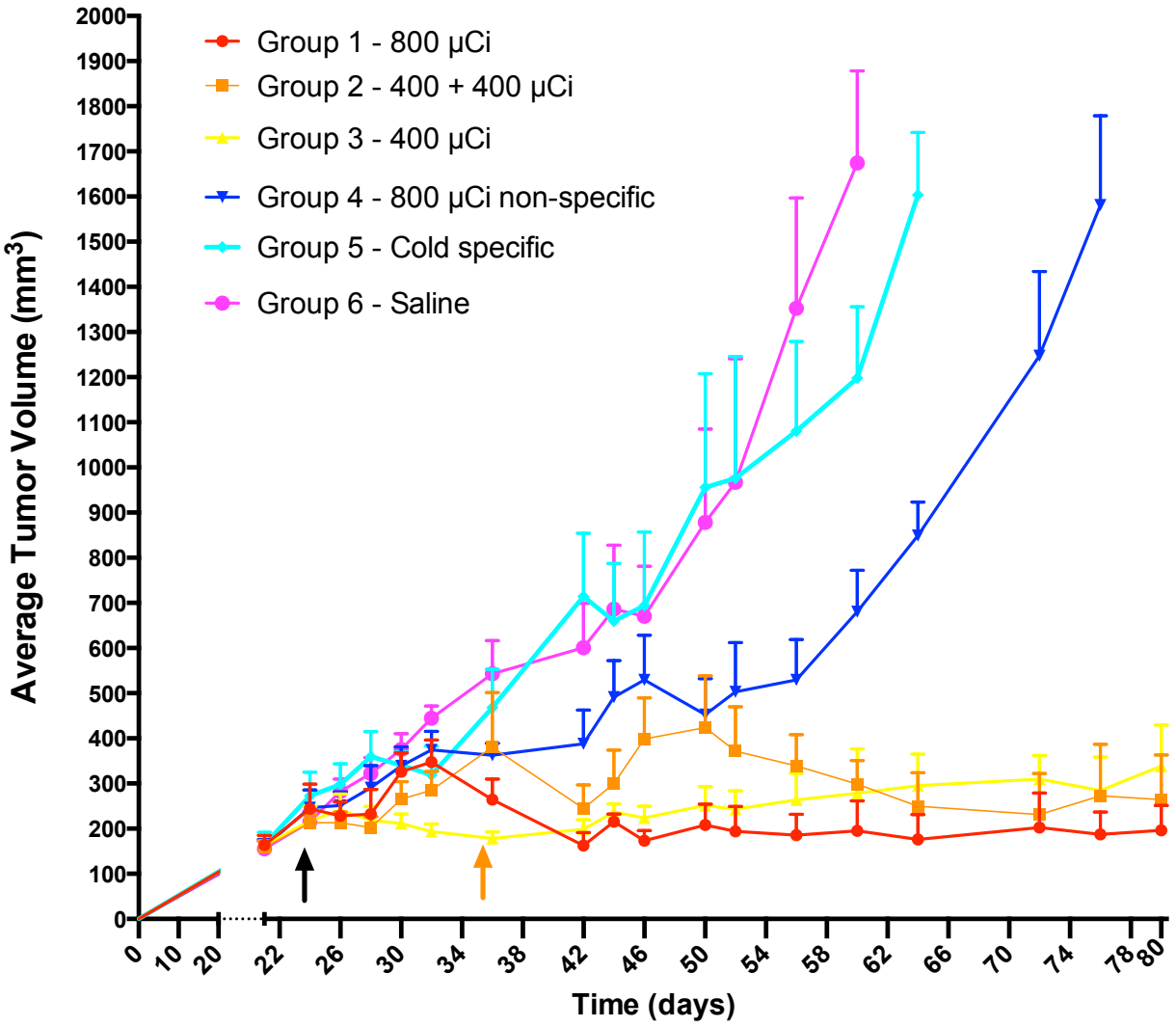

Figure 3.12. ^{177}Lu-HuE71-1 Aglyco radioimmunotherapy average tumor volumes.
Plot of the average tumor volume for each cohort of mice during the first 80 days of the PRIT study are shown with error bars denoting standard deviation. Black arrow indicates first injection of the specified treatment and orange arrow indicates second dose of ^{177}Lu-HuE71-1 Aglyco in the fractionated dose group. Tumor volumes were acquired using hand-held TM900 scanner (Peira, Brussels, BE). After initial tumor measurements, mice were randomized into groups (n = 8-9 per group), ensuring all cohorts had approximately equal average tumor volumes to start.

lymph node uptake of radiolabeled antibodies in the absence of metastatic nodes. We originally hypothesized that this occurrence could be due to either local expression of the antigen or binding of the Fc region of the antibodies to the Fc gamma receptors expressed on the immune cells within the lymph nodes.

Since the normal and enhanced Fc gamma receptor binding antibodies (^{89}Zr-HuE71-1 MAGE and ^{89}Zr-HuE71-1 WT) exhibited statistically significantly higher lymph node uptake as compared to the low Fc gamma receptor binding antibodies (^{89}Zr-HuE71-1 Aglyco, ^{89}Zr-HuE71-4 WT, ^{89}Zr-HuE71-4 Mutant), we can conclude that the high lymph node uptake observed is due to Fc binding, and not local expression of L1CAM.

Furthermore, in terms of the IgG4 antibodies, we have shown a statistically significant difference in the high renal uptake of ^{89}Zr-HuE71-4 WT and the low renal uptake of ^{89}Zr-HuE71-4 Mutant (S228P mutation) allowing us to conclude that dynamic fab arm exchange (present in ^{89}Zr-HuE71-4 WT, absent in ^{89}Zr-HuE71-4 Mutant) plays a role in the renal accumulation of IgG4 antibodies. This paradigm is supported by the observation of ^{89}Zr-HuCtrl-4 WT also had high renal accumulation throughout 96 hours post injection implying that this phenomenon may be IgG4 antibodies in general.

More broadly, this study illuminates the fact that molecular imaging is not only for diagnosing patients with suspected pathology or for monitoring disease. We can also use it as a tool to explore underlying biology and to enable us to develop and engineer more specific, more targeted, and thus, more effective constructs for a variety of biomedical applications.

Materials and Methods

General Laboratory Procedures

Unless otherwise noted, all chemicals were acquired from Sigma-Aldrich (St. Louis, MO) and used as received and all instruments were calibrated and maintained in accordance with standard procedures. ^{89}Zr was produced at Memorial Sloan Kettering Cancer Center on a TR19/9 cyclotron (Ebco Industries Inc.) via the ^{89}Y(*p,n*)^{89}Zr reaction and purified to yield ^{89}Zr with a specific activity of 196–496 MBq/mg. Activity measurements were made using a CRC-15R Dose Calibrator (Capintec). For the quantification of activities, samples were counted on an Automatic Wizard gamma counter (Perkin Elmer). The radiolabeling of ligands was monitored using instant thin-layer chromatography paper (Agilent Technologies) and analyzed on a Bioscan AR-2000 radio-ITLC plate reader using Winscan Radio-TLC software (Bioscan Inc., Washington, DC). All *in vivo* experiments were performed according to protocols approved by the Memorial Sloan Kettering Institutional Animal Care and Use Committee (Protocol 08 07 013).

Cell Culture

T-75 flasks (Corning, Corning NY) containing cells were stored in cell incubators maintained at 37 °C and a 5% CO_2 concentration. SKOV3, a human epithelial ovarian carcinoma cell line (ATCC, Manassas, VA) was cultured in RPMI McCoy's 5A Medium, modified to contain 1.5 mM L-glutamine, were all grown with 100 units/mL penicillin G and 100 g/mL streptomycin and 10% fetal bovine serum. The SKOV3 cell line was subcultivated once per week using 0.25% trypsin/0.53 mM EDTA in Hank's Buffered Salt Solution without calcium and magnesium and passaged 1:5 for standard cell line passaging.

Xenograft Mouse Models

Eight to ten week old athymic nu/nu female mice were purchased from Charles River Laboratories (Kingston, NY). Animals were housed in ventilated cages, were given food and water ad libitum, and were allowed to acclimatize for approximately 1 week prior to inoculation. SKOV-3 tumors were induced on the right shoulder by a subcutaneous injection of 5.0×10^6 cells in a 150 μL cell suspension of a 1:1 mixture of fresh media/BD Matrigel (BD Biosciences, Bedford, Ma). Experiments were performed approximately 2-3 weeks following the injection of the cancer cells. For tumor volume measurements, all tumors measured using hand-held TM900 scanner (Peira, Brussels, BE). After initial tumor measurements, mice were randomized into groups (n = 8–9 per group), ensuring all cohort had approximately equal average tumor volumes to start.

Antibody Bioconjugation

Antibodies were obtained in citrate buffer (25 mM sodium citrate, 150 mM sodium chloride) at an average concentration of 4-5 mg/mL. The antibodies were concentrated using centrifugal filter units with a 50,000 molecular weight cutoff (Amicon Ultra 4 Centrifugal Filtration Units, Millipore Corp., Billerica, MA) to a final concentration of 12-15 mg/mL. After concentrating, the antibodies were pH adjusted to 8.5-9.0 with 0.1 M Na_2CO_3 before the addition of 10 equivalents of *p*-SCN-Bn-DFO or *p*-SCN-Bn-DOTA (Macrocyclics, Inc. Dallas, TX) dissolved in DMSO. The reaction was incubated at 37 degrees Celsius for 1 h constantly shaking at 500 rpm. The antibodies were purified using centrifugal filter units with a 50,000 molecular weight cutoff (Amicon Ultra 4 Centrifugal Filtration Units, Millipore Corp., Billerica, MA) to purify the ligand-antibody conjugate. The final bioconjugates were aliquoted and stored in PBS pH 7.4 at -80 degrees Celsius.

Radiolabeling

^{89}Zr was received after target processing as ^{89}Zr-oxalate in 1.0 M oxalic acid. The solution was neutralized with 1.0 M sodium carbonate to reach pH ~7. DFO-antibodies were incubated together with neutralized ^{89}Zr labeled in PBS pH 7.4 at 37 degrees Celsius for 60 minutes. $^{177}LuCl_3$ was obtained (specific activity: 170 MBq/mg, Perkin Elmer) and diluted in ammonia acetate buffer (200 mmol/L, pH 5.4) and incubated with DOTA-antibodies at 42 degrees Celsius for 1 hour. The progress of the reactions was monitored via radio-ITLC with silica-gel impregnated glass-microfiber paper strips (ITLC-SG, Varian, Lake Forest, CA) (analyzed by AR-2000, Bioscan Inc., Washington, DC). using 50 mM EDTA at pH 5 as the mobile phase. Antibody complexes remained at the origin, while free radionuclide was taken up by EDTA in the mobile phase and migrated along solvent front. Crude radiochemical yields were calculated using the radio-ITLC data. Radiolabeled antibodies were then purified using size-exclusion chromatography (PD10), followed by centrifugal filtration to concentrate the final volume for formulation. The radiochemical purity of the final purified radiolabeled antibodies was confirmed to be >99% by radio-ITLC before use.

Serum Stability

Aliquots of each ^{89}Zr-antibody complex (100 μL) were incubated with 900 μL of human serum and agitated constantly on a thermomixer at 37 degrees Celsius. Samples were taken from each microcentrifuge tube and analyzed using radio-ITLC at day 0, 1, 3, 5, and 7 in triplicate. The stability of the complexes was measured as the percentage of ^{89}Zr that was retained at the origin of the radio-ITLC strip and reported as % intact.

Immunoreactivity

The immunoreactive fraction of the ^{89}Zr-DFO-antibodies was determined using a cell binding assay following procedures derived from Lindmo *et al* [79].To this end, SKOV3 cells were suspended in microcentrifuge tubes at concentrations ranging from 5.0 x 10^5 – 5.0 x 10^6 cells/mL in 500 μL PBS, 1% BSA (pH 7.4). Aliquots of ^{89}Zr-DFO-antibody (50 μL of 1 μCi/mL stock were added to each tube to a final volume of 500 □ L. The samples were incubated on a thermomixer for 60 min at 37 degrees Celsius. The treated cells were then pelleted via centrifugation (1400 RPM for 4 min), aspirated supernatant, and washed three times with cold PBS before removing the supernatant and counting the cell-associated radioactivity. The activity data were background-corrected and compared with the total number of counts in appropriate control samples. Immunoreactive fractions were determined by linear regression analysis of a plot of (total/bound) activity against (1/[normalized cell concentration]).

PET Imaging

PET imaging experiments were conducted on an Inveon PET/CT scanner (Siemens Healthcare Global). Female, athymic nude mice with SKOV3 xenografts on their right shoulders were administered ^{89}Zr-antibody (192-214 μCi] in 150 μL of PBS) via intravenous tail vein injection. Animals were anesthetized by inhalation of 2% isoflurane (Baxter Healthcare, Deerfield, IL) and medical air gas mixture and placed within the scanner with anesthesia maintained using 2% isoflurane and medical air gas mixture. PET data for each mouse were recorded via static scans at 24, 48, 72, and 96 hours post-injection. An energy window of 350-700 keV and a coincidence timing window of 6 ns were used. Data were sorted into 2D histograms by Fourier rebinning, and transverse images were reconstructed by filtered back-projection (FBP) into a 128 × 128 × 63 (0.72 × 0.72 × 1.3 mm^3) matrix. The counting rates in the reconstructed images were converted to activity concentrations (percentage injected dose per gram of tissue, %ID/g) by use of a system calibration

factor derived from the imaging of a mouse-sized water-equivalent phantom containing ^{89}Zr. Images were analyzed using ASIPro VM software (Concorde Microsystems).

Biodistribution

Biodistribution studies were performed using the ^{89}Zr-antibodies SKOV3 tumor-bearing female, athymic nude mice. Animals were administered (17-26 μCi) of each of the ^{89}Zr-antibodies in 150 μL PBS) via intravenous tail vein injection. Animals (n = 4 per group) were euthanized by CO_2 asphyxiation at 96 hours post-injection. Following euthanasia, 17 organs (blood, tumor, heart, lungs, liver, spleen, stomach, large bowel, small bowel, pancreas, ovary, kidney, bone, muscle, lymph, skin, tail) were collected, weighed, and assayed for radioactivity on a gamma counter calibrated for ^{89}Zr. Counts were converted into activity using a calibration curve generated from known standards. Count data were background and decay corrected to the time of injection, and the percent injected dose per gram (%ID/g) for each tissue sample was calculated by normalization to the total activity injected. The data depicted in this study are expressed as averages ± standard deviation. Statistical differences were analyzed by unpaired, two-tailed, student's t-test using GraphPad Prism 7 software. P-values <0.05 were considered statistically significant and indicated by an asterisk.

CHAPTER 4: MUC16 Targeted Chimeric Antigen T-Cell Tracking Using Zirconium-89 Labeling Approach

This chapter includes an attempted project that requires further work beyond the scope of this dissertation.

Introduction

Chimeric Antigen Receptor T Cells

Chimeric antigen receptors (CAR) are recombinant receptors that are used to genetically engineer T lymphocytes, as well as other immune cells. They contain a extracellular antigen recognition domain, a transmembrane domain and an intracellular T cell activation domain (in addition to a co-stimulatory domain in the case of second-generation CARs) [(104)]. Modification of T cells with a CAR alters the specificity and activity of T cells, targeting them to the receptor antigen. These modified T cells, originally retrieved from the blood of patients, are re-injected for a variety of therapeutic purposes [(105)]. CAR T cells have seen the most success in treating hematologic cancers, most notably in B-cell acute lymphoblastic leukemia [(106-108)]. While CAR T cell therapy against hematologic cancers has shown great promise, clinical trials in solid tumors have been much less successful in terms of antitumor efficacy.

Armored CAR T Cells

One of the hurdles that needs to be overcome in terms of solid tumor CAR T cell therapy is effective trafficking of the T cells to, and within the tumor tissue. Another hurdle in the context of solid tumors is the immunosuppressive environment established by tumors. A strategy to overcome this issue is to genetically modify T cells to express other molecules such as cytokines, in a sense 'armoring' the T cells [(109)]. One such cytokine is interleukin 12 (IL-12) which is a pro-inflammatory

cytokine normally secreted by dendritic cells, macrophages, and neutrophils. Its role in terms of CAR T cells is to activate and enhance the cytotoxic activity and improve T cell persistence.

Koneru M *et al.* developed an IL-12 secreting CAR T cell targeting MUC16 for the treatment of ovarian cancer [110]. They produced four distinct CAR T cells: 1928 (non-specific control), 1928 IL-12 (armored), 4H11 (MUC16 targeted), and 4H11 (MUC16, armored) (Figure 4.1). They were able to show *in vivo* that treating with these modified T cells either delayed progression of orthotopic ovarian cancer or completely eradicated it. Further, they showed that this delay in progression, and survival advantage was significantly greater than with the MUC16-targeted CAR T cells that do not secrete IL-12. **The working hypothesis for this observation is that the IL-12 reprograms the tissue microenvironment such that the CAR T cells are able to persist longer within the tumor. The goal of this project is to validate that hypothesis by using molecular imaging techniques to visualize the location of the CAR T cells *in vivo*.**

Cell Tracking

In the current era of cell-based therapies, *in vivo* cell tracking plays a vital role for the development and monitoring of such applications. Therapies from dendritic cell vaccines to the transfer of genetically modified T cells have become exceedingly prevalent in the last decade [111-113]. In order to optimize therapeutic efficacy, the cells of interest must localize preferentially and specifically to the targets *in vivo*. At present, the strategies for monitoring localization of cell-based therapies are invasive (such as biopsies) and time-consuming and as such, more robust and streamlined approaches are required. For example, bioluminescence imaging has been used with luciferase- expressing cells, but this strategy is limited due to low light penetration at a whole-body level [114]. In addition, the immunogenicity of luciferase would limit its use in man [115]. Attempts at

CAR-T Cells	Characteristics
1928	non-specific
1928 IL-12	armored, non-specific
4H11	specific
4H11 IL-12	armored, specific

Figure 4.1. Table of CAR T cells.
Table outlining the characteristics of each type of chimeric antigen receptor T cell in the following PET imaging experiments.

using magnetic resonance imaging with cells containing iron-nanoparticles has also shown limited success due to poor contrast [116].

Specifically regarding the tracking of radiolabeled cells, much work has been done since the advent of blood cell labeling in the 1970s where autologous leukocytes were isolated, labeled with ^{111}In and injected into patients with suspected inflammatory disorders [117]. Because of several drawbacks of using ^{111}In, much work has been done to develop strategies using longer-lived isotopes to produce high resolution images of cell-based therapies. In the context of the current study, the ^{89}Zr-oxine complex cell labeling technique has been exploited [118]. Here, we describe CAR T cell labeling and imaging studies in the context of ovarian cancer to better understand the role of IL-12 in CAR T cell immunotherapy.

Results and Discussion

Optimization of ^{89}Zr-Oxine Synthesis and CAR T Cell Labeling

The synthesis of ^{89}Zr-oxine was carried out by mixing an oxine-chloroform solution with neutralized ^{89}Zr, constantly agitating for 15 mins at room temperature. The chloroform phase was extracted, solvent removed by evaporation and the product ^{89}Zr-oxine redissolved in DMSO. Following the published protocol exactly however, resulted in a yield of 1.87%. In order to optimize this reaction, several conditions were modified including duration, oxine concentration and pH (Figure 4.2). By increasing the duration of the reaction to 1 hour from 15 mins, we were able to increase the yield to 3.12%. Increasing the concentration of oxine from 1 mg/mL to 5 mg/mL increased the yield to 81.25%. Despite the high yield, the increased concentration caused precipitation to occur in the final DMSO dissolution step of the synthesis. Lowering the concentration to 2 mg/mL increased the yield to 8.75%, a modest improvement. Finally, with a 15

	1	2	3	4	5
Time	15 mins	1 hour	15 mins	15 mins	15 mins
[Oxine]	1 mg/mL	1 mg/mL	5 mg/mL	2 mg/mL	2 mg/mL
pH	~7	~7	~7	~7	~8.5-9
Yield	1.87%	3.12%	81.25%	8.75%	52.8%

Figure 4.2. Optimization of ^{89}Zr-oxinate synthesis.
Table of 5 sets of conditions used in order to optimize the ^{89}Zr-oxinate. The optimal conditions were determined to be 15 minutes, 2 mg/mL oxine, and pH 8.5-9 as determined by radio-instant thin layer chromatography.

	1	2	3	4
Allograft	IP (PBS, 35 days pre-injection)	IP (PBS, 35 days pre-injection)	IP (matrigel, 3 days pre-injection)	IP (matrigel, 7 days pre-injection)
T Cell Route of Administration	IP	IV	IP (contralateral)	IP (contralateral)

Figure 4.3. Experimental plan for *in vivo* CAR T cell tracking.
Groups of C57Bl/6 female mice were inoculated with ID8 tumors intraperitoneally by injection of 5.0×10^6 cells in a 150 uL cell suspension in PBS (experiments 1-2). For the Matrigel model, 5.0×10^6 cells in a 150 uL cell suspension of a 1:1 mixture of fresh media/Matrigel were injected IP on the contralateral side of the CAR T cell injection (experiments 3-4). Experiments were performed approximately 35 days following the injection of the cancer cells for the IP disseminated model and 3 or 7 days following implantation for the Matrigel model with the T cells injected on Day 0 either IP or IV.

minute duration, 2 mg/mL oxine concentration, and pH of 8.5, we were able to increase the yield to 52.8% which was in range with the published value of 60%. Instant thin layer chromatography of the product revealed radiochemical purity of > 99%. The resulting product was diluted in PBS for cell labeling. Activated CAR T cells were obtained from the Brentjens Laboratory and labeled with the ^{89}Zr-oxine complex by incubating 10^7 cells with 20-30 μCi of ^{89}Zr-oxine at room temperature for 30 minutes. The CAR T cells were washed three times with PBS and the pellet activity assayed on a gamma counter to determine labeling efficiencies ranging from 41.8% to 49.4%, values within range of the published protocol.

PET Imaging of CAR T Cells In Vivo

To track the CAR T cells in vivo and in order to gain insight into the role of IL-12 on armored CAR T cells, we utilized a syngeneic ovarian cancer animal model in four imaging experiments (Figure 4.3). In experiment 1 and 2, we injected murine ovarian cancer cells (ID8) intraperitoneally 35 days prior to the injection of CAR T cells in order to mimic late stage peritoneal disease in a model system with a fully intact immune system. The route of administration for the CAR T cells in experiment 1 was intraperitoneal and for experiment 2, intravenous injection via the tail vein. PET images were acquired on Days 1, 2, 5, and 7 after injection with 10^7 CAR T cells.

In experiment 1 (Figure 4.4), the activity in the mouse was mostly isolated to the abdomen in a seemingly random, diffuse distribution. There were no regions of persistent activity observed besides the high spine activity. This is in contrast to the images of the animal injected with 4H11 IL-12 CAR T cells which revealed a large region of high activity concentration in the left abdomen (white arrow) which persisted up to Day 2 and then diminished. In the images of the animal injected

Allograft	IP (PBS, 35 days pre-injection)
T Cell Route of Administration	IP

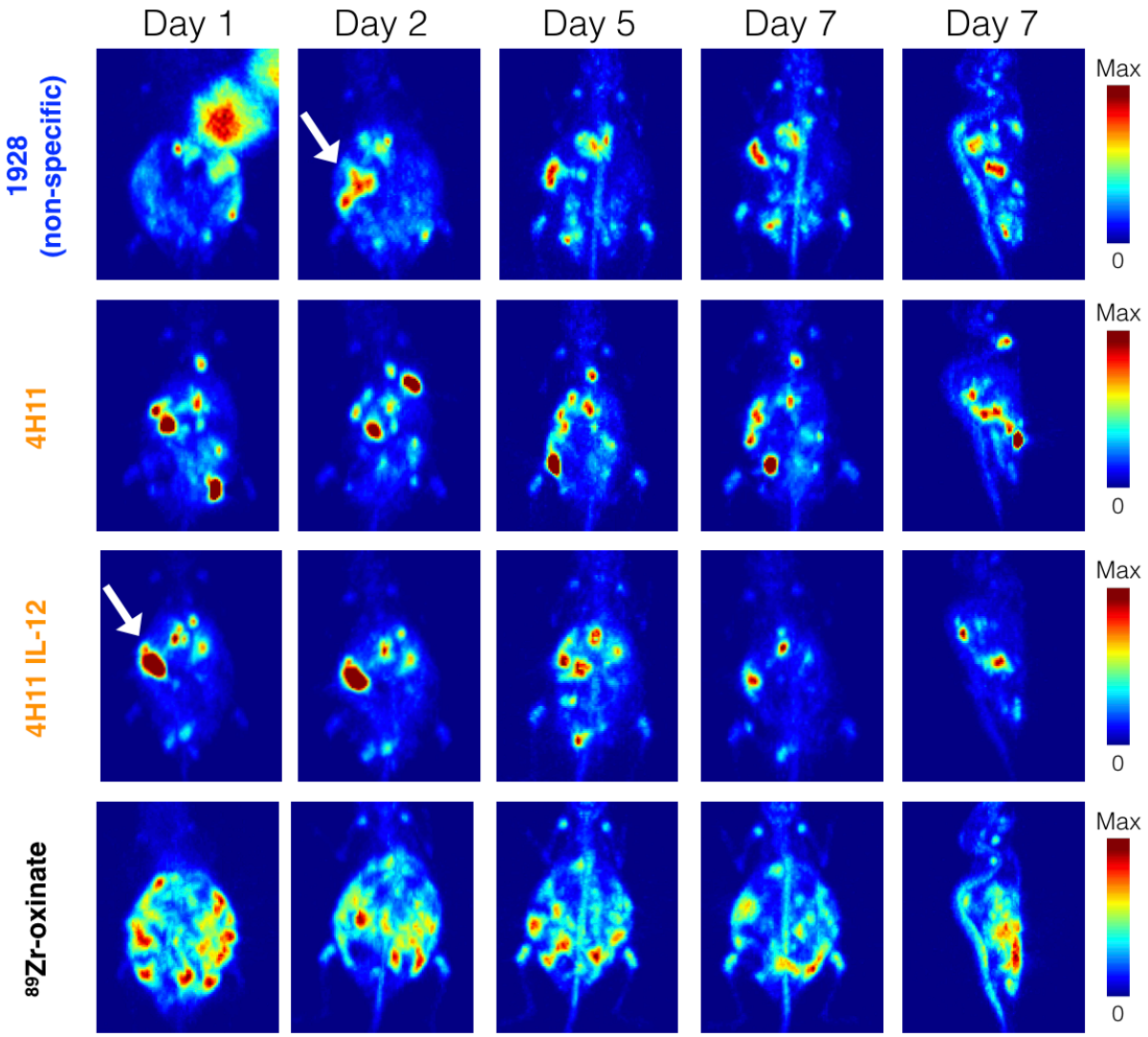

Figure 4.4. Serial PET images of CAR T cells *in vivo:* Experiment 1.
Small-animal serial PET imaging in an intraperitoneal disseminated ovarian cancer tumor model with IP injection of radioactivity. Maximal intensity projection (MIP) PET images of specified radiolabeled CAR T cells or free ^{89}Zr-oxinate (4-7 μCi in 500 μL of PBS injected IP) in C57Bl/6 mice bearing MUC16-positive ID8 murine ovarian cancer. Final column of images are sagittal cross-section MIPs of final time point. White arrows indicate areas of moderately retained radioactivity.

with 4H11 CAR T cells, there were no areas of persistent activity observed, but instead drifting areas of activity. On the other hand, the images of the non-specific CAR T cells (1928) revealed a scattering of abdominal activity with one foci (white arrow) that became apparent on Day 2 that persisted throughout Day 7.

In experiment 2, the same animal model was used as in experiment 3, but the route of administration for the CAR T cells was intravenous via the tail vein. The images of the ^{89}Zr-oxinate control in this experiment revealed high radioactivity concentration in the liver, almost exclusively. Interestingly, the images for the CAR T cells in this experiment appeared similar to one another. They showed high activity concentration within the liver and the spleen, with minimal bone activity. The images of the 4H11 CAR T cells showed diminishing liver activity from Day 1 to Day 7 while the non-specific and armored CAR T cell images showed consistent levels of activity within the liver through Day 7.

Using the previous intraperitoneal model proved difficult in terms of analyzing the images, so we altered the animal model in the following two experiments by injecting the mice intraperitoneally with a 1:1 mixture of ID8 cells and matrigel 3 days prior to injection of the CAR T cells. In this model, we expected the tumor to form in one mass on one side of the animal as opposed to disseminated disease throughout the abdomen (Figure 4.6). Injections of the CAR T cells, and control, were performed on the contralateral side. Images of ^{89}Zr-oxinate revealed one region of high activity in the lower portion of the abdomen that persisted from Day 1 through Day 7. The images of all of the CAR T cells look similar with the majority of the activity, from Day 1 to Day 7, localizing to the left region of the abdomen, the side where the tumor cells were implanted. In experiment 4, similar to the previous experiment, we injected ID8 cells intraperitoneally with

Allograft	IP (PBS, 35 days pre-injection)
T Cell Route of Administration	IV

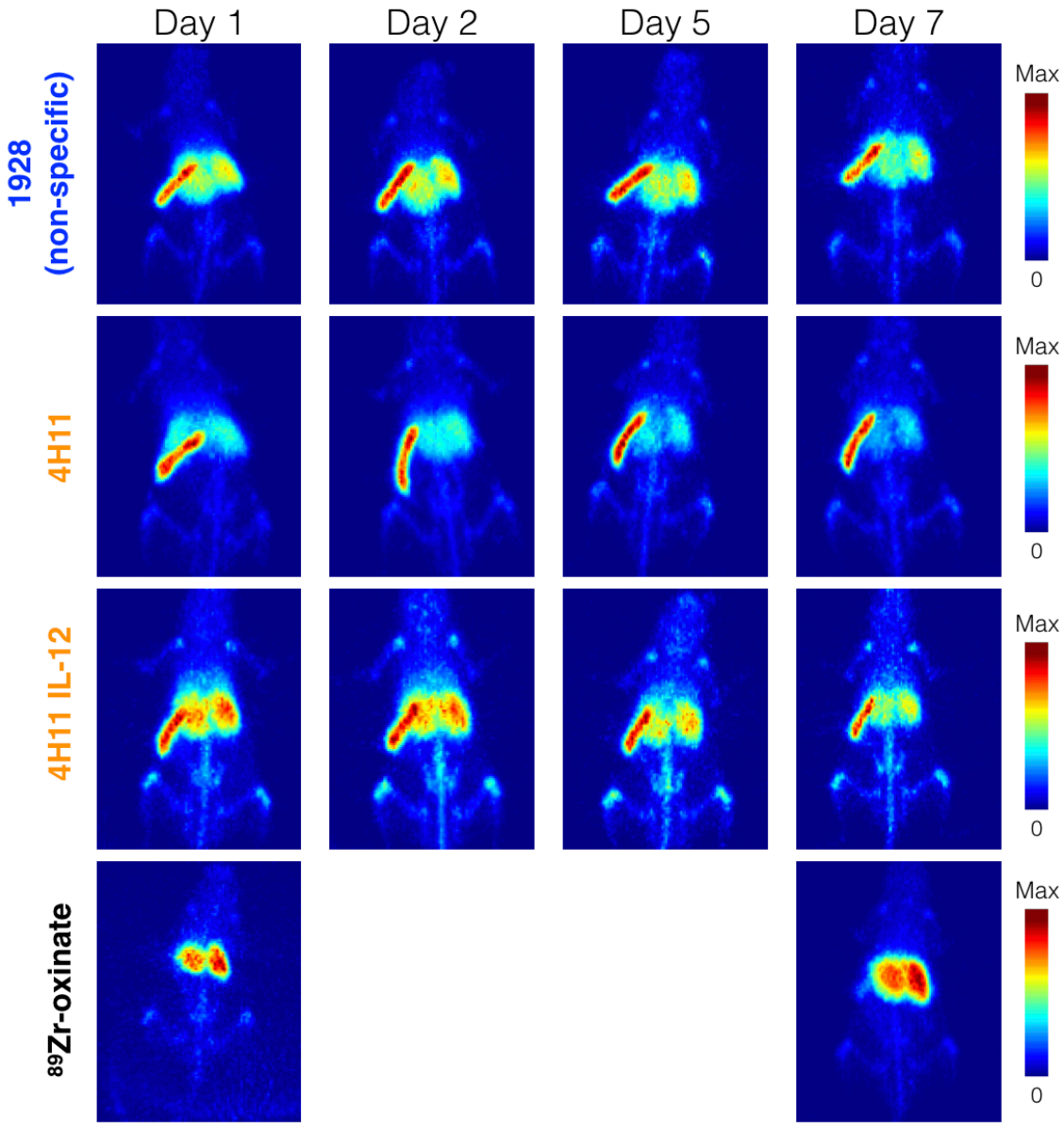

Figure 4.5. Serial PET images of CAR T cells *in vivo:* Experiment 2.
Small-animal serial PET imaging in an intraperitoneal disseminated ovarian cancer tumor model with intravenous injection of radioactivity. Maximal intensity projection (MIP) PET images of specified radiolabeled CAR T cells or free ^{89}Zr-oxinate (4-7 μCi in 500 μL of PBS injected IP) in C57Bl/6 mice bearing MUC16-positive ID8 murine ovarian cancer.

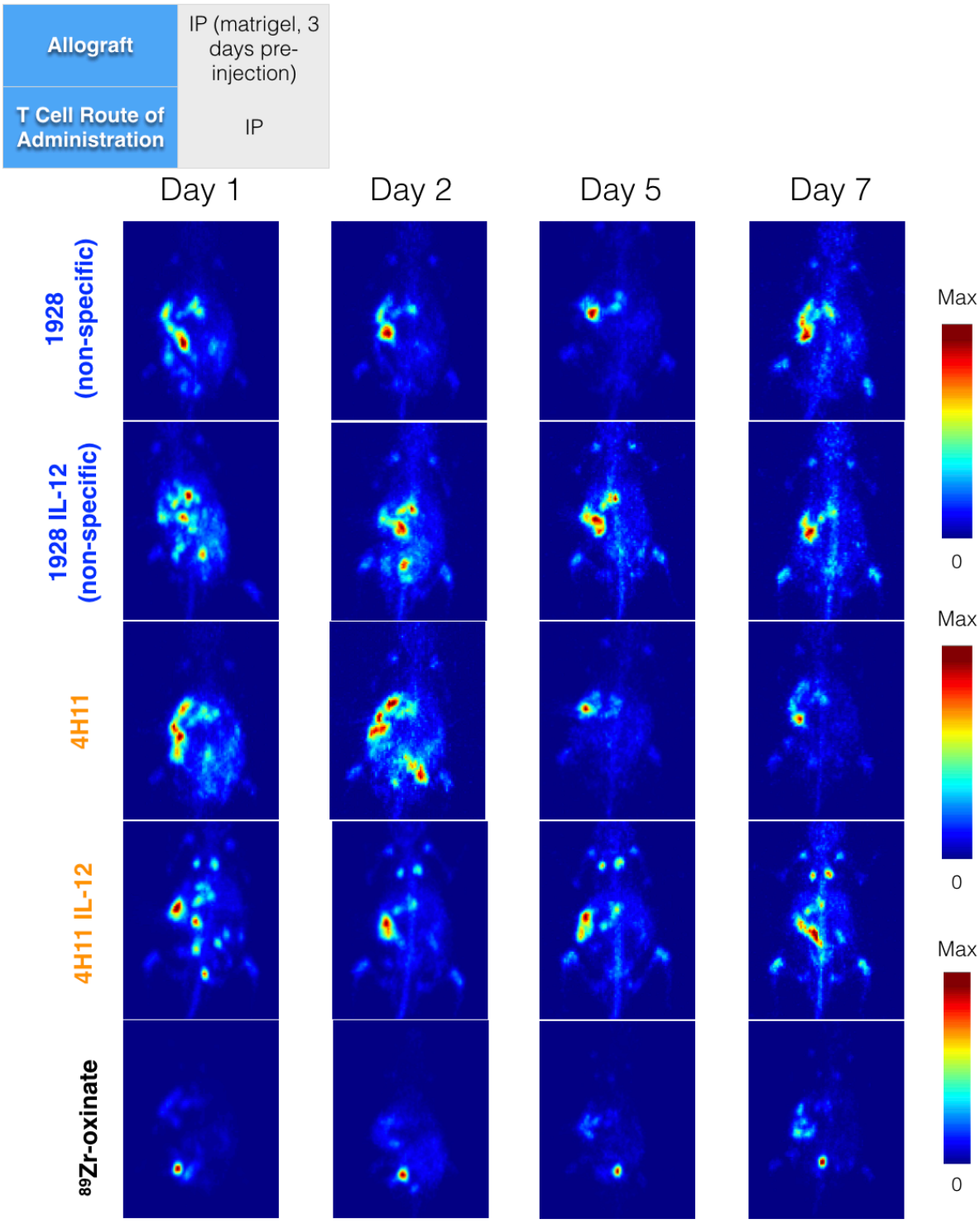

Figure 4.6. Serial PET images of CAR T cells *in vivo:* Experiment 3.
Small-animal serial PET imaging in an intraperitoneal Matrigel ovarian cancer tumor model. Maximal intensity projection (MIP) PET images of specified radiolabeled CAR T cells or free ^{89}Zr-oxinate (4-7 μCi in 500 μL of PBS injected IP) in C57Bl/6 mice bearing MUC16-positive ID8 murine ovarian cancer.

matrigel, and then injected the CAR T cells 7 days later. These images revealed no significant patterns or persistent regions of high activity at the tumor site.

Conclusions

Using the ^{89}Zr CAR T cell labeling approach, we were unable to conclusively visualize T cells trafficking to the tumor site. Utilizing a disseminated ovarian cancer model, the most clinically relevant model, made it difficult to determine if the areas of high activity observed in the images were truly sites of neoplasia. Further, our experiments which utilized matrigel to assist in the formation of one solid tumor mass did not appear to improve localization of the CAR T cells to the implantation site. In experiment 2 (Figure 4.5), we were able to clearly demonstrate a difference in the ^{89}Zr-oxinate control and the CAR T cells, indicating that the T cells were, in fact, labeled with ^{89}Zr-oxinate, however, they did not appear to extravasate from circulation and traffic tumor tissue within the abdomen. One potential reason why these experiment were unable to provide conclusive evidence of targeted T cell tracking include potential disruption of T cell activity due to the labeling reaction. In vitro assays to measure T cell viability and activity post-radiolabeling should be performed in the future. In addition, the use of a more straightforward subcutaneous model should be considered to verify T cell trafficking before continuing with more complex, relevant model.

Materials and Methods

General Laboratory Procedures

Unless otherwise noted, all chemicals were acquired from Sigma-Aldrich (St. Louis, MO) and used as received and all instruments were calibrated and maintained in accordance with standard

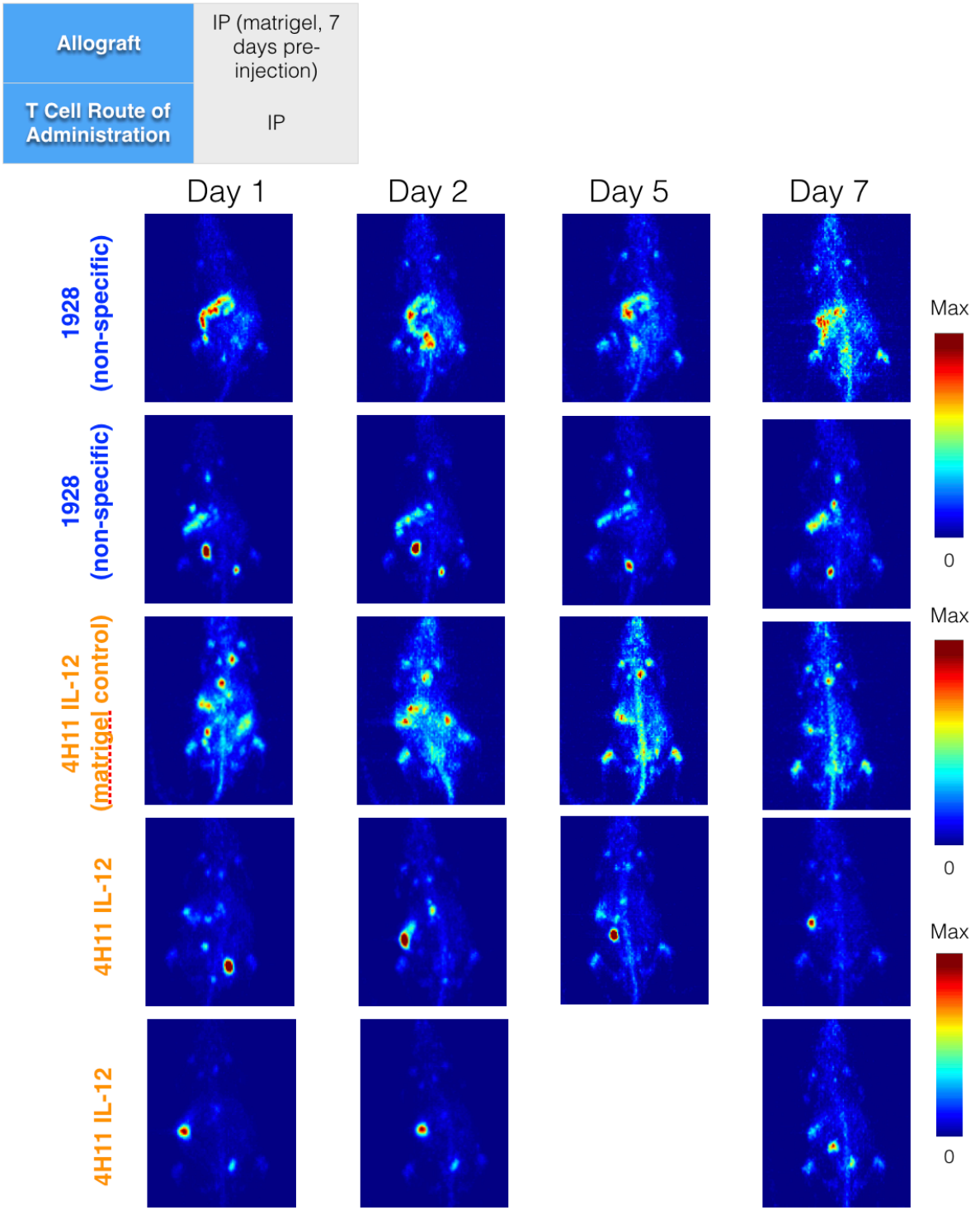

Figure 4.7. Serial PET images of CAR T cells *in vivo:* Experiment 4.
Small-animal serial PET imaging in an intraperitoneal Matrigel ovarian cancer tumor model. Maximal intensity projection (MIP) PET images of specified radiolabeled CAR T cells (4-7 μCi in 500 μL of PBS injected IP) in C57Bl/6 mice bearing MUC16-positive ID8 murine ovarian cancer.

procedures. ^{89}Zr was produced at Memorial Sloan Kettering Cancer Center on a TR19/9 cyclotron (Ebco Industries Inc.) via the ^{89}Y(p,n)^{89}Zr reaction and purified to yield ^{89}Zr with a specific activity of 196–496 MBq/mg. ^{89}Zr was received after target processing as ^{89}Zr-oxalate in 1.0 M oxalic acid. The solution was neutralized with 1.0 M sodium carbonate to reach pH ~7. Activity measurements were made using a CRC-15R Dose Calibrator (Capintec). For the quantification of activities, samples were counted on an Automatic Wizard gamma counter (Perkin Elmer). The radiolabeling of ligands was monitored using instant thin-layer chromatography paper (Agilent Technologies) and analyzed on a Bioscan AR-2000 radio-ITLC plate reader using Winscan Radio-TLC software (Bioscan Inc., Washington, DC). All in vivo experiments were performed according to protocols approved by the Memorial Sloan Kettering Institutional Animal Care and Use Committee (Protocol 08□ 07□ 013).

Xenograft Mouse Models

Eight to ten week old C57Bl/6 female mice were purchased from Charles River Laboratories (Kingston, NY). Animals were housed in ventilated cages, were given food and water ad libitum, and were allowed to acclimatize for approximately 1 week prior to inoculation. ID8 tumors were induced intraperitoneally by injection of 5.0×10^6 cells in a 150 μL cell suspension. For the Matrigel model, 5.0 × 106 cells in a 150 μL cell suspension of a 1:1 mixture of fresh media/BD Matrigel (BD Biosciences, Bedford, Ma) were injected IP on the contralateral side of the CAR T cell injection. Experiments were performed approximately 35 days following the injection of the cancer cells for the disseminated model and 3 or 7 days following implantation for the Matrigel model.

Synthesis of ^{89}Zr-Oxine Complex

To prepare ^{89}Zr-oxinate, the neutralized ^{89}Zr-oxalate solution (500-600 μCi) was added to a glass reaction vessel containing 1 mL of a 2 mg/ml 8-hydroxyquinoline (oxine) solution in chloroform.

The vessel was shaken for 15 min and the product ^{89}Zr-oxinate was recovered from the chloroform phase by evaporation, redissolved in dimethyl sulfoxide (DMSO, 20 □ l) and diluted with phosphate-buffered saline (PBS, 2 mL).

^{89}Zr-Oxine Complex Cell Labeling

Activated CAR T cells were obtained from the Brentjens Laboratory and labeled with the ^{89}Zr-oxine complex by incubating 10^7 cells in phosphate-buffered saline with 20-30 μCi of ^{89}Zr-oxine at room temperature for 30 minutes. The CAR T cells were washed three times with PBS and the pellet activity assayed on a gamma counter to determine labeling efficiencies ranging from 41.8% to 49.4%.

Tracking of ^{89}Zr-labeled CAR T Cells with PET

To track the CAR T cells in vivo, 5×10^6 ^{89}Zr-labeled T cells (4-7 μCi) were injected intraperitoneally or intravenously via the tail vein. PET imaging experiments were conducted on an Inveon PET/CT scanner (Siemens Healthcare Global). Animals were anesthetized by inhalation of 2% isoflurane (Baxter Healthcare, Deerfield, IL) and medical air gas mixture and placed within the scanner with anesthesia maintained using 2% isoflurane and medical air gas mixture. PET data for each mouse were recorded via static scans on Days 1, 2, 5 and 7 post-injection of T cells. An energy window of 350-700 keV and a coincidence timing window of 6 ns were used. Data were sorted into 2D histograms by Fourier rebinning, and transverse images were reconstructed by filtered back-projection (FBP) into a 128 × 128 × 63 (0.72 × 0.72 × 1.3 mm3) matrix. The counting rates in the reconstructed images were converted to activity concentrations (percentage injected dose per gram of tissue, %ID/g) by use of a system calibration factor derived from the imaging of a mouse-sized

water-equivalent phantom containing ^{89}Zr. Images were analyzed using ASIPro VM software (Concorde Microsystems).

CHAPTER 5: Summary, Conclusions, and Future Directions

This thesis project began with the overall goal of addressing an unmet need in the area of ovarian cancer diagnosis. The overwhelming statistics associated with ovarian cancer morbidity and mortality, along with the fact that a portion of patients that undergo surgery to remove suspicious adnexal masses are determined to be false positives catapulted our interest in pursuing this endeavor. As the niche field of ^{89}Zr immunoPET has been gaining increasing amounts of success pre-clinically and clinically over the past decade, we ventured to find an overexpressed antigen to exploit as a target for ^{89}Zr-labeled immunoconjugates.

The MUC16/CA-125 glycoprotein stood out in the literature as a prominent antigen in the ovarian cancer field and its success as a target for PET imaging, to date, has not been fully realized. Beginning with a panel of twelve murine antibodies, we identified characteristics that embody the ideal immunoPET agent including high specific activity, stability, affinity, immmunoreactivity, and internalization. At the *in vivo* level, ideal agents would display specificity for the target, preferentially accumulating in the tumor tissue, and low non-target organ uptake leading to images with high contrast. By using these criteria and performing the associated assays, we were able to narrow down a panel of twelve antibodies to three which were taken forward into *in vivo* studies. The three candidates were evaluated in a subcutaneous ovarian cancer model where they exhibited varying biodistribution profiles. ^{89}Zr-DFO-4H11 revealed itself as the leading candidate due to its superior tumor-to-background ratios as compared to the other two candidates. Delineating the tumor as early as 24 hours post-injection, and clearing from background tissues gradually throughout 96 hours, ^{89}Zr-DFO-4H11 showed the most promise as a radiotracer for the diagnosis of ovarian cancer. Future work in this portion of the thesis revolves around the humanization of this tracer and its potential translation into a clinical trial.

Literature searches also yielded another overexpressed antigen in ovarian cancer that appeared to be a promising target, L1CAM. Serial PET imaging of a humanized IgG1 wildtype antibody against L1CAM in a subcutaneous ovarian cancer xenograft model revealed even better tumor-to-background ratios than ^{89}Zr-DFO-4H11. Interestingly, however, lymph nodes within the animals were observed to have high radioactivity concentrations at all time points post-injection. This is a phenomenon that was also observed with ^{89}Zr-DFO-4H11, as well as other radioimmunoconjugates from our laboratory. In our case, these lymph nodes were false positive signals as histopathologic analysis revealed no signs of neoplastic cells. These observations stimulated the formation of a new question: what is the cause of the high lymph node uptake and is it a tracer specific property? We hypothesized this could be due to local expression or the antigen or binding of the Fc region of the antibodies to Fc gamma receptors expressed on immune cells within the lymph nodes.

In order to evaluate this hypothesis, we developed a panel of L1CAM targeted antibodies, all with the exact same antigen binding domain, but with subtle modifications to the Fc region. *In vivo* imaging and biodistribution experiments showed that antibodies with Fc region modifications that are known to enhance Fc gamma receptor binding exhibited significantly increased lymph node uptake. Conversely, the antibodies with Fc modifications that are known to decrease Fc gamma receptor binding demonstrated significantly lower lymph node uptake. These observations suggest that Fc binding, not local expression of the antigen, plays a role in the lymph node uptake we observed.

Following the observation of high renal uptake of ^{89}Zr-DFO-HuE71-4 WT (a wildtype IgG4 targeting L1CAM), we hypothesized that this renal accumulation was secondary to the IgG4 specific property of dynamic fab arm exchange. By introducing a single amino acid mutation in the IgG4 Fc region (eliminating dynamic fab arm exchange), we were able to observe a significant decrease in the

renal radioactivity concentration validating our hypothesis that dynamic fab arm exchange plays a role in renal accumulation, a finding that was confirmed with a non-specific IgG4 as well.

Further, by imaging these five L1CAM antibodies with Fc modifications, we were able to demonstrate that ^{89}Zr-DFO-HuE71-1 Aglyco (low Fc gamma receptor binding IgG1) displayed a superior biodistribution profile with the highest tumor uptake and lowest background tissue uptake by 96 hours. Accordingly, we took HuE71-1 Aglyco forward into a ^{177}Lu radioimmunotherapy study where it displayed significant efficacy, delaying tumor progression in a subcutaneous ovarian cancer model.

We find all of these specific results very intriguing and informative, but even more so, we are delighted by the fact that we have been able to use molecular imaging techniques to explore the underlying biology of the Fc region of antibodies and the impact it has on *in vivo* behavior. We hope that these results will inspire others to incorporate more molecular imaging in terms of the design, development, and engineering of tools for various biomedical applications.

Appendix

Chapter 2

Antibody	Specific Activity	Immunoreactivity	Scatchard	Cell Uptake
9C9	4.35 µCi/µg	84.6 ± 4.4 %	9.02 ± 1.49 nM	11.89± 2.21 %ID
4H11	5.74 µCi/µg	88.3 ± 5.9 %	6.38 ± 1.20 nM	14.09 ± 1.34 %ID
2F4	3.57 µCi/µg	82.1 ± 3.4 %	9.27 ± 1.80 nM	9.86 ± 1.28 %ID
23D3	3.93 µCi/µg	83.1 ± 2.6 %	7.10 ± 1.14 nM	6.34 ± 1.96 %ID
7B12	5.32 µCi/µg	86.7 ± 4.7 %	9.95 ± 1.68 nM	8.41 ± 0.59 %ID
28F8	3.50 µCi/µg	82.8 ± 2.4 %	19.80 ± 1.09 nM	n/a
4C7	3.19 µCi/µg	76.3 ± 3.8 %	13.29 ± 2.89 nM	n/a
9B11	3.34 µCi/µg	71.5 ± 1.2 %	13.80 ± 2.92 nM	n/a
10A2	2.16 µCi/µg	68.3 ± 5.9 %	n/a	n/a
29G9	1.25 µCi/µg	62.0 ± 6.6 %	n/a	n/a
4A5	0.21 µCi/µg	67.2 ± 1.2 %	n/a	n/a
4A2	n/a	n/a	n/a	n/a

Figure A.2.1. Table of *in vitro* screen values of panel of MUC16 targeted antibodies.

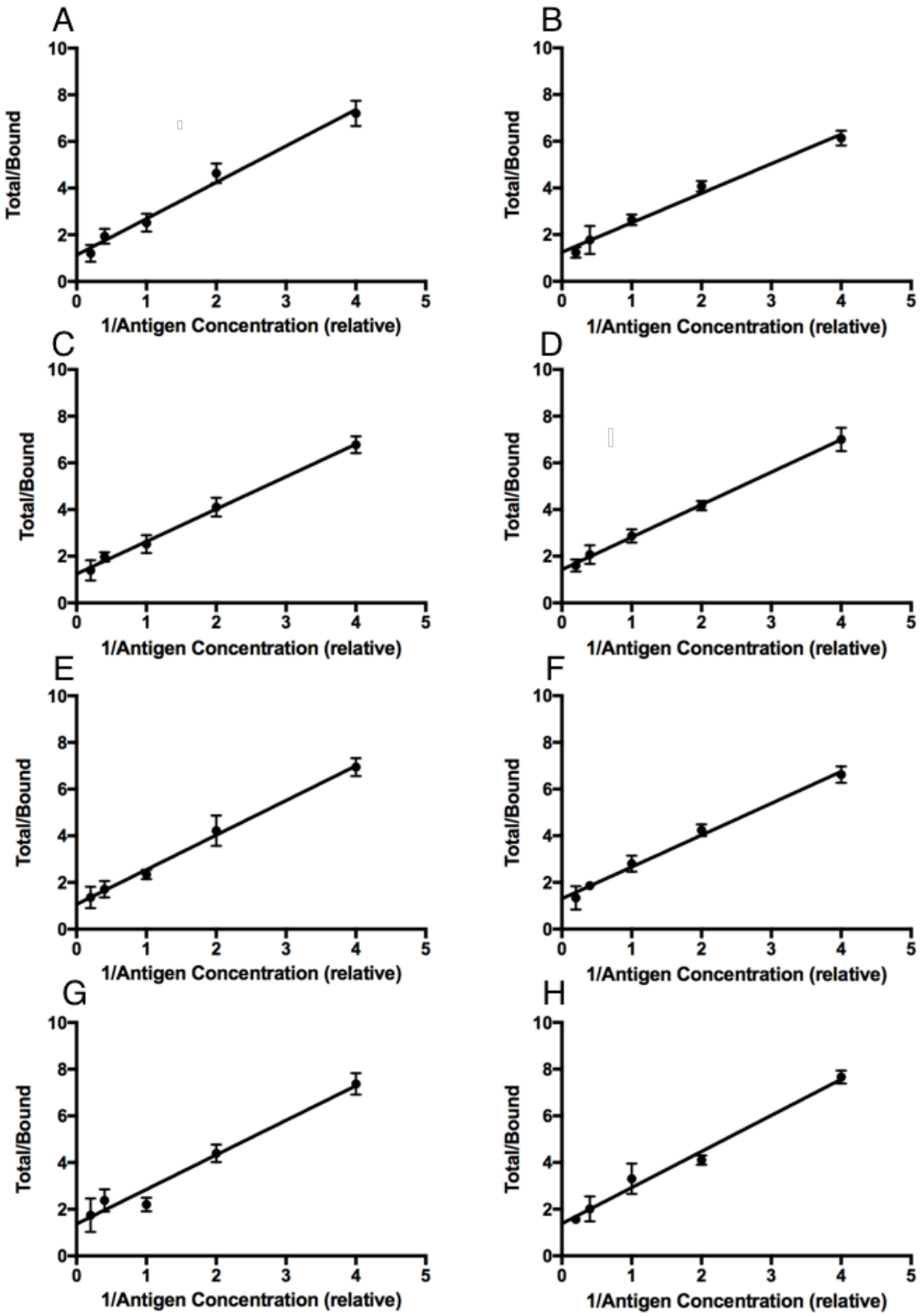

Figure A.2.2. Immunoreactivity of MUC16 antibodies.
(A) 2F4, (B) 23D3, (C) 28F8, (D) 4C7, (E) 9B11, (F) 10A2, (G) 29G9, (H) 4A5. Values displayed in Figure A.2.1.

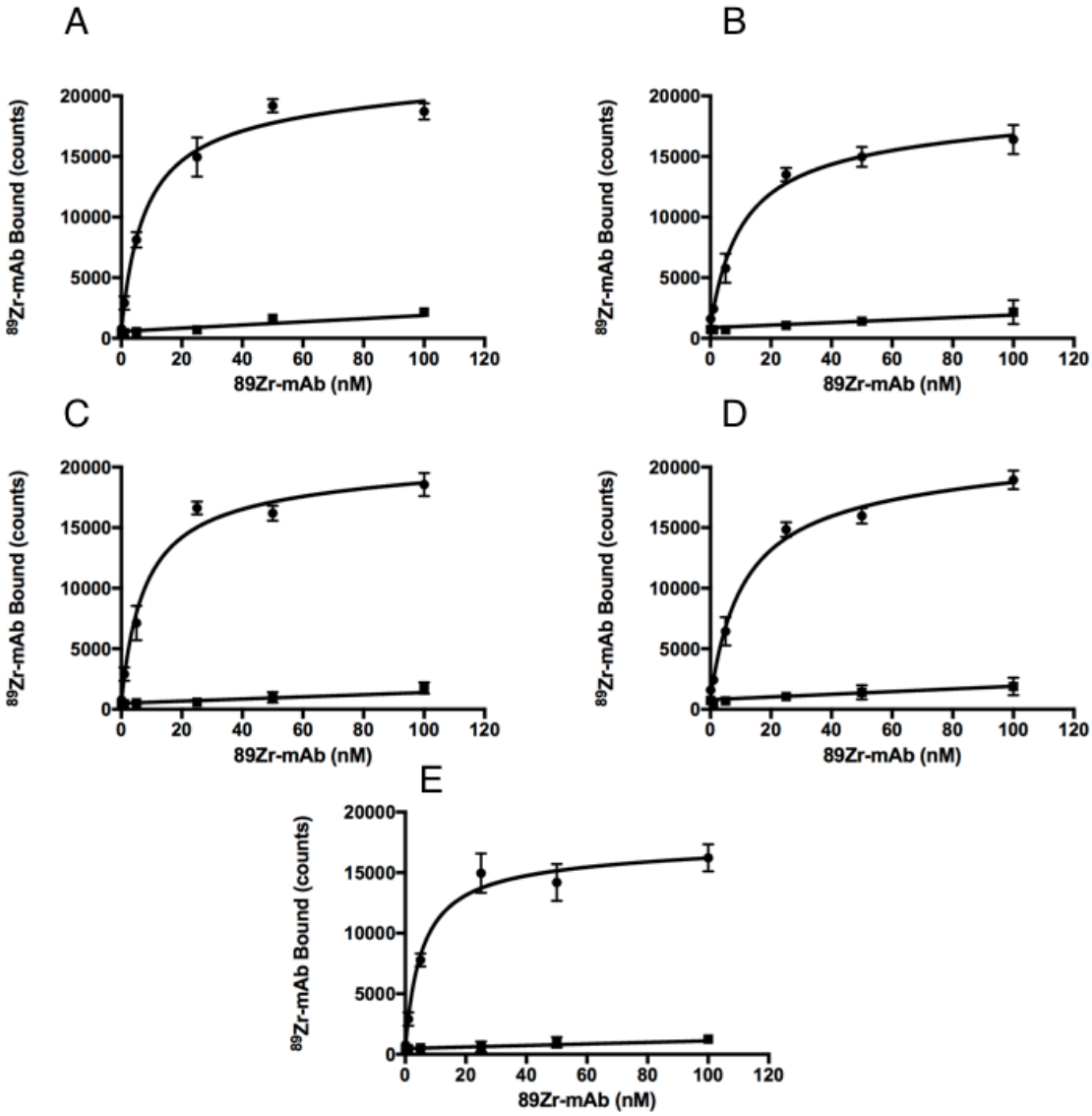

Figure A.2.3 Cell saturation binding assays of MUC16 antibodies.
(A) 2F4, (B) 23D3, (C) 28F8, (D) 4C7, (E) 9B11. Values outline in Figure A.2.1.

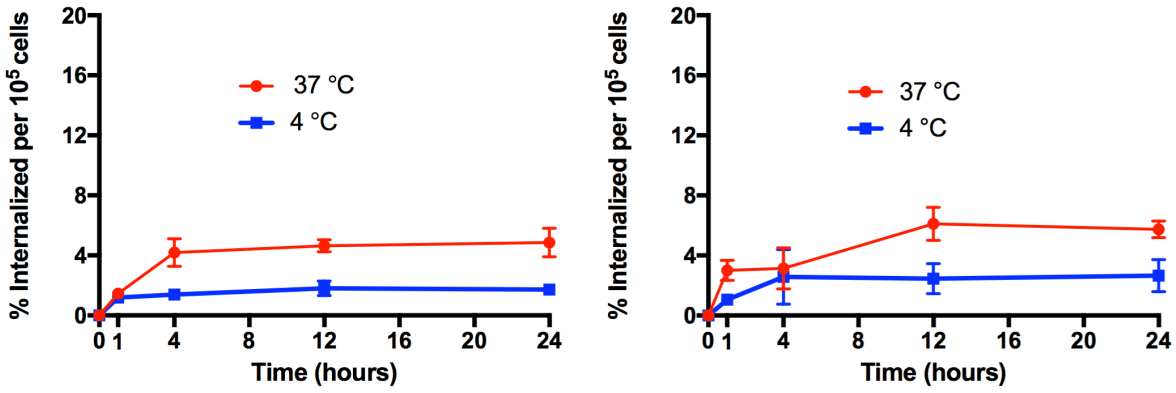

Figure A.2.4. Cell internalization assay of MUC16 antibodies.
Internalization of 2F4 (left) and 23D3 (right). Values outlined in Figure A.2.1.

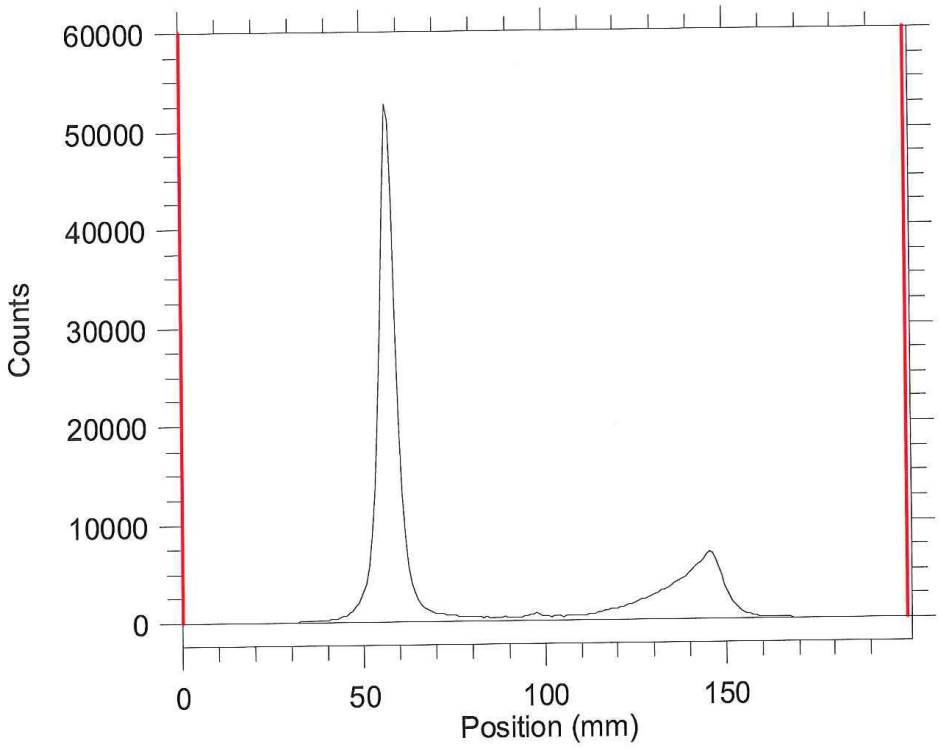

Figure A.2.5 Radio-ITLC of ^{89}Zr-DFO-29G9 crude reaction.

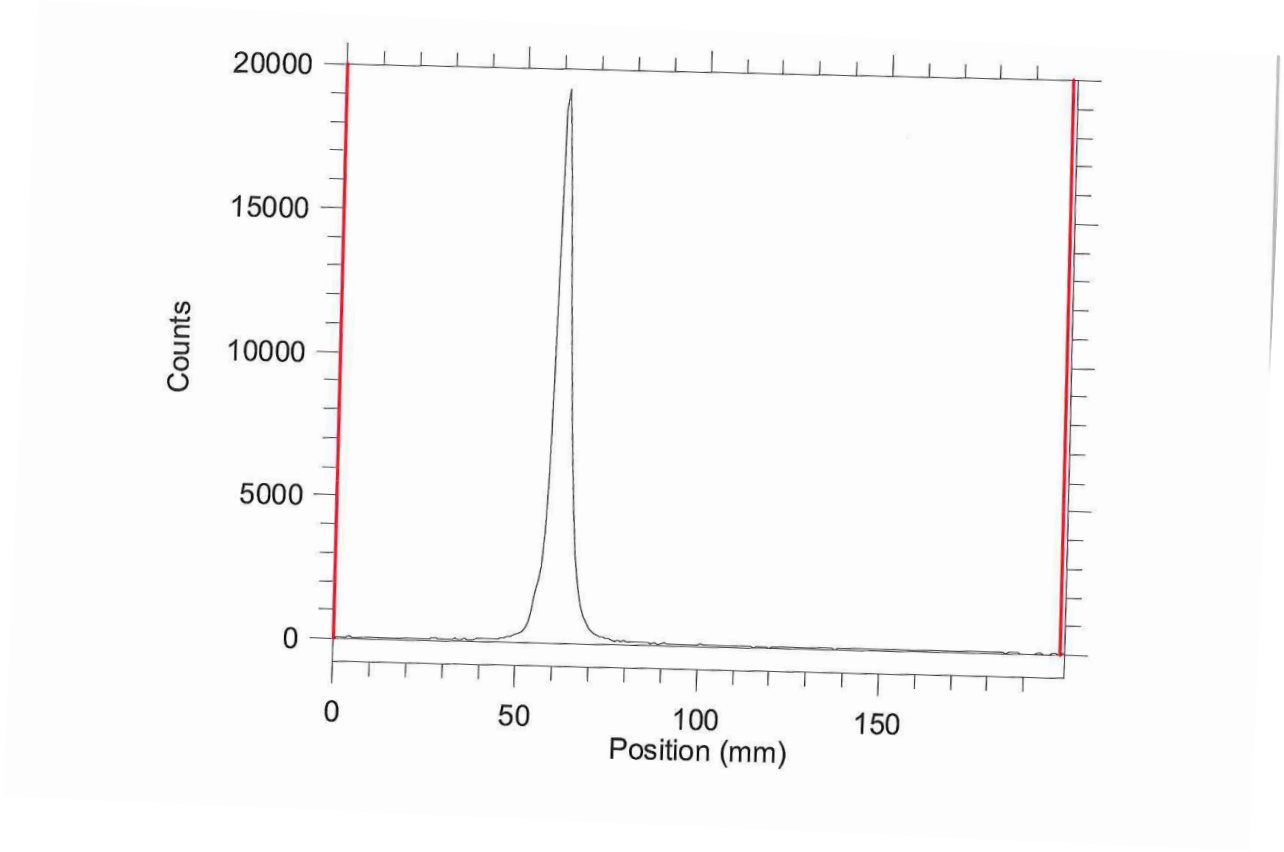

Figure A.2.6 Radio-ITLC of ^{89}Zr-DFO-29G9 purified.

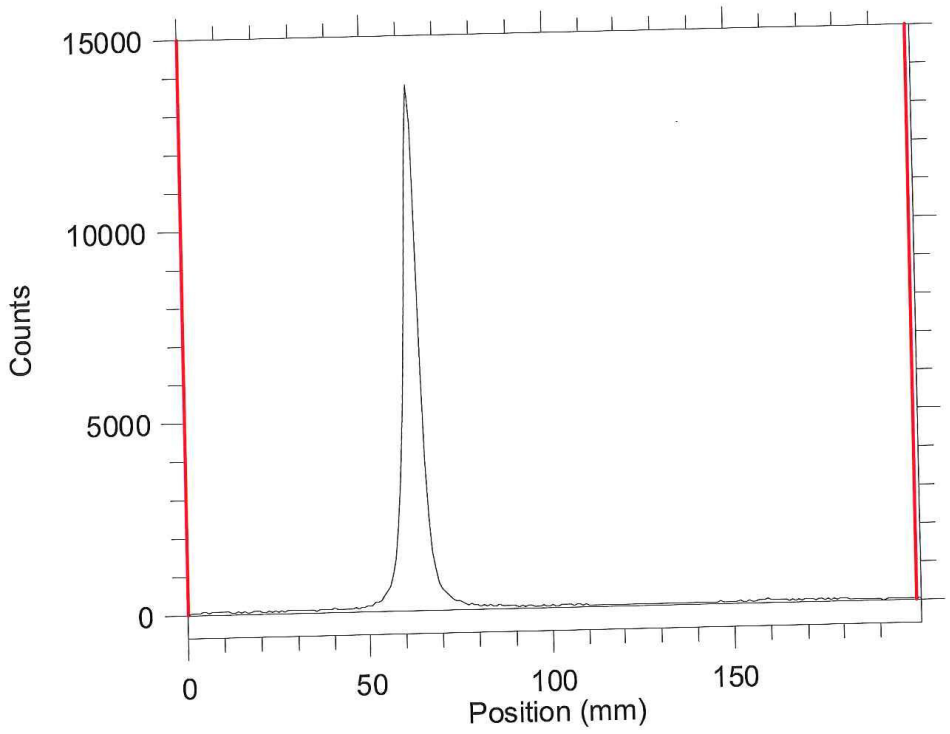

Figure A.2.7 Radio-ITLC of ^{89}Zr-DFO-9C9 purified reaction.

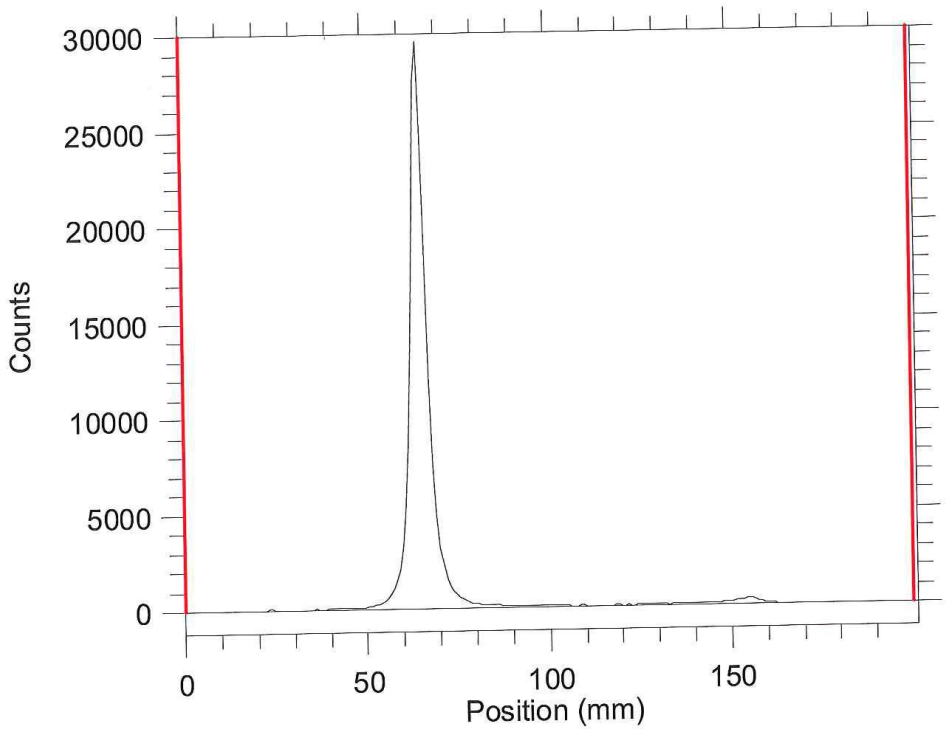

Figure A.2.8 Radio-ITLC of ^{89}Zr-DFO-4H11 purified reaction.

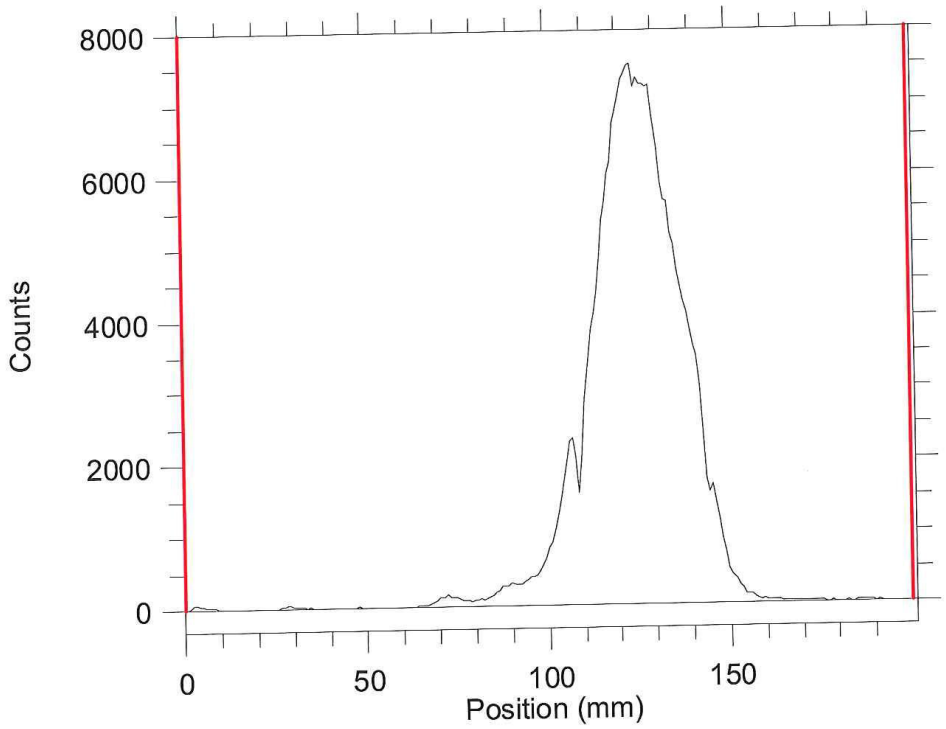

Figure A.2.9 Radio-ITLC of ^{89}Zr-DFO-4A2 crude reaction.

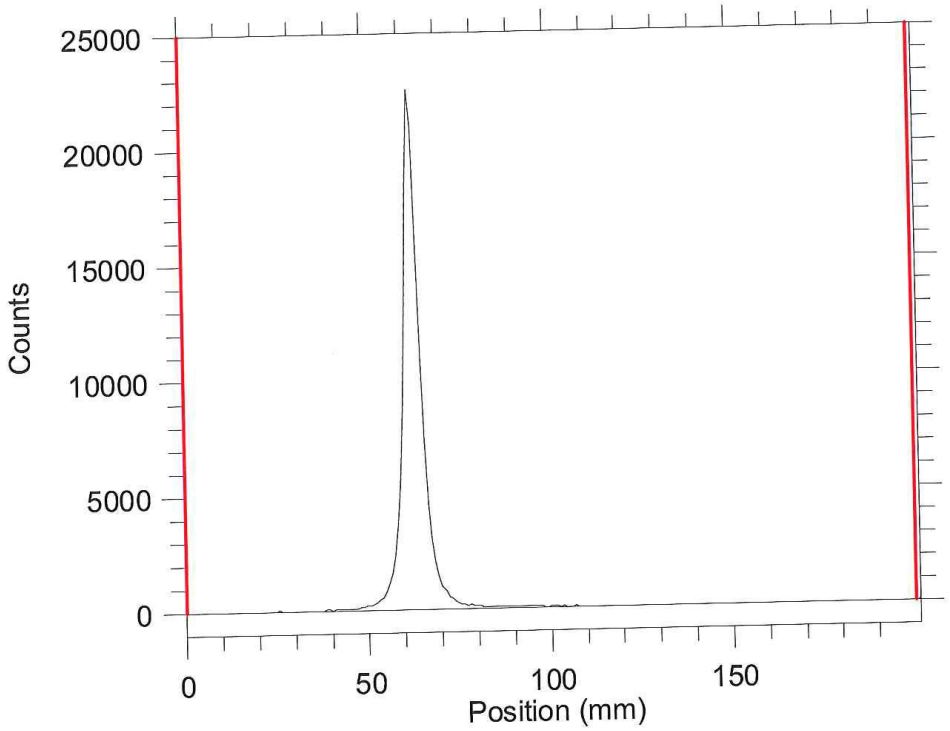

Figure A.2.10 Radio-ITLC of ^{89}Zr-DFO-2F4 purified reaction.

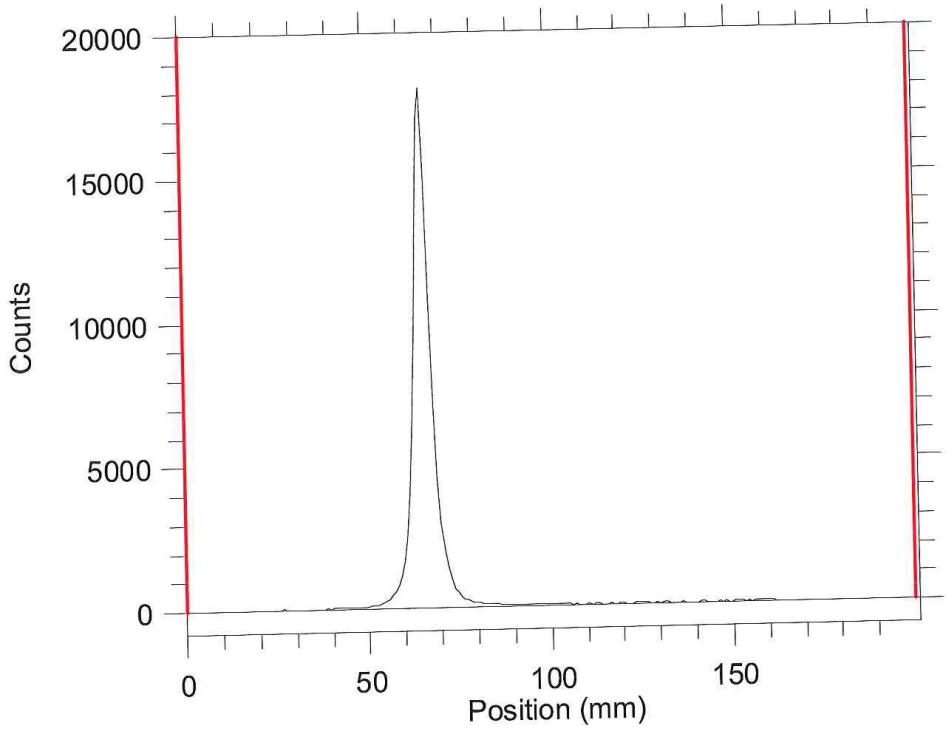

Figure A.2.11 Radio-ITLC of ^{89}Zr-DFO-23D3 purified reaction.

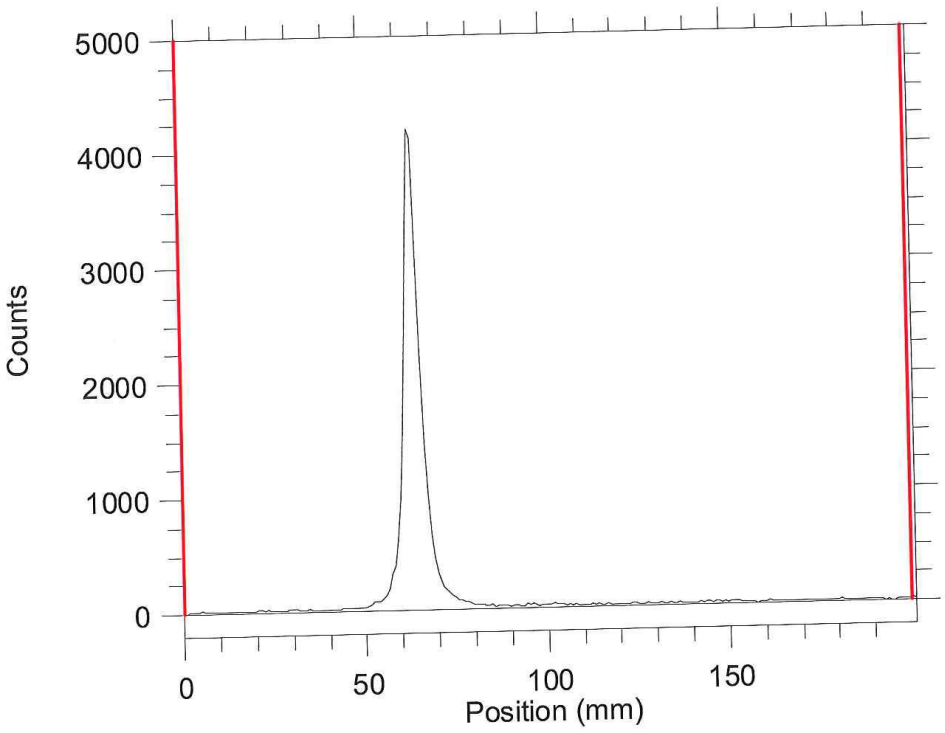

Figure A.2.12 Radio-ITLC of ^{89}Zr-DFO-7B12 purified reaction.

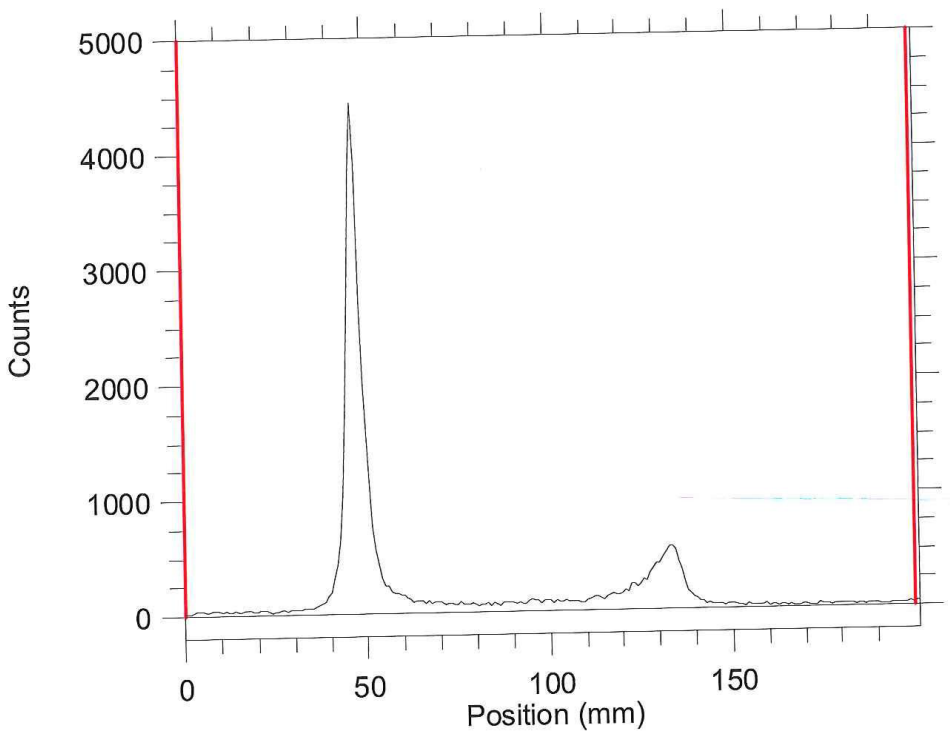

Figure A.2.13 Radio-ITLC of ^{89}Zr-DFO-10A2 crude reaction.

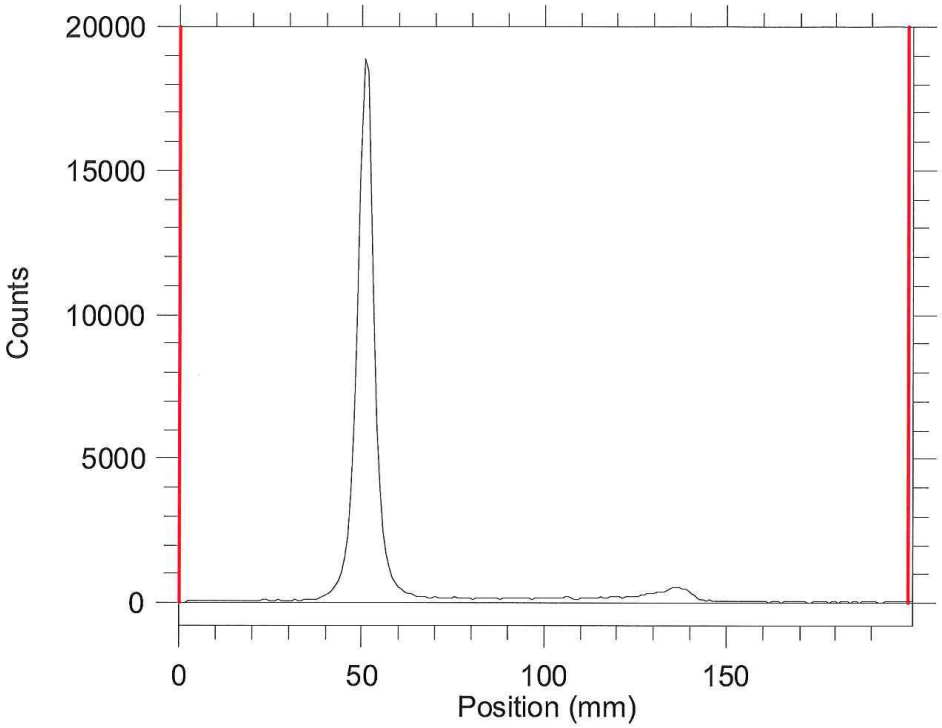

Figure A.2.14 Radio-ITLC of ^{89}Zr-DFO-10A2 purified reaction.

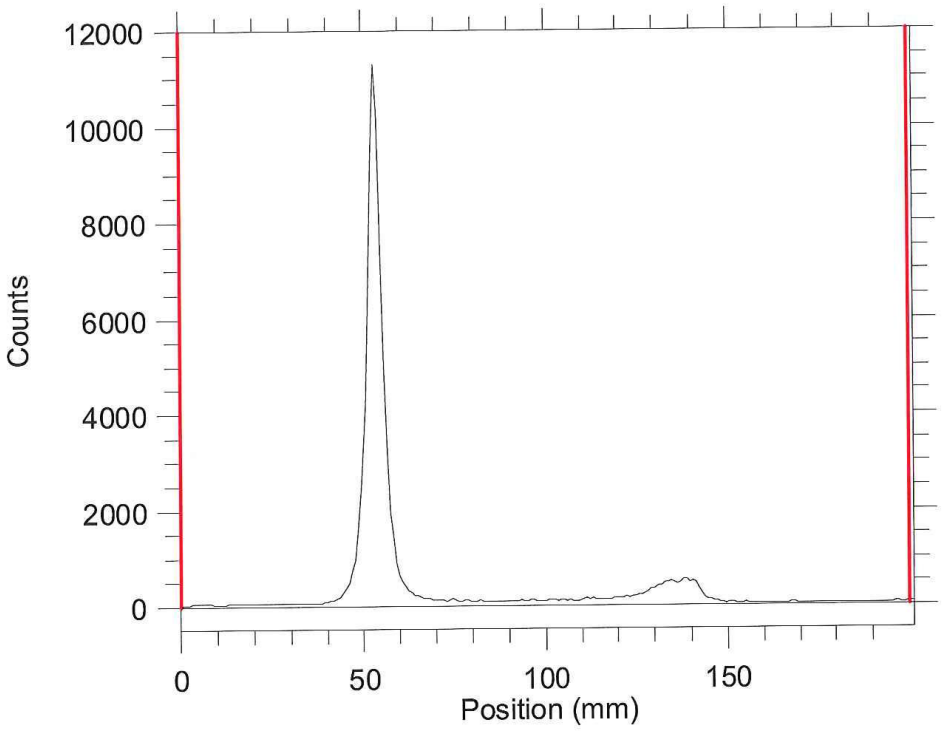

Figure A.2.15 Radio-ITLC of ^{89}Zr-DFO-9B11 crude reaction.

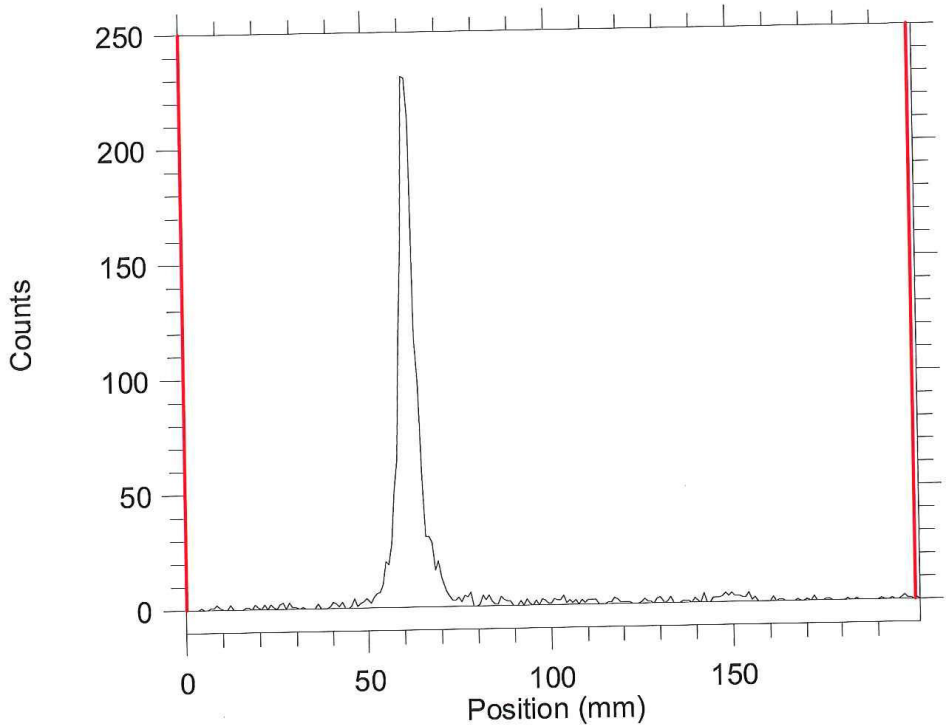

Figure A.2.16 Radio-ITLC of ^{89}Zr-DFO-9B11 purified reaction.

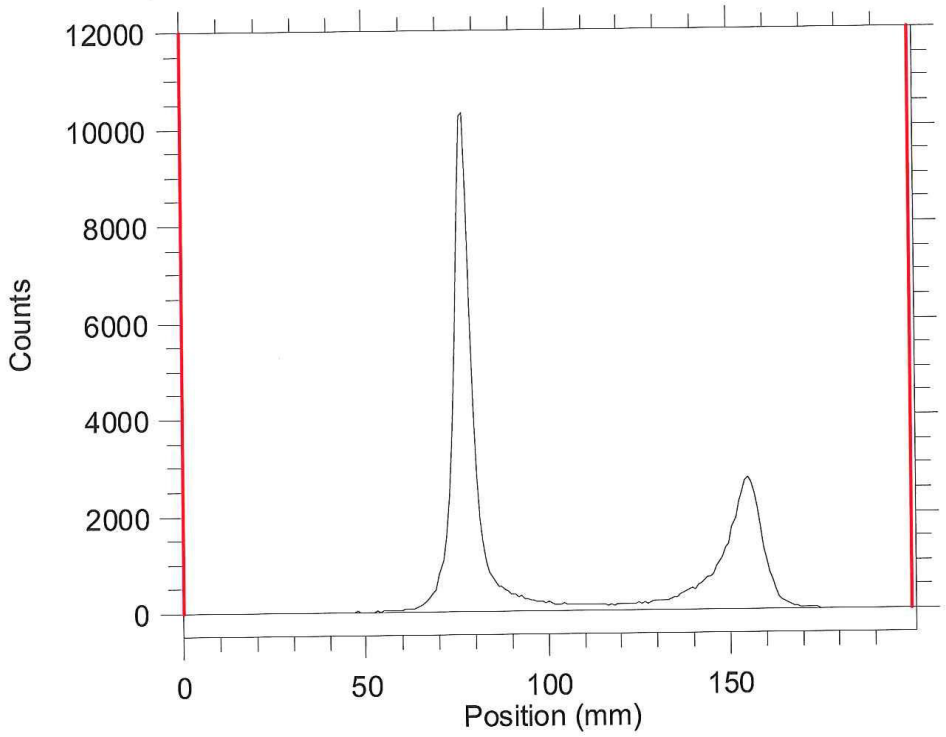

Figure A.2.17 Radio-ITLC of ^{89}Zr-DFO-4A5 crude reaction.

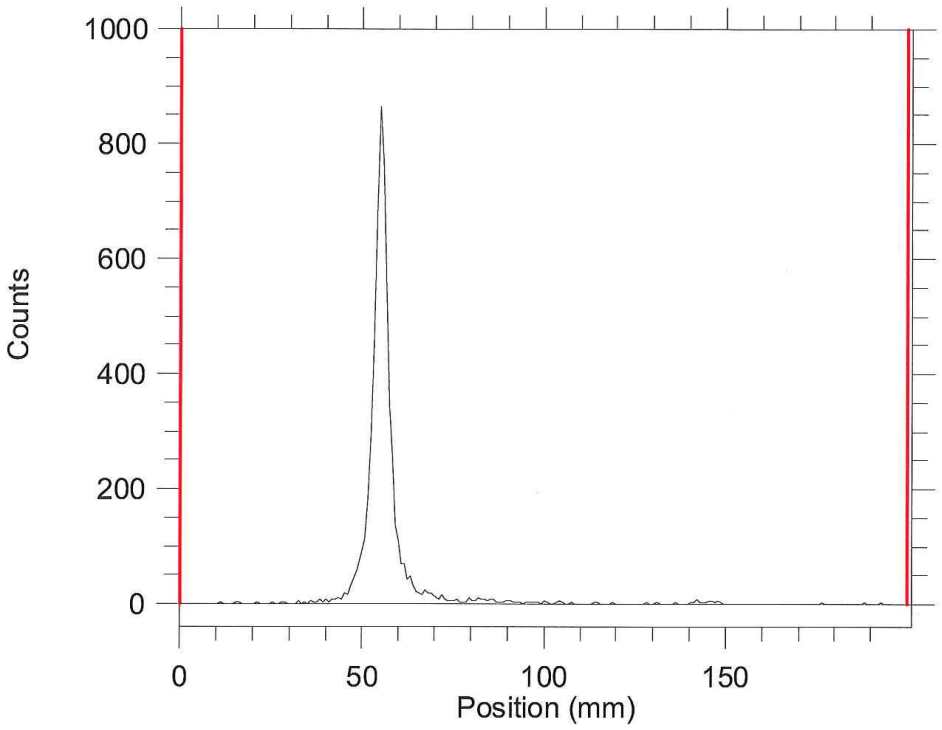

Figure A.2.18 Radio-ITLC of ^{89}Zr-DFO-4A5 purified reaction.

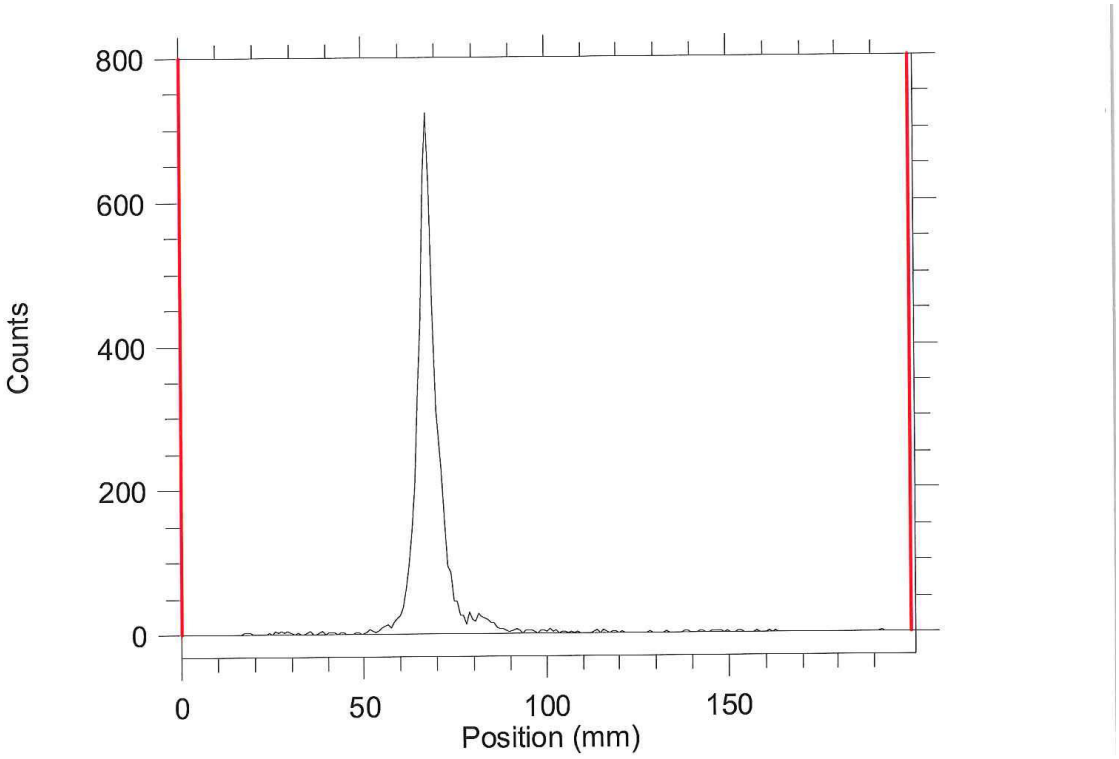

Figure A.2.19 Radio-ITLC of ^{89}Zr-DFO-28F8 purified reaction.

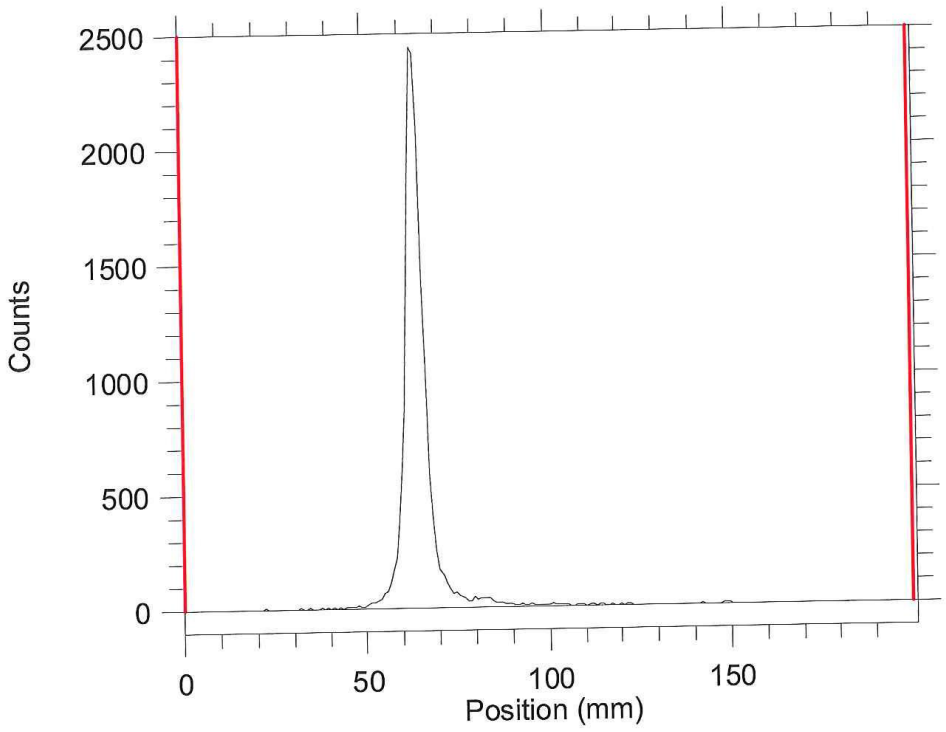

Figure A.2.20 Radio-ITLC of ^{89}Zr-DFO-4C7 purified reaction.

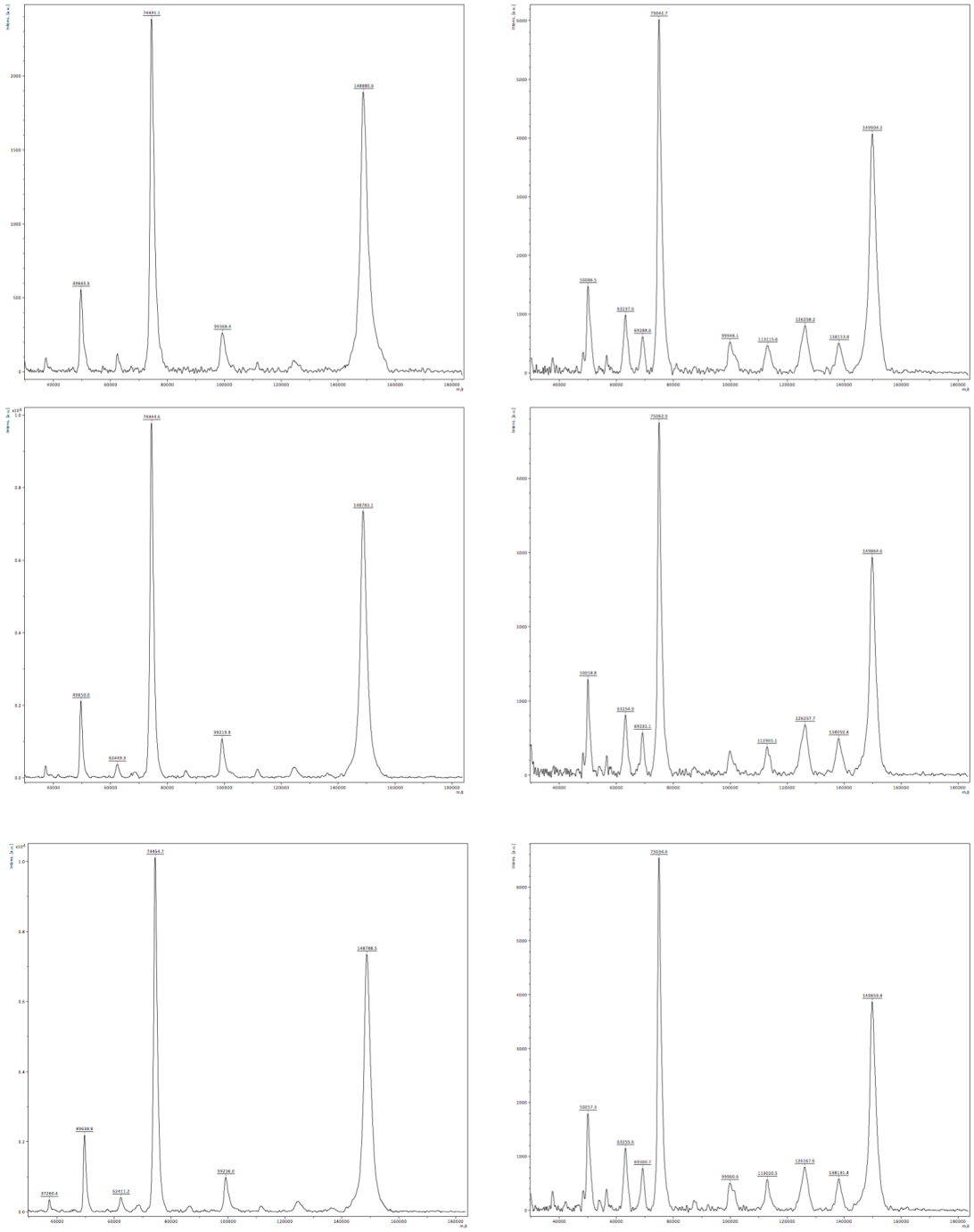

Figure A.3.1 MALDI-ToF MS of HuE71-1 WT
MALDI-ToF MS of unmodified antibody (left) and DFO-modified antibody (right) in triplicate. Mass and chelate number values outlined in Figure A.3.7.

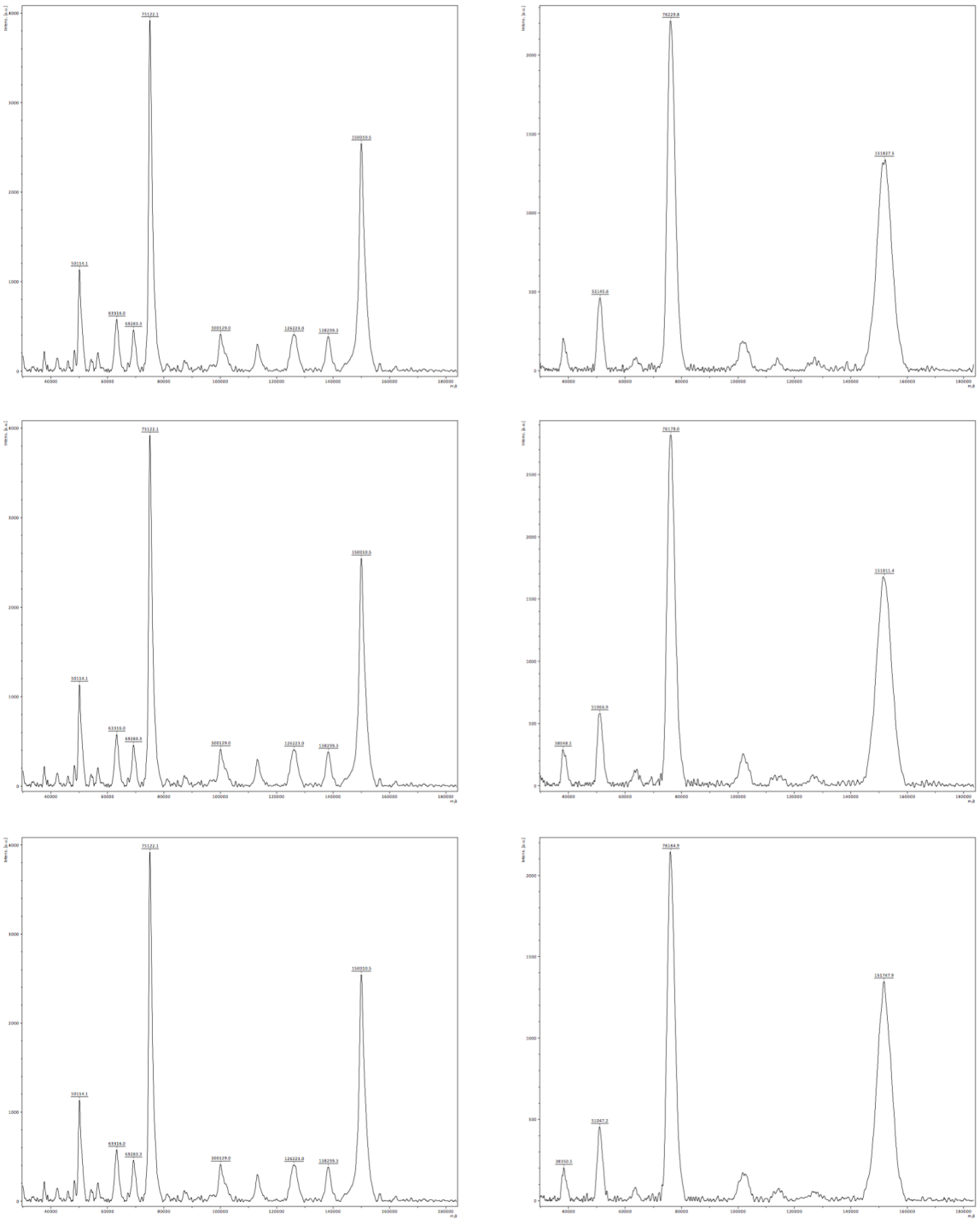

Figure A.3.2 MALDI-ToF MS of HuE71-1 MAGE
MALDI-ToF MS of unmodified antibody (left) and DFO-modified antibody (right) in triplicate. Mass and chelate number values outlined in Figure A.3.7.

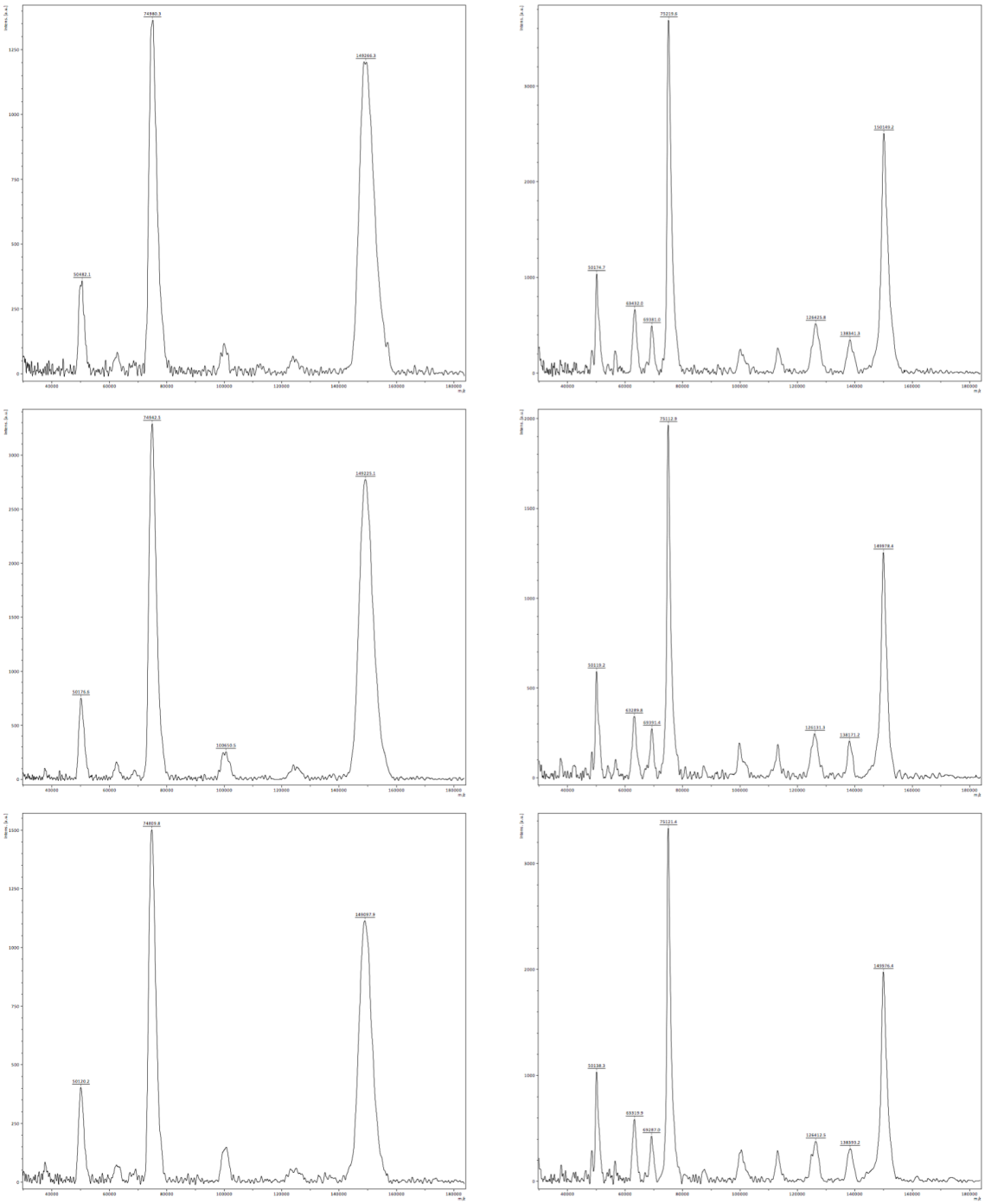

Figure A.3.3 MALDI-ToF MS of HuE71-1 Aglyco
MALDI-ToF MS of unmodified antibody (left) and DFO-modified antibody (right) in triplicate. Mass and chelate number values outlined in Figure A.3.7.

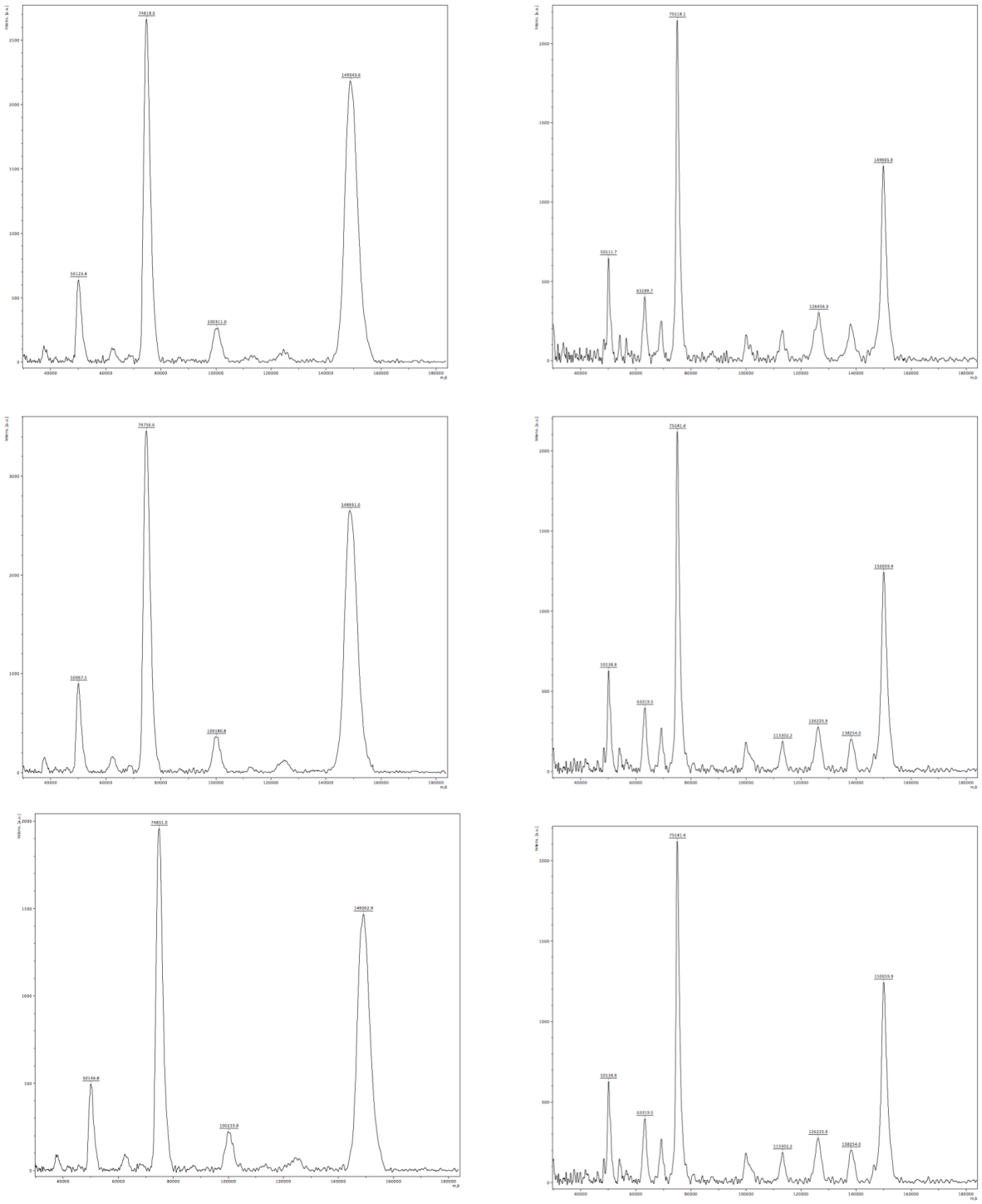

Figure A.3.4 MALDI-ToF MS of HuE71-4 WT
MALDI-ToF MS of unmodified antibody (left) and DFO-modified antibody (right) in triplicate. Mass and chelate number values outlined in Figure A.3.7.

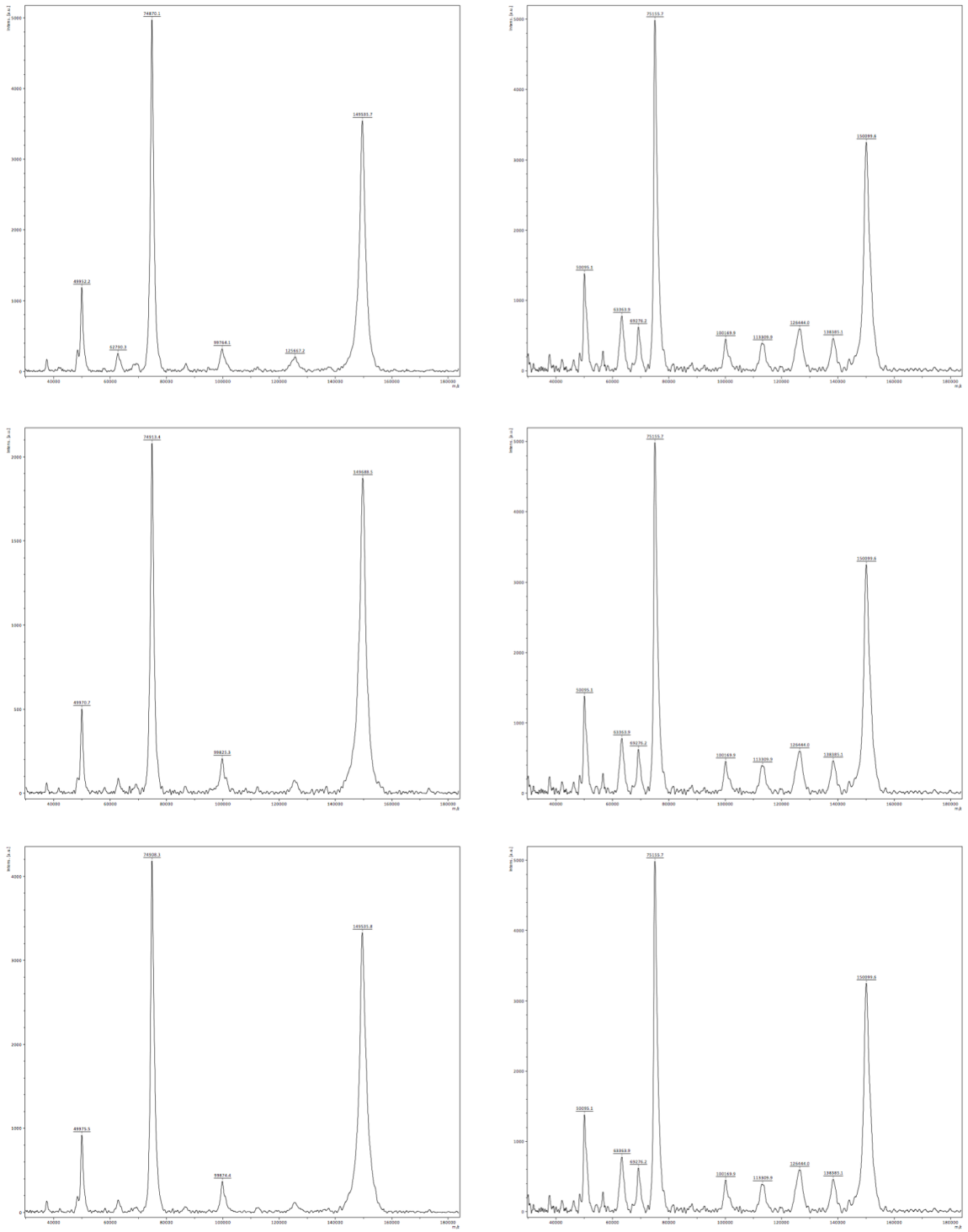

Figure A.3.5 MALDI-ToF MS of HuE71-4 Mutant
MALDI-ToF MS of unmodified antibody (left) and DFO-modified antibody (right) in triplicate. Mass and chelate number values outlined in Figure A.3.7.

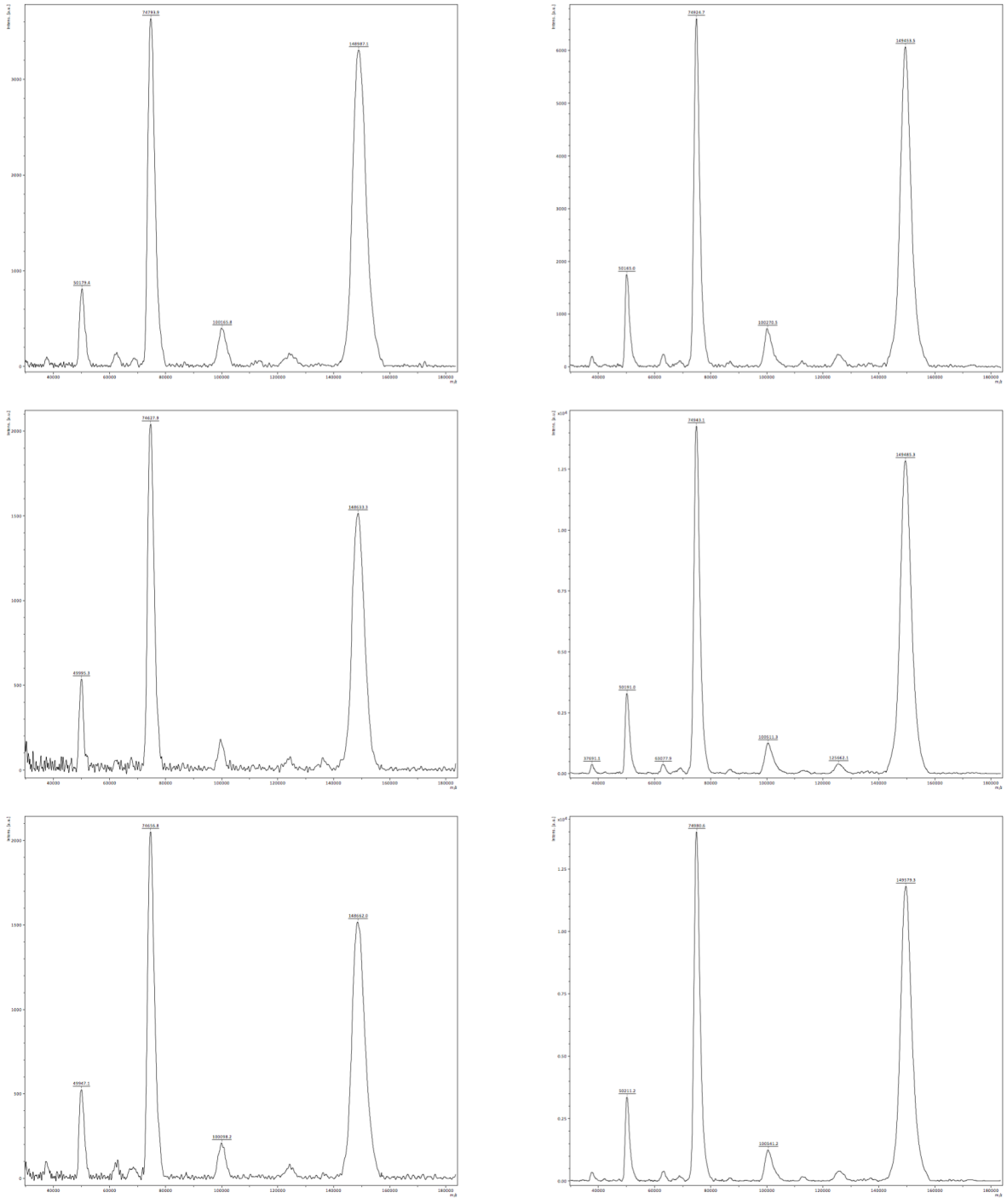

Figure A.3.6 MALDI-ToF MS of HuCtrl-4 WT
MALDI-ToF MS of unmodified antibody (left) and DFO-modified antibody (right) in triplicate. Mass and chelate number values outlined in Figure A.3.7.

	HuE71-1 WT	DFO-HuE71-1 WT	HuE71-1 MAGE	DFO-HuE71-1 MAGE	HuE71-1 Aglyco	DFO-HuE71-1 Aglyco
Mass 1 (Da)	148880.6	149904.3	150010.5	151747.9	149266.3	150049.2
Mass 2 (Da)	148783.1	149859.4	149978.4	151811.4	149225.1	149978.4
Mass 3 (Da)	148788.5	149864.6	150011.5	151827.5	149097.9	149976.4
Average	149876.1	148817.4	150000.1	151795.6	149196.4	150001.3
Standard Dev	54.80	24.56	18.83	42.09	87.78	41.47
Chelate Number		1.41		2.38		1.07
	HuE71-4 WT	**DFO-HuE71-4 WT**	**HuE71-4 Mutant**	**DFO-HuE71-4 Mutant**	**HuCtrl-4 WT**	**DFO-HuCtrl-4 WT**
Mass 1 (Da)	149043.6	150059.9	149535.7	150099.6	148687.1	149453.5
Mass 2 (Da)	148931	149949.7	149535.8	150070	148633.3	149485.3
Mass 3 (Da)	149002.9	149905.9	149688.5	150019.1	148662	149579.3
Average	148992.5	149971.8	149586.7	150062.9	148660.8	149506.0
Standard Dev	57.02	79.35	88.19	40.72	26.92	65.41
Chelate Number		1.30		0.63		1.12

Figure A.3.7. Table of MALDI-ToF MS derived chelate numbers.

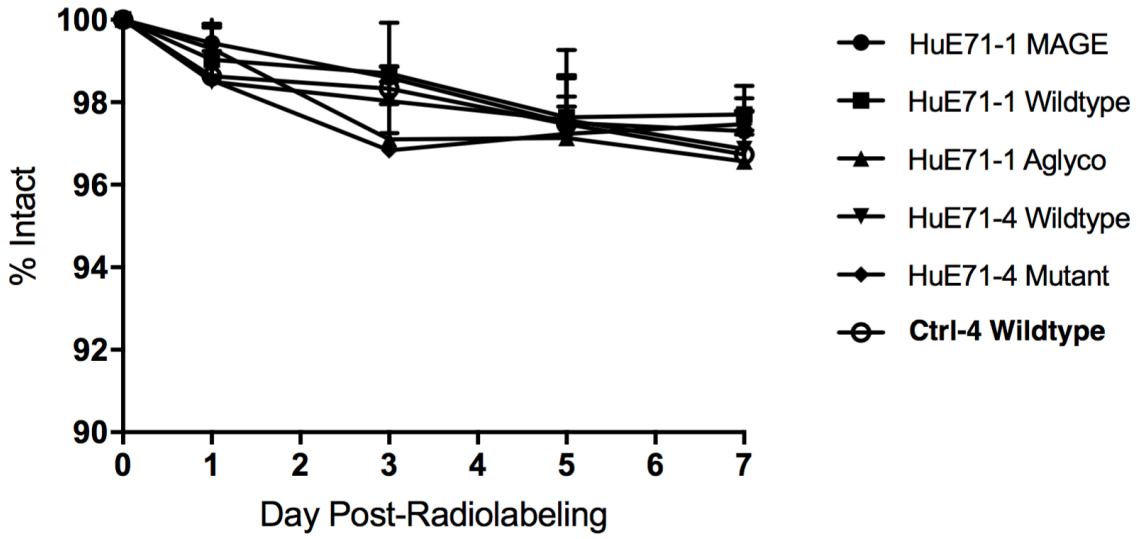

Figure A.3.8. Serum stability of L1CAM targeted ^{89}Zr-radioimmunoconjugates.
Serum stability of the radioimmunoconjugates was assessed by incubating 100 μL of purified reaction mixture in 900 μL of human male AB+ serum at 37 degrees Celsius. Aliquots of radioimmunoconjugates (in triplicate) were assessed via radio-ITLC at the time points listed above.

	HuE71-1 MAGE		HuE71-1 MAGE Blocked		HuE71-1 WT		HuE71-1 WT Blocked		HuE71-1 Aglyco		HuE71-1 Aglyco Blocked	
	%ID/g	SEM	%ID/g	SEM	%ID/g	SEM	%ID/g	SEM	%ID/g	SEM	%ID/g	SEM
Blood	4.67	0.85	9.84	0.84	5.52	0.99	9.64	1.39	7.94	1.19	9.51	0.39
Tumor	16.15	0.85	5.87	0.76	19.68	1.00	6.82	0.81	32.03	2.99	10.59	1.52
Heart	4.60	0.77	9.55	0.53	4.56	0.44	7.80	1.57	3.76	0.59	6.25	1.33
Lungs	4.81	1.16	7.95	1.00	5.63	0.97	6.87	1.20	4.86	1.13	5.10	1.08
Liver	7.09	0.69	9.24	0.64	11.06	1.00	13.65	1.16	6.22	1.22	9.76	0.37
Spleen	7.13	1.12	9.08	0.84	6.15	1.93	7.52	1.32	4.37	0.58	4.49	0.24
Stomach	2.52	0.51	3.68	0.77	3.66	0.29	3.96	0.88	3.56	0.51	3.78	0.40
Large Bowel	2.20	0.21	2.37	0.51	2.06	0.14	2.77	0.93	2.56	0.31	3.31	0.30
Small Bowel	3.05	0.85	4.02	1.30	3.40	0.56	2.09	0.95	3.63	0.31	4.23	1.45
Pancreas	4.63	0.84	4.47	0.33	3.92	0.77	4.09	1.21	4.28	0.69	4.73	1.81
Ovary	3.36	0.50	5.72	2.14	4.78	0.61	5.07	1.71	3.49	0.90	5.97	2.30
Kidney	6.17	1.00	9.97	0.49	5.92	0.80	7.23	1.55	4.62	0.70	6.12	0.79
Bone	2.85	0.99	3.69	0.50	2.87	0.17	3.06	0.63	2.79	0.85	3.64	1.42
Muscle	3.78	0.60	4.26	0.97	4.14	0.48	4.97	0.75	4.87	0.85	6.31	0.98
Lymph	17.16	0.41	18.63	0.95	16.86	1.39	19.21	0.66	5.60	0.49	5.71	1.65
Skin	1.49	0.38	3.77	1.52	1.79	0.57	4.14	0.62	2.66	0.78	3.87	0.45
Tail	1.57	0.42	5.20	0.50	2.54	1.09	4.22	0.82	2.39	0.75	4.21	1.08

Figure A.3.9. ***Ex vivo*** **Biodistribution values of IgG1 antibodies 96h post-injection.**

	HuE71-4 WT		HuE71-4 WT Blocked		HuE71-4 Mutant		HuE71-4 Mutant Blocked		HuCtrl-4 WT	
	%ID/g	SEM	%ID/g	SEM	%ID/g	SEM	%ID/g	SEM	%ID/g	SEM
Blood	3.53	0.63	5.88	1.24	5.86	0.18	7.35	0.15	7.32	0.49
Tumor	27.30	1.55	10.65	0.47	16.90	1.22	9.04	1.42	6.03	0.87
Heart	2.76	0.25	3.37	1.03	5.34	0.79	7.90	0.72	7.05	0.93
Lungs	3.65	0.93	4.76	0.66	5.39	0.46	6.37	0.92	5.86	0.45
Liver	3.85	0.52	5.25	0.50	13.20	0.70	13.97	1.04	11.05	0.50
Spleen	5.44	1.28	5.76	0.96	9.23	1.27	9.58	0.48	9.63	1.54
Stomach	4.58	0.28	5.01	1.07	3.81	1.49	4.35	0.49	5.01	0.54
Large Bowel	2.39	0.62	2.64	0.36	3.95	1.05	3.84	0.49	3.52	0.28
Small Bowel	2.26	0.44	2.75	0.46	3.64	0.67	3.46	1.45	3.10	0.65
Pancreas	3.11	0.58	3.46	0.36	5.73	0.22	5.42	0.71	3.26	0.50
Ovary	3.31	0.88	3.80	0.31	3.95	0.78	3.30	0.62	2.99	1.18
Kidney	12.06	1.24	14.96	0.94	5.83	0.54	6.04	0.27	17.91	2.46
Bone	1.48	0.30	1.80	0.53	2.72	0.56	3.84	1.34	3.71	1.35
Muscle	3.53	0.24	4.15	0.62	2.67	1.21	3.67	1.23	4.03	0.67
Lymph	3.99	0.97	3.15	1.03	2.95	0.44	4.23	0.56	4.90	0.41
Skin	2.98	0.87	2.80	0.31	3.70	0.98	3.22	1.11	3.44	0.79
Tail	1.50	0.15	1.88	0.18	3.30	0.82	4.57	1.08	2.89	0.79

Figure A.3.10. ***Ex vivo*** **Biodistribution values of IgG4 antibodies 96h post-injection.**

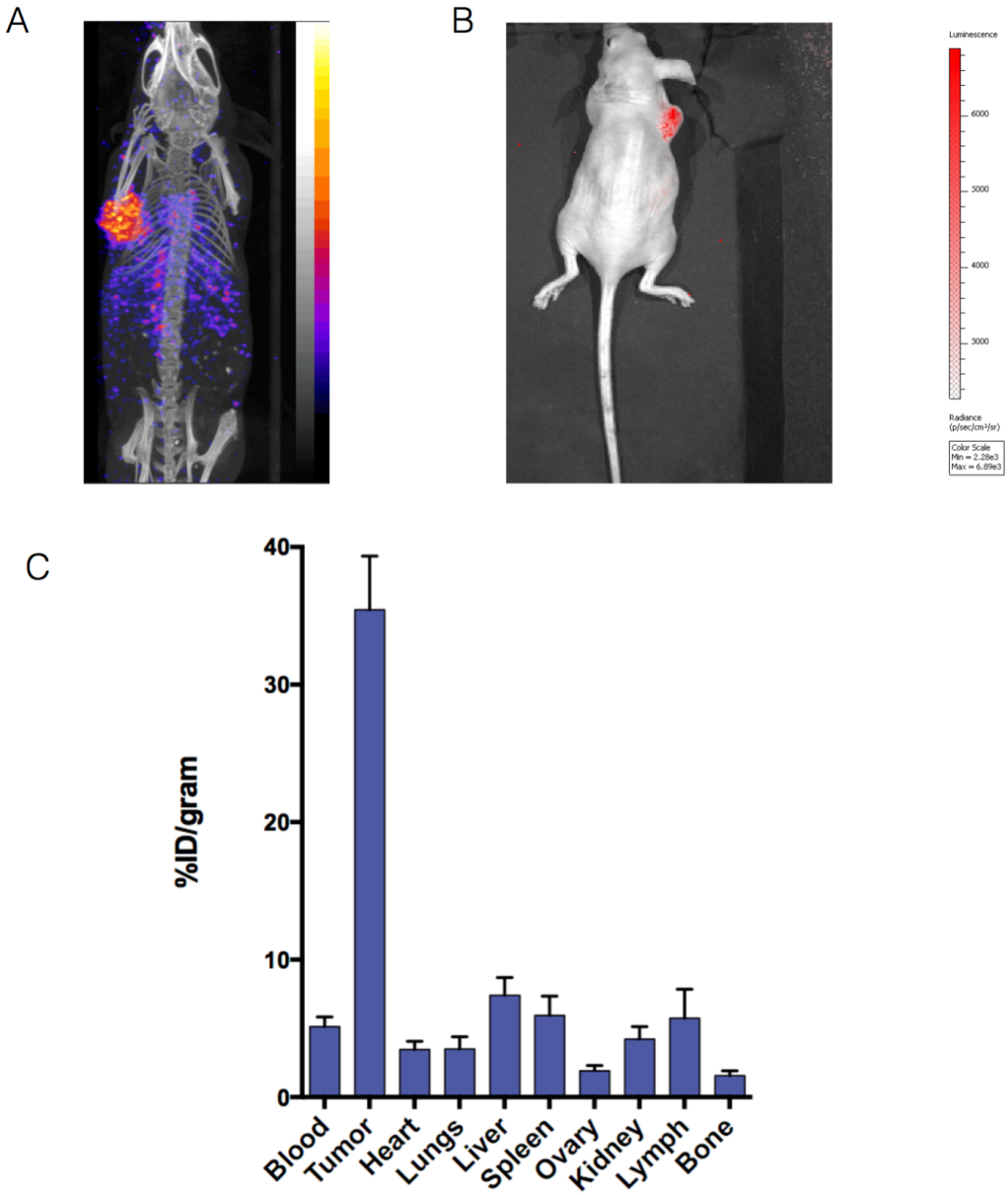

Figure A.3.11. ^{177}Lu-HuE71-1 Aglyco imaging and e*x vivo* biodistribution.
(A) SPECT-CT image of athymic nude SKOV-3 tumor bearing mouse 168h post-injection of ^{177}Lu-HuE71-1 Aglyco (858 □ Ci in 150 □ L of PBS), (B) Cerenkov image of athymic nude SKOV-3 tumor bearing mouse 168h post-injection of ^{177}Lu-HuE71-1 Aglyco (858 □ Ci in 150 □ L of PBS), and (C) 168h *ex vivo* biodistribution of athymic nude SKOV-3 tumor bearing mouse 168h post-injection of ^{177}Lu-HuE71-1 Aglyco (18-26 □ Ci in 150 □ L of PBS, n=4).

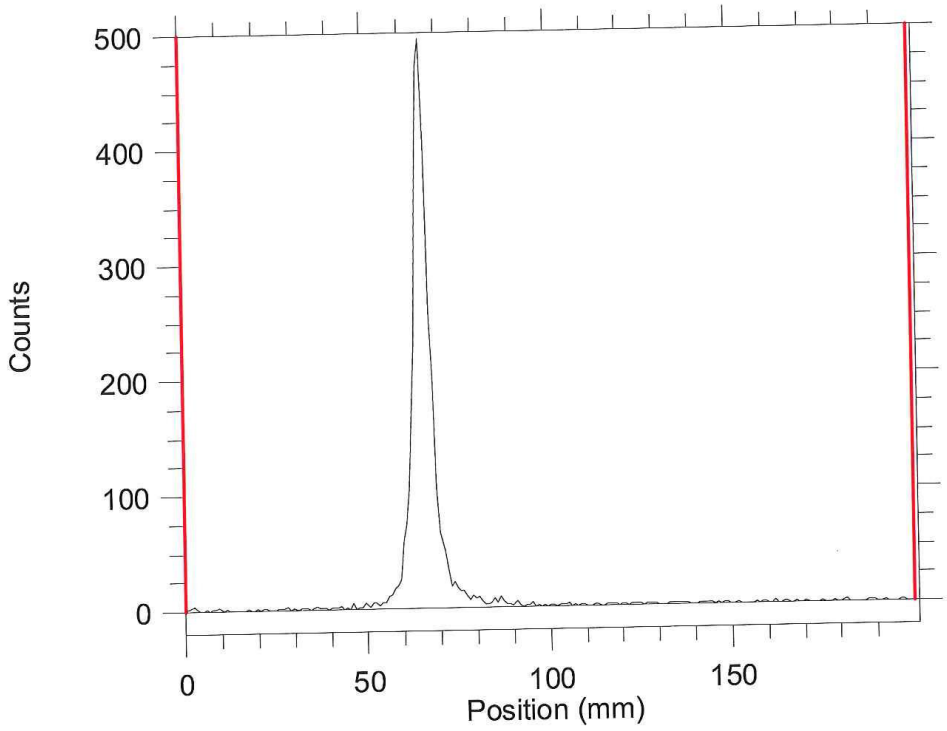

Figure A.3.12 Radio-ITLC of ^{89}Zr-DFO-HuE71-1 WT purified reaction.

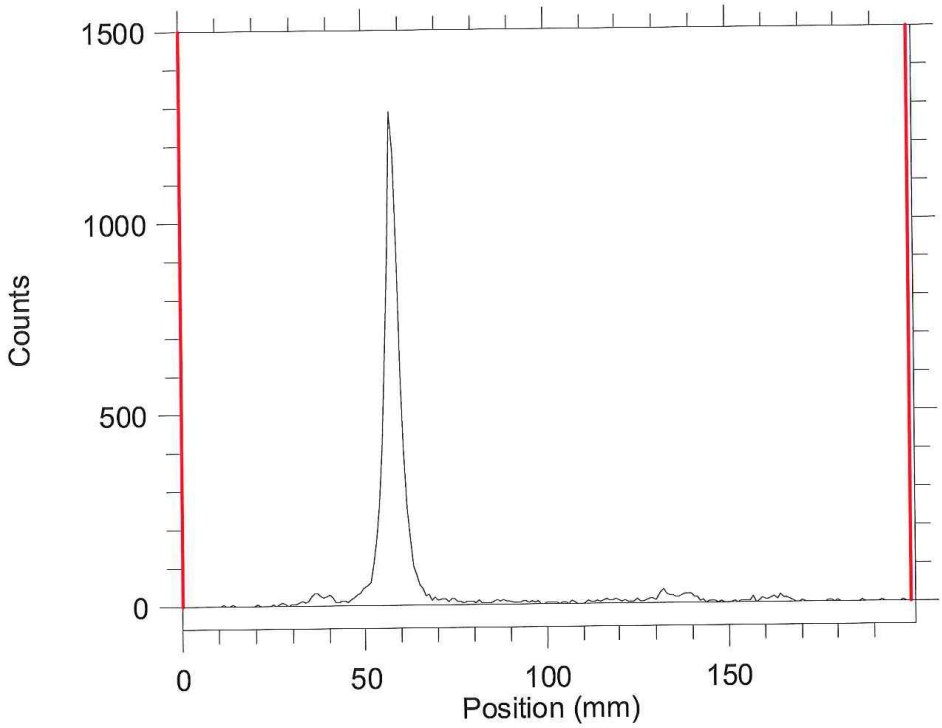

Figure A.3.13 Radio-ITLC of ^{89}Zr-DFO-HuE71-1 MAGE purified reaction.

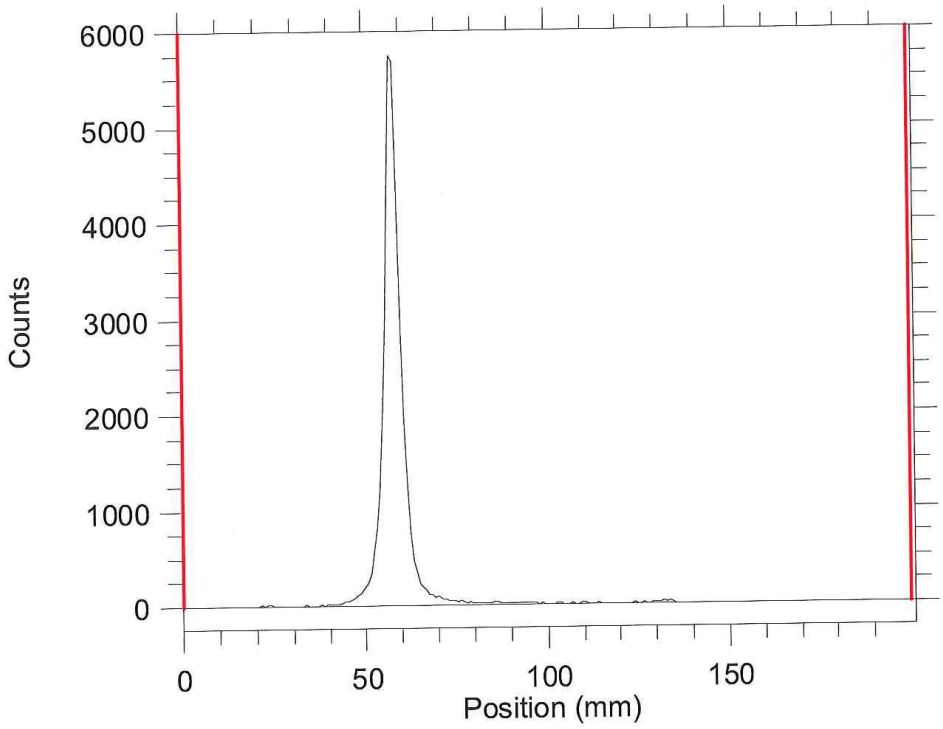

Figure A.3.14 Radio-ITLC of ^{89}Zr-DFO-HuE71-1 Aglyco purified reaction.

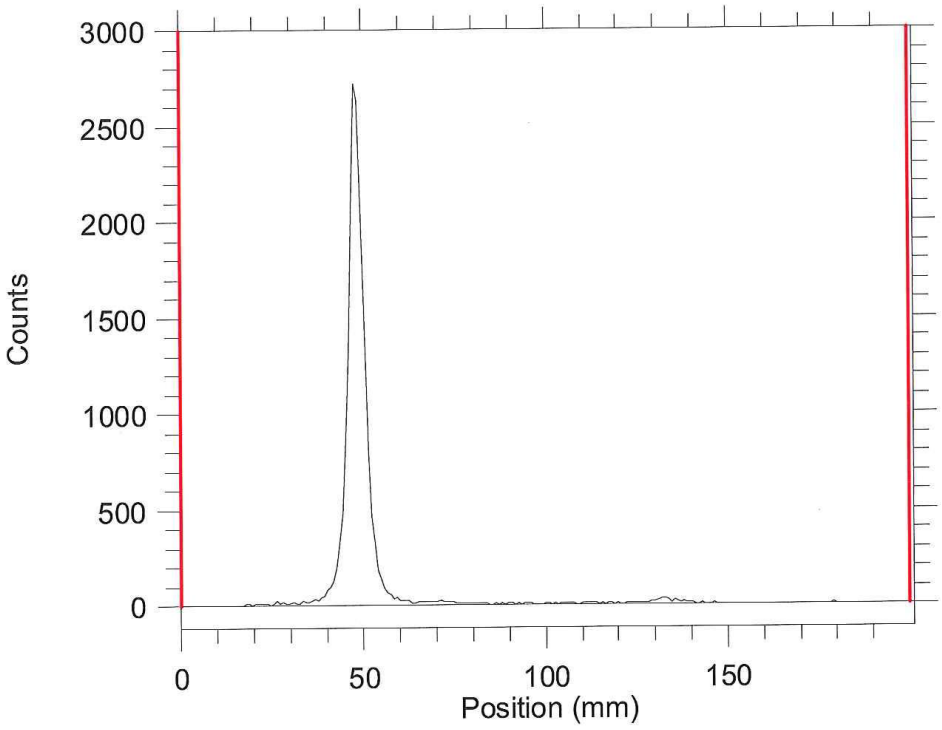

Figure A.3.15 Radio-ITLC of ^{89}Zr-DFO-HuE71-4 WT purified reaction.

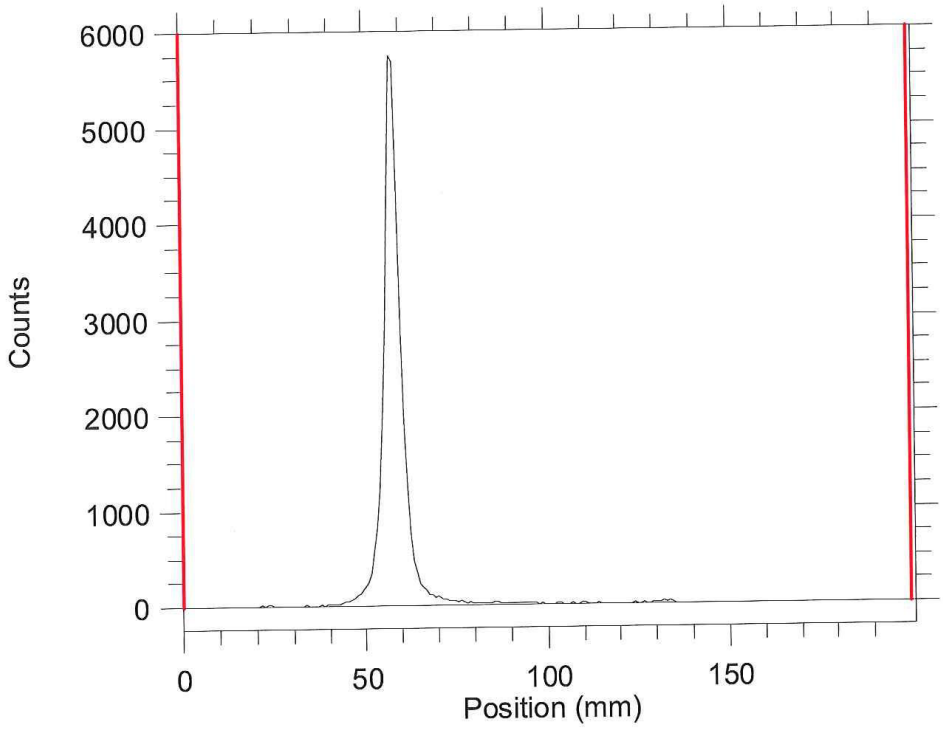

Figure A.3.16 Radio-ITLC of ^{89}Zr-DFO-HuE71-4 Mutant purified reaction.

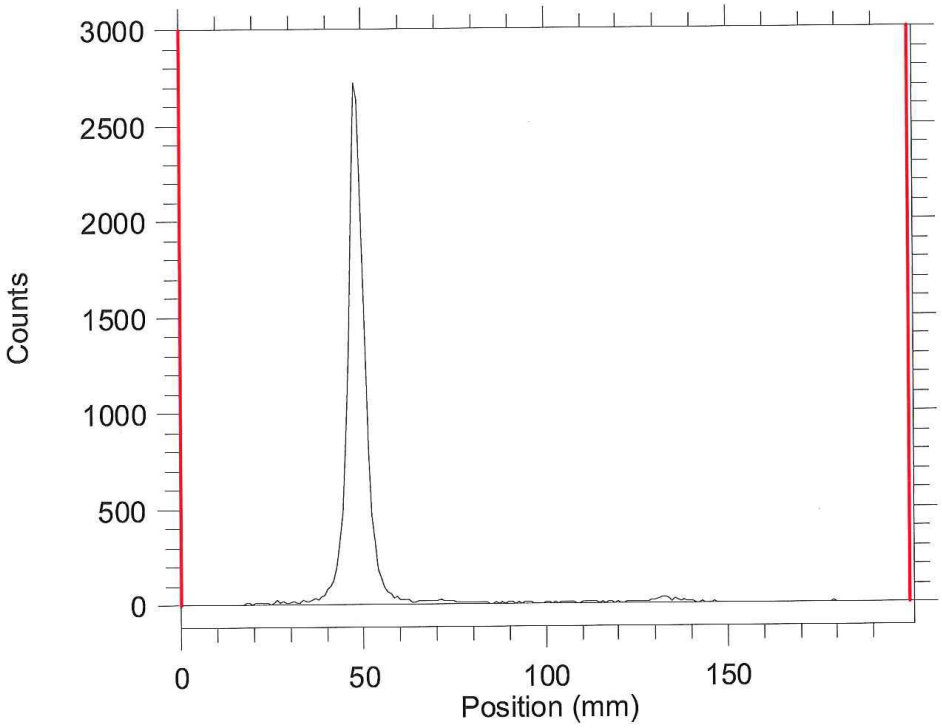

Figure A.3.17 Radio-ITLC of ^{89}Zr-DFO-HuCtrl-4 WT purified reaction.

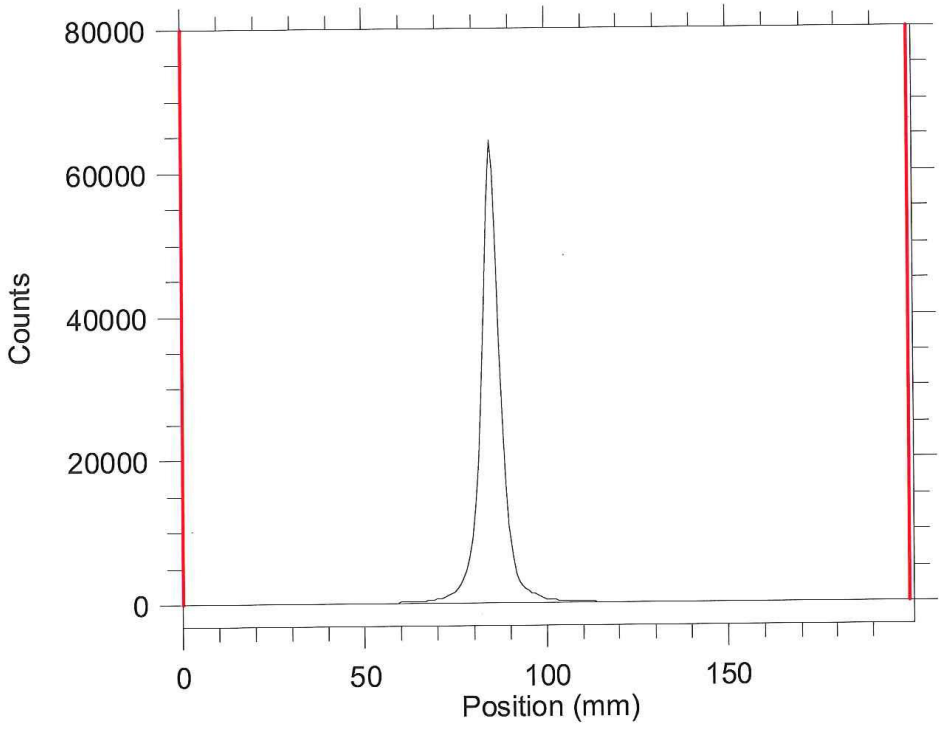

Figure A.3.18 Radio-ITLC of ^{177}Zr-DOTA-HuE71-1 Aglyco purified reaction.

References

1. Siegel RL, Miller KD, Jemal A. Cancer statistics, 2015. *CA Cancer J Clin.* 2015;65(1):5-29.
2. Gupta D, Lis CG. Role of CA125 in predicting ovarian cancer survival - a review of the epidemiological literature. *J Ovarian Res.* 2009;2:13.
3. Haggerty AF, Hagemann AR, Chu C, Siegelman ES, Rubin SC. Correlation of pelvic magnetic resonance imaging diagnosis with pathology for indeterminate adnexal masses. *International journal of gynecological cancer : official journal of the International Gynecological Cancer Society.* 2014;24(7):1215-1221.
4. Adusumilli S, Hussain HK, Caoili EM, et al. MRI of sonographically indeterminate adnexal masses. *AJR American journal of roentgenology.* 2006;187(3):732-740.
5. Shahbazi-Gahrouei D, Abdolahi M. Superparamagnetic iron oxide-C595: Potential MR imaging contrast agents for ovarian cancer detection. *Journal of medical physics / Association of Medical Physicists of India.* 2013;38(4):198-204.
6. Quan G, Du X, Huo T, et al. Targeted molecular imaging of antigen OC183B2 in ovarian cancers using MR molecular probes. *Academic radiology.* 2010;17(12):1468-1476.
7. Schwenzer NF, Schmidt H, Gatidis S, et al. Measurement of apparent diffusion coefficient with simultaneous MR/positron emission tomography in patients with peritoneal carcinomatosis: comparison with 18F-FDG-PET. *Journal of magnetic resonance imaging : JMRI.* 2014;40(5):1121-1128.
8. Li X, Hu JL, Zhu LM, et al. The clinical value of dynamic contrast-enhanced MRI in differential diagnosis of malignant and benign ovarian lesions. *Tumour biology : the journal of the International Society for Oncodevelopmental Biology and Medicine.* 2015;36(7):5515-5522.

9. Esseridou A, Di Leo G, Sconfienza LM, et al. In vivo detection of choline in ovarian tumors using 3D magnetic resonance spectroscopy. *Investigative radiology.* 2011;46(6):377-382.

10. Sala E, Kataoka MY, Priest AN, et al. Advanced ovarian cancer: multiparametric MR imaging demonstrates response- and metastasis-specific effects. *Radiology.* 2012;263(1):149-159.

11. Thrall MM, DeLoia JA, Gallion H, Avril N. Clinical use of combined positron emission tomography and computed tomography (FDG-PET/CT) in recurrent ovarian cancer. *Gynecol Oncol.* 2007;105(1):17-22.

12. Zimny M, Siggelkow W, Schroder W, et al. 2-[Fluorine-18]-fluoro-2-deoxy-d-glucose positron emission tomography in the diagnosis of recurrent ovarian cancer. *Gynecol Oncol.* 2001;83(2):310-315.

13. Kyriazi S, Kaye SB, deSouza NM. Imaging ovarian cancer and peritoneal metastases--current and emerging techniques. *Nature reviews Clinical oncology.* 2010;7(7):381-393.

14. Caobelli F, Alongi P, Evangelista L, et al. Predictive value of F-FDG PET/CT in restaging patients affected by ovarian carcinoma: a multicentre study. *Eur J Nucl Med Mol Imaging.* 2015.

15. Sala E, Kataoka M, Pandit-Taskar N, et al. Recurrent ovarian cancer: use of contrast-enhanced CT and PET/CT to accurately localize tumor recurrence and to predict patients' survival. *Radiology.* 2010;257(1):125-134.

16. Vallius T, Peter A, Auranen A, et al. F-FDG-PET/CT can identify histopathological non-responders to platinum-based neoadjuvant chemotherapy in advanced epithelial ovarian cancer. *Gynecol Oncol.* 2015.

17. Gungor H, Saleem A, Babar S, et al. Dose-finding quantitative FDG PET imaging study with the oral pan-AKT inhibitor GSK2141795 in patients with gynecological malignancies. *Journal of nuclear medicine : official publication, Society of Nuclear Medicine.* 2015.

18. Siegel BA, Dehdashti F, Mutch DG, et al. Evaluation of 111In-DTPA-folate as a receptor-targeted diagnostic agent for ovarian cancer: initial clinical results. *Journal of nuclear medicine : official publication, Society of Nuclear Medicine.* 2003;44(5):700-707.

19. Morris RT, Joyrich RN, Naumann RW, et al. Phase II study of treatment of advanced ovarian cancer with folate-receptor-targeted therapeutic (vintafolide) and companion SPECT-based imaging agent (99mTc-etarfolatide). *Annals of oncology : official journal of the European Society for Medical Oncology / ESMO.* 2014;25(4):852-858.

20. van Kruchten M, de Vries EF, Arts HJ, et al. Assessment of estrogen receptor expression in epithelial ovarian cancer patients using 16alpha-18F-fluoro-17beta-estradiol PET/CT. *Journal of nuclear medicine : official publication, Society of Nuclear Medicine.* 2015;56(1):50-55.

21. Lamberts TE, Menke-van der Houven van Oordt CW, Ter Weele EJ, et al. ImmunoPET with anti-mesothelin antibody in patients with pancreatic and ovarian cancer before anti-mesothelin antibody-drug conjugate treatment. *Clin Cancer Res.* 2015.

22. Sharma SK, Zeglis B, Sevak K, Lewis J, Wuest F. Zr-89 immuno-PET of epithelial ovarian cancer. *Nucl Med Biol.* 2014;41(7):638-639.

23. Ocak M, Gillman AG, Bresee J, et al. Folate receptor-targeted multimodality imaging of ovarian cancer in a novel syngeneic mouse model. *Molecular pharmaceutics.* 2015;12(2):542-553.

24. Liu TW, Stewart JM, Macdonald TD, et al. Biologically-targeted detection of primary and micro-metastatic ovarian cancer. *Theranostics.* 2013;3(6):420-427.

25. Li F, Zhang Z, Cheng T, et al. SPECT imaging of interleukin-6 receptor in ovarian tumor xenografts with a novel radiotracer of Tc-HYNIC-Aca-LSLITRL. *Amino acids.* 2015.

26. Zhang J, Zhao X, Wang S, et al. Monitoring therapeutic response of human ovarian cancer to trastuzumab by SPECT imaging with (99m)Tc-peptide-Z(HER2:342). *Nuclear medicine and biology.* 2015;42(6):541-546.

27. Niu G, Li Z, Cao Q, Chen X. Monitoring therapeutic response of human ovarian cancer to 17-DMAG by noninvasive PET imaging with (64)Cu-DOTA-trastuzumab. *European journal of nuclear medicine and molecular imaging.* 2009;36(9):1510-1519.

28. Nagengast WB, de Korte MA, Oude Munnink TH, et al. 89Zr-bevacizumab PET of early antiangiogenic tumor response to treatment with HSP90 inhibitor NVP-AUY922. *Journal of nuclear medicine : official publication, Society of Nuclear Medicine.* 2010;51(5):761-767.

29. Chi C, Du Y, Ye J, et al. Intraoperative imaging-guided cancer surgery: from current fluorescence molecular imaging methods to future multi-modality imaging technology. *Theranostics.* 2014;4(11):1072-1084.

30. van Dam GM, Themelis G, Crane LM, et al. Intraoperative tumor-specific fluorescence imaging in ovarian cancer by folate receptor-alpha targeting: first in-human results. *Nature medicine.* 2011;17(10):1315-1319.

31. Tummers QR, Hoogstins CE, Peters AA, et al. The Value of Intraoperative Near-Infrared Fluorescence Imaging Based on Enhanced Permeability and Retention of Indocyanine Green: Feasibility and False-Positives in Ovarian Cancer. *PloS one.* 2015;10(6):e0129766.

32. Quirijn R. Tummers CEH, Adam F. Cohen, Cornelis J. van de Velde, Philip S. Low, Gerrit-Jan Liefers, Katja N. Gaarenstroom, Jacobus Burggraaf, Alexander L. Vahrmeijer. Intraoperative fluorescence imaging of folate receptor alpha positive ovarian and breast cancer using the tumor specific agent EC17. *World Molecular Imaging Congress.* Vol 2015 Sept 2-52015:Abstract ID 2233311.

33. Terwisscha van Scheltinga AG, van Dam GM, Nagengast WB, et al. Intraoperative near-infrared fluorescence tumor imaging with vascular endothelial growth factor and human epidermal growth factor receptor 2 targeting antibodies. *Journal of nuclear medicine : official publication, Society of Nuclear Medicine.* 2011;52(11):1778-1785.

34. Lee H, Kim J, Kim H, Kim Y, Choi Y. A folate receptor-specific activatable probe for near-infrared fluorescence imaging of ovarian cancer. *Chemical communications.* 2014;50(56):7507-7510.

35. Mallidi S, Luke GP, Emelianov S. Photoacoustic imaging in cancer detection, diagnosis, and treatment guidance. *Trends in biotechnology.* 2011;29(5):213-221.

36. Aguirre A, Ardeshirpour Y, Sanders MM, Brewer M, Zhu Q. Potential role of coregistered photoacoustic and ultrasound imaging in ovarian cancer detection and characterization. *Translational oncology.* 2011;4(1):29-37.

37. Alqasemi U, Li H, Yuan G, Kumavor P, Zanganeh S, Zhu Q. Interlaced photoacoustic and ultrasound imaging system with real-time coregistration for ovarian tissue characterization. *Journal of biomedical optics.* 2014;19(7):76020.

38. Salehi HS, Wang T, Kumavor PD, Li H, Zhu Q. Design of miniaturized illumination for transvaginal co-registered photoacoustic and ultrasound imaging. *Biomedical optics express.* 2014;5(9):3074-3079.

39. Jokerst JV, Cole AJ, Van de Sompel D, Gambhir SS. Gold nanorods for ovarian cancer detection with photoacoustic imaging and resection guidance via Raman imaging in living mice. *ACS nano.* 2012;6(11):10366-10377.

40. Willmann JK, Kimura RH, Deshpande N, Lutz AM, Cochran JR, Gambhir SS. Targeted contrast-enhanced ultrasound imaging of tumor angiogenesis with contrast microbubbles conjugated to integrin-binding knottin peptides. *J Nucl Med.* 2010;51(3):433-440.

41. Lutz AM, Bachawal SV, Drescher CW, Pysz MA, Willmann JK, Gambhir SS. Ultrasound molecular imaging in a human CD276 expression-modulated murine ovarian cancer model. *Clin Cancer Res.* 2014;20(5):1313-1322.

42. Partovi S, Kohan A, Rubbert C, et al. Clinical oncologic applications of PET/MRI: a new horizon. *American journal of nuclear medicine and molecular imaging.* 2014;4(2):202-212.

43. Siegel RL, Miller KD, Jemal A. Cancer Statistics, 2017. *CA: a cancer journal for clinicians.* 2017;67(1):7-30.

44. Matias-Guiu X, Davidson B. Prognostic biomarkers in endometrial and ovarian carcinoma. *Virchows Archiv : an international journal of pathology.* 2014;464(3):315-331.

45. Reid BM, Permuth JB, Sellers TA. Epidemiology of ovarian cancer: a review. *Cancer Biol Med.* 2017;14(1):9-32.

46. Hennessy BT, Coleman RL, Markman M. Ovarian cancer. *Lancet.* 2009;374(9698):1371-1382.

47. Canis M, Botchorishvili R, Manhes H, et al. Management of adnexal masses: role and risk of laparoscopy. *Seminars in surgical oncology.* 2000;19(1):28-35.

48. van Nagell JR, Jr., Miller RW. Evaluation and Management of Ultrasonographically Detected Ovarian Tumors in Asymptomatic Women. *Obstetrics and gynecology.* 2016;127(5):848-858.

49. Timmerman D, Van Calster B, Testa A, et al. Predicting the risk of malignancy in adnexal masses based on the Simple Rules from the International Ovarian Tumor Analysis group. *American journal of obstetrics and gynecology.* 2016;214(4):424-437.

50. Sainz de la Cuesta R, Goff BA, Fuller AF, Jr., Nikrui N, Eichhorn JH, Rice LW. Prognostic importance of intraoperative rupture of malignant ovarian epithelial neoplasms. *Obstetrics and gynecology.* 1994;84(1):1-7.

51. Buys SS, Partridge E, Greene MH, et al. Ovarian cancer screening in the Prostate, Lung, Colorectal and Ovarian (PLCO) cancer screening trial: findings from the initial screen of a randomized trial. *American journal of obstetrics and gynecology.* 2005;193(5):1630-1639.

52. Metcalfe KA, Lynch HT, Ghadirian P, et al. The risk of ovarian cancer after breast cancer in BRCA1 and BRCA2 carriers. *Gynecologic oncology.* 2005;96(1):222-226.

53. van de Watering FC, Rijpkema M, Perk L, Brinkmann U, Oyen WJ, Boerman OC. Zirconium-89 labeled antibodies: a new tool for molecular imaging in cancer patients. *BioMed research international.* 2014;2014:203601.

54. Vidarsson G, Dekkers G, Rispens T. IgG subclasses and allotypes: from structure to effector functions. *Front Immunol.* 2014;5:520.

55. Verel I, Visser GW, Boellaard R, Stigter-van Walsum M, Snow GB, van Dongen GA. 89Zr immuno-PET: comprehensive procedures for the production of 89Zr-labeled monoclonal antibodies. *Journal of nuclear medicine : official publication, Society of Nuclear Medicine.* 2003;44(8):1271-1281.

56. Wadas TJ, Wong EH, Weisman GR, Anderson CJ. Coordinating radiometals of copper, gallium, indium, yttrium, and zirconium for PET and SPECT imaging of disease. *Chemical reviews.* 2010;110(5):2858-2902.

57. Holland JP, Divilov V, Bander NH, Smith-Jones PM, Larson SM, Lewis JS. 89Zr-DFO-J591 for immunoPET of prostate-specific membrane antigen expression in vivo. *Journal of nuclear medicine : official publication, Society of Nuclear Medicine.* 2010;51(8):1293-1300.

58. Abou DS, Ku T, Smith-Jones PM. In vivo biodistribution and accumulation of 89Zr in mice. *Nuclear medicine and biology.* 2011;38(5):675-681.

59. Meijs WE, Herscheid JD, Haisma HJ, Pinedo HM. Evaluation of desferal as a bifunctional chelating agent for labeling antibodies with Zr-89. *International journal of radiation applications and instrumentation Part A, Applied radiation and isotopes.* 1992;43(12):1443-1447.

60. Chopra A. 89Zr-Labeled p-isothiocyanatobenzyl-desferrioxamine B (Df-Bz-NCS)-conjugated panitumumab, a fully human monoclonal antibody directed against the extracellular domain III of the epidermal growth factor receptor. *Molecular Imaging and Contrast Agent Database (MICAD)*. Bethesda (MD)2004.

61. Guerard F, Lee YS, Tripier R, Szajek LP, Deschamps JR, Brechbiel MW. Investigation of Zr(IV) and 89Zr(IV) complexation with hydroxamates: progress towards designing a better chelator than desferrioxamine B for immuno-PET imaging. *Chemical communications.* 2013;49(10):1002-1004.

62. Perk LR, Vosjan MJ, Visser GW, et al. p-Isothiocyanatobenzyl-desferrioxamine: a new bifunctional chelate for facile radiolabeling of monoclonal antibodies with zirconium-89 for immuno-PET imaging. *European journal of nuclear medicine and molecular imaging.* 2010;37(2):250-259.

63. Tinianow JN, Gill HS, Ogasawara A, et al. Site-specifically 89Zr-labeled monoclonal antibodies for ImmunoPET. *Nuclear medicine and biology.* 2010;37(3):289-297.

64. Vugts DJ, Vervoort A, Stigter-van Walsum M, et al. Synthesis of phosphine and antibody-azide probes for in vivo Staudinger ligation in a pretargeted imaging and therapy approach. *Bioconjugate chemistry.* 2011;22(10):2072-2081.

65. Zeglis BM, Mohindra P, Weissmann GI, et al. Modular strategy for the construction of radiometalated antibodies for positron emission tomography based on inverse electron demand Diels-Alder click chemistry. *Bioconjugate chemistry.* 2011;22(10):2048-2059.

66. Zeglis BM, Davis CB, Aggeler R, et al. Enzyme-mediated methodology for the site-specific radiolabeling of antibodies based on catalyst-free click chemistry. *Bioconjugate chemistry.* 2013;24(6):1057-1067.

67. Gross ME, Shazer RL, Agus DB. Targeting the HER-kinase axis in cancer. *Seminars in oncology.* 2004;31(1 Suppl 3):9-20.

68. Chang AJ, Desilva R, Jain S, Lears K, Rogers B, Lapi S. 89Zr-Radiolabeled Trastuzumab Imaging in Orthotopic and Metastatic Breast Tumors. *Pharmaceuticals.* 2012;5(1):79-93.

69. Dijkers EC, Kosterink JG, Rademaker AP, et al. Development and characterization of clinical-grade 89Zr-trastuzumab for HER2/neu immunoPET imaging. *Journal of nuclear medicine : official publication, Society of Nuclear Medicine.* 2009;50(6):974-981.

70. Dijkers EC, Oude Munnink TH, Kosterink JG, et al. Biodistribution of 89Zr-trastuzumab and PET imaging of HER2-positive lesions in patients with metastatic breast cancer. *Clinical pharmacology and therapeutics.* 2010;87(5):586-592.

71. Gaykema SB, Brouwers AH, Lub-de Hooge MN, et al. 89Zr-bevacizumab PET imaging in primary breast cancer. *Journal of nuclear medicine : official publication, Society of Nuclear Medicine.* 2013;54(7):1014-1018.

72. Rizvi SN, Visser OJ, Vosjan MJ, et al. Biodistribution, radiation dosimetry and scouting of 90Y-ibritumomab tiuxetan therapy in patients with relapsed B-cell non-Hodgkin's lymphoma using 89Zr-ibritumomab tiuxetan and PET. *European journal of nuclear medicine and molecular imaging.* 2012;39(3):512-520.

73. Blalock TD, Spurr-Michaud SJ, Tisdale AS, et al. Functions of MUC16 in corneal epithelial cells. *Investigative ophthalmology & visual science.* 2007;48(10):4509-4518.

74. Gipson IK. The ocular surface: the challenge to enable and protect vision: the Friedenwald lecture. *Investigative ophthalmology & visual science.* 2007;48(10):4390; 4391-4398.

75. Comamala M, Pinard M, Theriault C, et al. Downregulation of cell surface CA125/MUC16 induces epithelial-to-mesenchymal transition and restores EGFR signalling in NIH:OVCAR3 ovarian carcinoma cells. *British journal of cancer.* 2011;104(6):989-999.

76. Hattrup CL, Gendler SJ. Structure and function of the cell surface (tethered) mucins. *Annual review of physiology.* 2008;70:431-457.

77. Rump A, Morikawa Y, Tanaka M, et al. Binding of ovarian cancer antigen CA125/MUC16 to mesothelin mediates cell adhesion. *The Journal of biological chemistry.* 2004;279(10):9190-9198.

78. Dharma Rao T, Park KJ, Smith-Jones P, et al. Novel monoclonal antibodies against the proximal (carboxy-terminal) portions of MUC16. *Applied immunohistochemistry & molecular morphology : AIMM / official publication of the Society for Applied Immunohistochemistry.* 2010;18(5):462-472.

79. Lindmo T, Boven E, Cuttitta F, Fedorko J, Bunn PA, Jr. Determination of the immunoreactive fraction of radiolabeled monoclonal antibodies by linear extrapolation to binding at infinite antigen excess. *Journal of immunological methods.* 1984;72(1):77-89.

80. Sharma SK, Sevak KK, Monette S, et al. Preclinical 89Zr Immuno-PET of High-Grade Serous Ovarian Cancer and Lymph Node Metastasis. *Journal of nuclear medicine : official publication, Society of Nuclear Medicine.* 2016;57(5):771-776.

81. Thies A, Schachner M, Moll I, et al. Overexpression of the cell adhesion molecule L1 is associated with metastasis in cutaneous malignant melanoma. *Eur J Cancer.* 2002;38(13):1708-1716.

82. Schafer MK, Altevogt P. L1CAM malfunction in the nervous system and human carcinomas. *Cell Mol Life Sci.* 2010;67(14):2425-2437.

83. Kaifi JT, Reichelt U, Quaas A, et al. L1 is associated with micrometastatic spread and poor outcome in colorectal cancer. *Mod Pathol.* 2007;20(11):1183-1190.

84. Allory Y, Matsuoka Y, Bazille C, Christensen EI, Ronco P, Debiec H. The L1 cell adhesion molecule is induced in renal cancer cells and correlates with metastasis in clear cell carcinomas. *Clin Cancer Res.* 2005;11(3):1190-1197.

85. Fogel M, Gutwein P, Mechtersheimer S, et al. L1 expression as a predictor of progression and survival in patients with uterine and ovarian carcinomas. *Lancet.* 2003;362(9387):869-875.

86. Aktas B, Kasimir-Bauer S, Wimberger P, Kimmig R, Heubner M. Utility of mesothelin, L1CAM and Afamin as biomarkers in primary ovarian cancer. *Anticancer Res.* 2013;33(1):329-336.

87. Nimmerjahn F, Ravetch JV. Fcgamma receptors as regulators of immune responses. *Nat Rev Immunol.* 2008;8(1):34-47.

88. Bruhns P, Iannascoli B, England P, et al. Specificity and affinity of human Fcgamma receptors and their polymorphic variants for human IgG subclasses. *Blood.* 2009;113(16):3716-3725.

89. Sazinsky SL, Ott RG, Silver NW, Tidor B, Ravetch JV, Wittrup KD. Aglycosylated immunoglobulin G1 variants productively engage activating Fc receptors. *Proceedings of the National Academy of Sciences of the United States of America.* 2008;105(51):20167-20172.

90. Maverakis E, Kim K, Shimoda M, et al. Glycans in the immune system and The Altered Glycan Theory of Autoimmunity: a critical review. *J Autoimmun.* 2015;57:1-13.

91. Arnold JN, Wormald MR, Sim RB, Rudd PM, Dwek RA. The impact of glycosylation on the biological function and structure of human immunoglobulins. *Annu Rev Immunol.* 2007;25:21-50.

92. van der Neut Kolfschoten M, Schuurman J, Losen M, et al. Anti-inflammatory activity of human IgG4 antibodies by dynamic Fab arm exchange. *Science.* 2007;317(5844):1554-1557.

93. Rispens T, Davies AM, Ooijevaar-de Heer P, et al. Dynamics of inter-heavy chain interactions in human immunoglobulin G (IgG) subclasses studied by kinetic Fab arm exchange. *The Journal of biological chemistry.* 2014;289(9):6098-6109.

94. Rispens T, Ooijevaar-de Heer P, Bende O, Aalberse RC. Mechanism of immunoglobulin G4 Fab-arm exchange. *J Am Chem Soc.* 2011;133(26):10302-10311.

95. Silva JP, Vetterlein O, Jose J, Peters S, Kirby H. The S228P mutation prevents in vivo and in vitro IgG4 Fab-arm exchange as demonstrated using a combination of novel quantitative immunoassays and physiological matrix preparation. *The Journal of biological chemistry.* 2015;290(9):5462-5469.

96. Dekkers G, Bentlage AEH, Stegmann TC, et al. Affinity of human IgG subclasses to mouse Fc gamma receptors. *mAbs.* 2017:0.

97. Overdijk MB, Verploegen S, Ortiz Buijsse A, et al. Crosstalk between human IgG isotypes and murine effector cells. *Journal of immunology.* 2012;189(7):3430-3438.

98. Xu H, Guo H, Cheung IY, Cheung NK. Antitumor Efficacy of Anti-GD2 IgG1 Is Enhanced by Fc Glyco-Engineering. *Cancer Immunol Res.* 2016;4(7):631-638.

99. Tian X, Vestergaard B, Thorolfsson M, Yang Z, Rasmussen HB, Langkilde AE. In-depth analysis of subclass-specific conformational preferences of IgG antibodies. *IUCrJ.* 2015;2(Pt 1):9-18.

100. Heneweer C, Holland JP, Divilov V, Carlin S, Lewis JS. Magnitude of enhanced permeability and retention effect in tumors with different phenotypes: 89Zr-albumin as a model system. *Journal of nuclear medicine : official publication, Society of Nuclear Medicine.* 2011;52(4):625-633.

101. D'Huyvetter M, Vincke C, Xavier C, et al. Targeted radionuclide therapy with A 177Lu-labeled anti-HER2 nanobody. *Theranostics.* 2014;4(7):708-720.

102. Buchsbaum DJ, Khazaeli MB, Axworthy DB, et al. Intraperitoneal pretarget radioimmunotherapy with CC49 fusion protein. *Clinical cancer research : an official journal of the American Association for Cancer Research.* 2005;11(22):8180-8185.

103. Pouget JP, Navarro-Teulon I, Bardies M, et al. Clinical radioimmunotherapy--the role of radiobiology. *Nature reviews Clinical oncology.* 2011;8(12):720-734.

104. Jaspers JE, Brentjens RJ. Development of CAR T cells designed to improve antitumor efficacy and safety. *Pharmacol Ther.* 2017.

105. Sadelain M, Brentjens R, Riviere I. The basic principles of chimeric antigen receptor design. *Cancer Discov.* 2013;3(4):388-398.

106. Brentjens RJ, Davila ML, Riviere I, et al. CD19-targeted T cells rapidly induce molecular remissions in adults with chemotherapy-refractory acute lymphoblastic leukemia. *Sci Transl Med.* 2013;5(177):177ra138.

107. Brentjens RJ, Riviere I, Park JH, et al. Safety and persistence of adoptively transferred autologous CD19-targeted T cells in patients with relapsed or chemotherapy refractory B-cell leukemias. *Blood.* 2011;118(18):4817-4828.

108. Kochenderfer JN, Dudley ME, Feldman SA, et al. B-cell depletion and remissions of malignancy along with cytokine-associated toxicity in a clinical trial of anti-CD19 chimeric-antigen-receptor-transduced T cells. *Blood.* 2012;119(12):2709-2720.

109. Jackson HJ, Rafiq S, Brentjens RJ. Driving CAR T-cells forward. *Nature reviews Clinical oncology.* 2016;13(6):370-383.

110. Koneru M, Purdon TJ, Spriggs D, Koneru S, Brentjens RJ. IL-12 secreting tumor-targeted chimeric antigen receptor T cells eradicate ovarian tumors in vivo. *Oncoimmunology.* 2015;4(3):e994446.

111. Palucka K, Banchereau J. Cancer immunotherapy via dendritic cells. *Nat Rev Cancer.* 2012;12(4):265-277.

112. Korbling M, Freireich EJ. Twenty-five years of peripheral blood stem cell transplantation. *Blood.* 2011;117(24):6411-6416.

113. Grupp SA, Kalos M, Barrett D, et al. Chimeric antigen receptor-modified T cells for acute lymphoid leukemia. *N Engl J Med.* 2013;368(16):1509-1518.

114. Choy G, Choyke P, Libutti SK. Current advances in molecular imaging: noninvasive in vivo bioluminescent and fluorescent optical imaging in cancer research. *Molecular imaging.* 2003;2(4):303-312.

115. Limberis MP, Bell CL, Wilson JM. Identification of the murine firefly luciferase-specific CD8 T-cell epitopes. *Gene Ther.* 2009;16(3):441-447.

116. Briley-Saebo KC, Leboeuf M, Dickson S, et al. Longitudinal tracking of human dendritic cells in murine models using magnetic resonance imaging. *Magn Reson Med.* 2010;64(5):1510-1519.

117. Thakur ML, Lavender JP, Arnot RN, Silvester DJ, Segal AW. Indium-111-labeled autologous leukocytes in man. *Journal of nuclear medicine : official publication, Society of Nuclear Medicine.* 1977;18(10):1014-1021.

118. Sato N, Wu H, Asiedu KO, Szajek LP, Griffiths GL, Choyke PL. (89)Zr-Oxine Complex PET Cell Imaging in Monitoring Cell-based Therapies. *Radiology.* 2015;275(2):490-500.